UNIWERSYTET
MIKOŁAJA KOPERNIKA
W TORUNIU
Wydział Chemii

Universitat de Girona

DOCTORAL DISSERTATION

Intermolecular Interactions Between Fluorophores Carrying BF/BF_2 Group and Halogenated Fluorobenzenes

Alejandro Iglesias Reguant

2024

DOCTORAL PROGRAMME IN CHEMISTRY

Supervised by:

Prof. Dr. Borys Ośmiałowski

Dr. Josep Maria Luis Luis

Presented to obtain the doctoral degree at the
Nicolaus Copernicus University

Acknowledgements

"Gather ye rose-buds while ye may,
Old Time is still a-flying;
And this same flower that smiles today
Tomorrow will be dying."

-Robert Herrick-

A tots i totes les que heu decidit invertir el vostre temps en mi

I would like to express my deepest gratitude to my supervisors and advisor, whose guidance and support have been instrumental in the completion of this thesis.

First, I am immensely grateful to Borys for providing the financial support necessary to pursue this research. Besides that, you always granted me the freedom to explore my own interests, which allowed me to grow both academically and personally.

I would also like to extend my gratitude to Josep Maria, whose consistent attention has ensured that I stood on track during this journey. Thank you for your weekly meetings which helped me a lot to keep working and motivated me to try my best.

Lastly, I owe a debt of gratitude to Robert, (more than one in fact), who has selflessly shared his knowledge and expertise with me. You always looked after me and this has inspired me a lot, not only in science but in human values.

Thank you all for your exceptional guidance, support, and encouragement throughout this process.

I would also like to thank Denis, who allowed me to stay in his group in Nantes for a short period. I learned a lot from this group, both in chemistry and administration of a scientific group.

També voldria expressar la meva sincera gratitud a les persones que més estimo en la meva vida.

A la meva mare, el teu amor i creença en mi des del primer dia han estat la base sobre la qual he construït el meu present. Sovint recordo les trucades post-bici (i algun cop que havia sortit malament, durant la bici) cada diumenge del meu primer any. Gràcies per les teves paraules d'ànim i la teva fe en les meves capacitats i per estar sempre al meu costat.

A mi padre, gracias por estar siempre, por cuidarnos a Roman y a mí. Aunque no lo sepas, pienso mucho en los esfuerzos que haces cada día para que nos vaya todo bien. Me alegra

haber adquirido el hábito de la lectura gracias a vosotros, y poder hablar de los libros que leemos y hacernos recomendaciones. Eres un ejemplo a seguir como padre, y como persona.

Al meu germà, qui sempre ha estat present, a punt per una conversa de qualsevol tema. Gràcies per les rialles, les aventures i els moments de desconnexió durant aquest temps, i per aguantar-me quan intento molestar-te. Estic molt content de tenir un germà com tu.

A la Silvia, tot i que en començar la tesi encara no ens coneixiem, ara ets de les persones més importants de la meva vida. Admiro la teva feina, la qual em motiva per seguir endavant. M'encanta la teva personalitat, la qual em motiva encara més per seguir endavant. En molt poc temps hem compartit moments que ni imaginaria si no hagués estat per tu. De Toruń a Tossa, passant per Boston, Chamonix, Annecy i Bad Cannstatt, tot el que fem junts ho guardo amb molt bon record.

A Rubèn, recuerdo las llamadas diarias cuando cogía el bus de la uni a casa durante el primer año. La nieve me llegaba hasta las rodillas y hacía un frío que pelaba, pero me daba igual congelarme la mano mientras hablabamos de cualquier cosa. Cuántas horas habremos pasado en llamada durante estos años... No lo quiero ni pensar. Muchas gracias por todo, y por seguir cada día a mi lado.

A la Naina, fa més de la meitat de la nostra vida que ens coneixem, i me n'alegro molt que seguim sent amics. Sempre estar bé tornar a casa i coincidir amb la teva gent que no veus durant la resta de l'any. Gràcies per seguir aguantant-me i compartir el teu temps amb mi.

To Patryk, since day one you have assisted me with knowledge and friendship. Without your help, I would have struggled a lot in Poland. I will never forget that you invited me to Christmas and Easter with your family, because '*you can't spend these dates alone*'. Thank you very much.

A les meves families: als Iglesias, en especial les meves cosines. Gràcies per tants moments divertits, sou les millors. Als Reguant, en especial al meu oncle qui sempre m'ha

guiat per a que tot sortís el millor possible, i a la meva Àvia, encara que ja no hi ets penso sovint en tu. Y a Luis, mi tercera familia. Te agradezco mucho todo lo que haces por nosotros, eres una persona genial.

Als amics de Catalunya: en Dani i en Roger, pels padels i sopars que s'allargaven fins altes hores de la nit. A la Lorena, Alba, i Nuni, gràcies per fer tot el possible per trobarnos en les comptades ocasions que puc viatjar a Catalunya. A Christian y Alba, amigos de toda la vida, siempre es un placer quedar con vostros y disfrutar de un tiempo de calidad.

A la gent del DnD: en Nil, el millor DM, en Kiku, i l'Aniol, per totes les tardes que hem passat fent veure que erem algú altre i divertint-nos molt. A David y Joan Pere, por tantos años sufriendo a mi merced, aunque espero que también divirtiendoos. A tots, m'heu ajudat molt a distreure'm durant moltes hores durant aquests quatre anys.

To the people from Poland: to Olek, you also invited me with your family for Christmas. It was nice to meet your family and spend these dates with you. To Anna, who cares a lot for all the students, like me. I appreciate everything you do: advice, seminars, meetings... To me, all your efforts are worth it. To Judyta, you always bring a lot of energy, which helps to spark those days when one feels tired. Thanks to all of you for making my stay far from my family and friends more enjoyable.

Por último, pero no por eso menos importante, a la gente de Euskadi: a Irune, a Mikel, a Ilargi y a Amaiur. Mi segundo año está marcado por vuetro paso por Toruń. Aún me acuerdo cuando os conocí, nos juntamos enseguida. Hemos pasado muchas juergas y mucho tiempo juntos en un peridodo de tiempo muy breve. Me alegro de la decisión de ir a vivir a la residencia solo por el hecho de haberos conocido.

Abstract

In this thesis, the impact of halogen bonding on electronic and vibrational spectroscopic properties of organic fluoroborate compounds is explored using theoretical and computational methods. This thesis offers a comprehensive understanding of the mechanisms underlying these intermolecular interactions and their effects on the electronic and vibrational spectra. For each studied spectroscopic property, different research projects focused on the interactions between organic fluoroborate dyes and perfluorohaloarenes were carried out. These projects were designed based on their broad chemical interest and the valuable insights that computational chemistry can offer to the existing body of knowledge on the subject. In the first block of the thesis, I studied the photophysical properties associated with the electronic spectra of complexes formed through halogen bonding. In the second block of the thesis, the focus was on the distinctive signatures of halogen bonding in the infrared spectrum of molecular complexes.

The design of new organic dyes and the development of strategies to obtain the desired properties is still a challenging work in synthetic chemistry. Nowadays several families of dyes are studied to provide new materials of interest for the industry. Thus, this research topic is the focus of much activity and there is still plenty of room for development. The use of intermolecular interactions in such strategies to obtain dyes with desired photophysical properties requires further investigation, especially for halogen bonding. The main role of computational chemistry in this field falls to the determination of the photophysical properties of organic fluoroborates and the simulation of the effect of halogen bonding on these

properties. In this thesis, two sets of dyes are studied (Chapter 4), both formed by dyes that have been designed to be prone to interact through halogen bonds (XB) and exhibit Intramolecular Charge Transfer (ICT), with a BF/BF_2 fragment as the electron-accepting group and a N,N-dimethylamino group as the electron-donating group. The first set of dyes contains the XB acceptor site outside the acceptor-donor CT pathway. In this way, due to the halogen bond nature, the pulling of electron density should favor the CT along the conjugated system of the dye, modifying its photophysical properties. The second set of dyes contains two different XB acceptor sites, one outside the CT pathway but near the BF_2 group, and one between the electron acceptor and donor groups. In this way, the effect of the halogen bond in distinct positions within the molecule can be compared with the dyes of the first set. Therefore, the effect of the halogen bond in the electronic structure of the dyes is investigated to rationalize the underlying process occurring within this intermolecular interaction. The electronic structure calculations agreed with experimental data showing a nice fit in the absorption and emission maximum wavelength changes upon complexation. The analysis of the stability of the complexes and the electron density change during the absorption and emission processes allowed us to rationalize the effect of the halogen bonding on the photophysical properties of the organic fluoroborate dyes.

The use of infrared (IR) spectroscopy for investigating intermolecular interactions, such as halogen bonding, has garnered significant attention in recent decades. While spectroscopic features have been identified to elucidate molecular complexes, understanding the physical origins of these features has remained elusive. In this thesis, a novel method has been developed to uncover the physical origins of changes in the IR spectrum of molecular complexes resulting from intermolecular interactions. This method is based on a direct connection between changes in the nuclear relaxation polarizability and changes in IR intensity due to intermolecular interactions. By linking these changes, any Energy Decomposition Analysis (EDA) can be applied, allowing for the partitioning of changes in IR intensity caused by halogen bonding into terms with different physical origins such as electrostatics, exchange, and delocalization. The application of this method to molecular complexes sharing structural similarities with the organic fluoroborate dyes studied in this thesis underscores its interpretative power, providing new insights into the effect of halogen bonding on vibrational spectroscopy and enhancing our understanding of this intermolecular interaction.

The thesis is organized into six chapters. The introduction, Chapter 1, outlines the chemical significance of the selected topics and summarizes contributions from the chemistry community to date. Chapter 2 presents the theoretical methods, tools, and computational strategies employed throughout the thesis to conduct studies effectively. Chapter 3 outlines the objectives of the thesis. Chapters 4 and 5 delve into the discussion of reported results. Finally, Chapter 6 summarizes the main conclusions drawn from the thesis.

Contents

List of abbreviations

BODIPY boron-dipyrromethene

CP counterpoise

DCBS dimer centered basis set

DF density fitting

DFT density functional theory

EDA energy decomposition analysis

ES excited state

FIR far infrared

FQY fluorescent quantum yield

GS ground state

HB hydrogen bond

HOMO highest occupied molecular orbital

IR infrared

LUMO lowest unoccupied molecular orbital

MP2 Møller–Plesset perturbation theory of the second order

OLED organic light emitting diode

RR Romberg-Rutishauser

SAPT symmetry-adapted perturbation theory

SCS spin-component-scaled

TICT twisted intramolecular charge transfer

VP-EDS variational-perturbational energy decomposition scheme

XB halogen bond

CHAPTER 1

Introduction

Intermolecular interactions, although significantly weaker than intramolecular covalent bonds, play a crucial role in shaping the properties of molecules [1]. During the last decades, halogen bonding (XB), as one of the non-covalent interactions, has gained significant attention for its unique properties, such as directionality, tunability, and hydrophobicity [2]. Although substantial advancements have been made in both experimental and theoretical investigations, a deeper understanding of the halogen bond is crucial for the scientific community for its applications in biochemistry [3], crystal engineering [4], and photoresponsive materials [5]. The development of a variety of methods allowed the characterization of halogen bonding in molecular complexes in gas phase, solution, and solids. The present thesis highlights the use of electronic and infrared (IR) spectroscopy, both of which play a crucial role in the identification and characterization of this interaction [6, 7]. To achieve this, computational chemistry has been employed. Computational chemistry has become a widely used tool in the scientific community, utilizing methods of theoretical chemistry to calculate the geometries, electronic and vibrational structures, interactions, and properties of molecules. Using computational chemistry, the electronic and vibrational structure of molecules can be simulated with high accuracy, allowing for the identification of specific spectral features, such as vibrational frequencies or electronic transitions, and elucidation of molecular mechanisms governing spectroscopic behavior.

1.1 Dyes in Organic Chemistry

Throughout history and across cultures and continents, colors have been an intrinsic part of cultural, scientific, and artistic development. From prehistoric cave paintings to modern masterpieces, the interest in novel, bright colors, and their multiple applications has remained a central aspect of human life. In Egypt, for instance, color held such significance that artisans developed complex processes to synthesize pigments, broadening their color palette. Egyptian blue, a symbol of royalty and divinity, was created by grinding a specific mineral mixture. During the Greco-Roman era, color took on a social dimension, leading to laws that restricted the use of certain colors, like the highly prized purple dye extracted from shellfish. In the Middle Ages, the main impetus for new colors was the development of art.

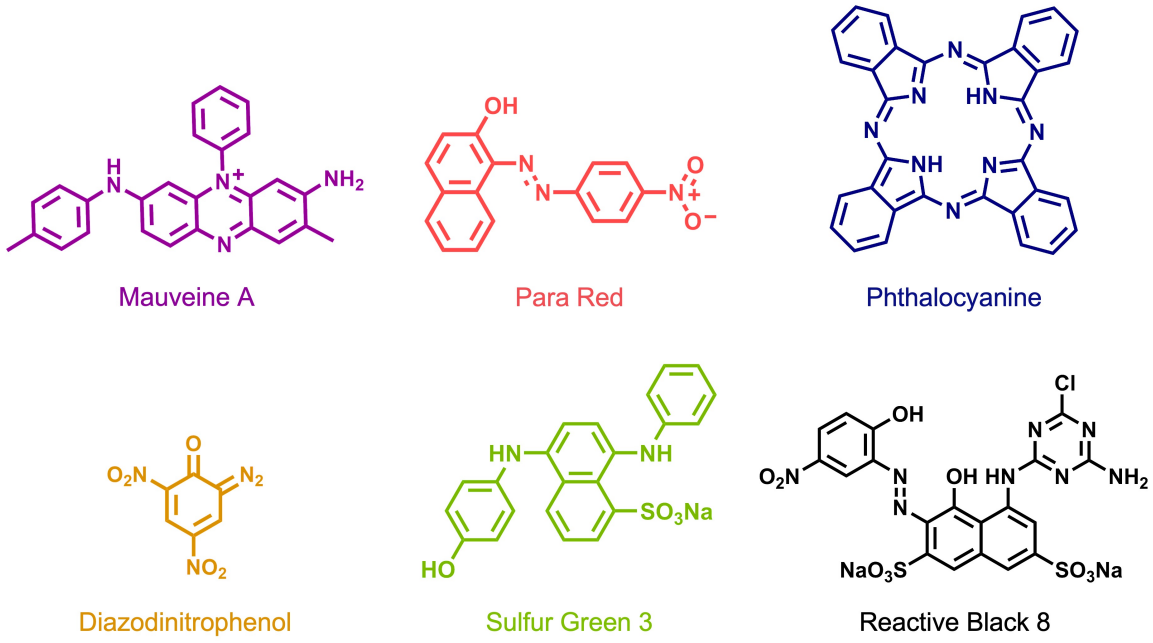

Figure 1.1: Molecular structure of the most important dye discoveries.

Once the need for colors evolved, the world of dyeing changed drastically in 1856. The turning point came with the discovery of mauveine by William Henry Perkin while trying to synthesize quinine, a drug used to cure malaria. Although mauveine only remained a commercial product for a few years, it led to the development of a huge new industry, especially in Europe [8]. Subsequent findings led to a significant transformation in this field. From the discovery of diazo compounds in 1859 by Griess [9] to the development of the first azo dyes in 1861, and the introduction of the first fully synthetic organic pigment named Para Red by Meldola in 1885, to the expansion of the field of sulfur dyes by Vidal in 1893, the color chemistry experienced significant advancements (Figure 1.1).

Two important developments were introduced in the 20th century. The first, phthalocyanines, constituted a group of colorants that transformed the methods of this field to obtain the blue and green parts of the spectrum. The second, reactive dyes, allowed cellulosic fibers to achieve remarkable levels of colorfastness (i.e. the resistance of a material to change in any of its color characteristics), which was previously achieved only through very complex and expensive processes. The development of reactive dyes created the tendency to move away from purely empirical synthesis towards studying their mechanisms and processes. Although serendipity had an important role, the knowledge obtained by synthetic organic chemistry remained an important tool. Building on earlier observations, Graebe and Liebermann discovered that colored dyes share a common feature: conjugated double bonds. Witt then developed the first comprehensive theory, proposing that colored compounds possess specific groups called chromophores, which are the specific parts of the molecule responsible for its color. This 'chromophore theory' remains the foundation for many empirical theories even today. However, it was primarily the development of quantum theory in the late 1920s that led to a new, purely quantum mechanical explanation of the chemical bond and, subsequently, the color of the chemical compounds and their spectral properties in general.

According to these theories, the term *dyes* is used to name compounds that display color due to their ability to absorb or emit light in the visible spectrum (400–700 nm) and possess at least one chromophore. Notably, just as two adjacent p-orbitals in a molecule form a π-bond, three or more adjacent p-orbitals in a molecule can form a conjugated π-system. Organic compounds carrying conjugated π-system can absorb visible light, exciting the molecule from its ground state (S_0) into an electronic excited state (S_1, S_2...). Once the molecule is excited, different processes can occur. In many cases, the subsequent emission of a photon occurs, with the return of the molecule to its ground state S_0. This phenomenon, known as fluorescence, represents one of the possible outcomes of electronic excitation. Furthermore, the presence of a conjugated system allows for the resonance of electrons, which contributes to the stability of the molecule. When any of the mentioned features are lacking from the molecular structure, the color is usually not present. In addition to these features, the presence of functional groups containing lone pairs of electrons, known as auxochromes, further influences this extended system of alternating single and double bonds. Auxochromes can participate in resonance, extending the conjugated system of the molecule. Although they are not responsible for color themselves, their presence can influence the color of a dye by shifting the position of its absorption band.

Crucial structural aspects of organic molecules influence several key properties, including the wavelength and intensity of the absorption and emission maximum. The design, synthesis, and application of functional chromophores with specific and tunable optical and electronic properties have gained significant attention in photonics and optoelectronics [10], as well as in organic light-emitting diodes (OLEDs) [11], dye-sensitized

solar cells [12], and bioimaging [13]. The most efficient and widely used strategies up to date involve the incorporation of heteroatoms, the introduction of electron-donating and/or electron-withdrawing substituents into the parent π-conjugated framework, and the extension of their π-systems by annulation with aromatic groups leading to polycyclic aromatic hydrocarbons [14, 15]. However, these established methods often face limitations due to chemical instability, poor solubility caused by the large size of the conjugated system, and difficulties in their synthesis. As a result, special efforts have been directed toward the design of new functional chromophores that overcome these limitations. To achieve this goal, researchers have systematically engineered various dye families, including polyaromatics (pyrene, tetracene, pentacene, etc.) [16], porphyrins [17], coumarins [18], xanthenes (rhodamines, fluorescein, etc.) [19], cyanines (Cy2, Cy3, and Cy5, etc.) [20], and squaraines [21], among others. One widely recognized group of dyes in recent times has been derivatives based on 4,4-difluoro-4-bora-3a,4a-diaza-*s*-indacene (BODIPY) (Figure 1.2a). These dyes have attracted the attention of the scientific community due to their tunable emission properties (i.e. their ability to emit different colors), and intensive efforts to improve their photochemical stability have provided promising results [22, 23].

1.1.1 BF/BF_2 Chromophores: Properties and Applications

Since their discovery by Treibs and Kreuzer in 1968 [24], boron-dipyrromethene (BODIPY) dyes have experienced a remarkable increase in the number and range of applications. In many cases, BODIPY dyes display relatively narrow absorption and emission bands, high molar absorption coefficients, and outstanding fluorescence quantum yields (FQY). Furthermore, BODIPY dyes exhibit redox activity in the ground and excited states, making them attractive materials for electron transfer, charge separation, excimer formation, and near-infrared emission [25–27]. However, one major drawback of BODIPY dyes, despite their intense fluorescence in solution, is their weak emission in the solid state, limiting their potential for optoelectronic applications. This weak emission is mostly produced by self-absorption caused by a small Stokes shift, leading to a strong overlap between both spectra. Additionally, the flat conjugated core facilitates tight packing of the molecules, significantly quenching their luminescence. The introduction of bulky substituents onto dyes is one effective strategy for decreasing intermolecular interactions [28]. In contrast, controlled aggregation can sometimes enhance fluorescence. This approach is useful for creating fluorescent particles from molecules that don't show fluorescence on their own in solution [29]. Due to the limitations mentioned, tailoring neutral boron dyes for fine-tuning their optical and physical properties has been explored in energy conversion devices, such as in OLEDs [30], organic photovoltaics [31], cascade-energy-transport devices [32], fluorescent probes [33, 34], and near-infrared absorbing systems [35].

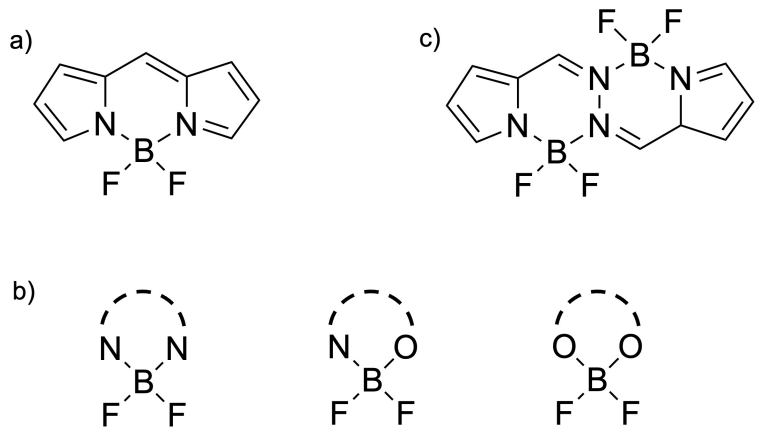

Figure 1.2: Molecular structure of (a) BODIPY, (b) the different types of BF_2 dyes, and (c) ditopic BF_2 dye.

The search for new dyes and methods to tune their properties remains a challenging target for a growing community of chemists and is far from being finished. Another promising strategy in the ongoing search for new dyes involves fluorophores containing BF/BF_2 groups, which have been demonstrated to exhibit high fluorescence efficiency, holding a privileged position within this field. These dyes feature a central boron atom bonded to four surrounding atoms, typically two neutral nitrogen and/or oxygen atoms, and two additional ligands, such as fluorine, to maintain overall neutrality. This configuration stabilizes the surrounding atoms of the boron through coordination, inducing rigidification and planarity of the π-system at the core (Figure 1.2b). This rigid structure leads to enhanced fluorescence quantum yields, conjugation, and charge transfer along the molecule's main axis, when proper substituents are used [36, 37]. Additionally, most of the N,N, N,O, or O,O complexes of boron(III) are easy to prepare and handle, and display outstanding fluorescence properties in solution and solid-state, overcoming the principal limitation of BODIPYs [38, 39].

The photophysical properties of these molecules are typically attributed to the excitation from the ground state (S_0) to the first excited state (S_1), resulting from a strong $\pi \rightarrow \pi^*$ transition within the conjugated backbone. Following this excitation, the electron may return to the ground state (S_0), emitting a photon in the process. The presence of conjugated systems strongly affects the energy levels of the molecule's electrons, which is crucial for understanding how dyes behave [40–44]. When two or more chromophores are conjugated, the absorption maximum tends to shift towards a longer wavelength (lower energy) and usually exhibits greater intensity compared to a simple unconjugated chromophore. Figure 1.3 illustrates the significance of conjugation in the UV-Vis spectrum. In conjugated dienes (C=C–C=C), the π molecular orbitals of individual alkene groups (C=C) combine to create two new bonding molecular orbitals, namely π_1 and π_2, together with two antibonding molecular orbitals, π_3^*, and π_4^*.

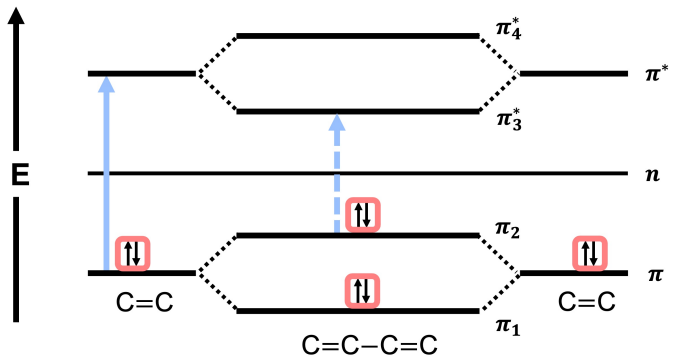

Figure 1.3: Energy level diagram with electronic transitions in conjugated systems.

Figure 1.3 shows that the promotion of an electron from the highest occupied molecular orbital (HOMO) to the lowest unoccupied molecular orbital (LUMO) of a conjugated diene ($\pi_2 \rightarrow \pi_3^*$) is lower in energy compared to the individual alkene group transition ($\pi \rightarrow \pi^*$). Similarly, for other conjugated chromophores, the energy difference between HOMO and LUMO is decreased, leading to a bathochromic shift (shift towards longer wavelengths). Thus, increasing the degree of π conjugation of organic frameworks is an effective strategy for stabilizing the LUMO and shifting both absorption and emission spectra. However, this red-shifted absorption can sometimes lead to lower quantum yields, as dictated by the energy gap law [45]. A common approach to enhance the quantum yield by increasing the rigidity of the core and extending the delocalization along the dye has led to engineering ditopic ligands capable of offering two chelation sites, as illustrated in Figure 1.2c [46]. The rigidification of the structure disfavors the vibrational and rotational nonradiative deactivation channels, leading to exceptionally high fluorescence quantum yields [47].

Interestingly, dyes can be designed with specific molecular arrangements that create an excited state in which the charge is redistributed within the molecule. This excited state can then emit light. Although their lifetimes are usually short, these dyes exhibit a significant increase in Stokes shift with solvent polarity, rendering them suitable for various applications [48–50]. Furthermore, these push-pull organic BF_2 dyes have been previously demonstrated to exhibit nonlinear optical properties, offering interesting applications in optical devices for data storage, communication, switching, computing, and image processing [51–55].

Besides, various mechanisms termed quenching can decrease the intensity of the absorption and emission of an organic dye. Dynamic quenching occurs when the quencher molecule collides with the dye in an excited state, leading to an energy transfer process between the dye and the quencher and the subsequent deactivation of the excited dye molecule. This process is dependent on the concentration of the quencher. On the other hand, static quenching involves the formation of a ground state complex between the dye and the quencher that prevents the fluorophore from absorbing light to promote an elec-

tron to the excited state and therefore prevents fluorescence from occurring [56]. Static quenching is usually observed as a decrease in the absorption of the dye, in addition to the reduction in fluorescence intensity. By understanding and characterizing all these effects, particularly in the context of halogen bonding, researchers can design tunable materials with fluorescence properties tailored for a wide range of applications.

A wide variety of examples of new organic borate dyes can be found in the literature. Some boron complexes exhibit a relatively strong covalency of B–O and B–N bonds compared to other atoms used in the field of electroluminescent devices, such as aluminum. This feature allows the engineering of numerous high-performance fluorescent borate emitters for use in OLED devices [57]. Beyond OLEDs, borate complexes also serve as photosensitizers in photovoltaic cells and polymerization, enabling efficient cascade energy transfer under certain functionalization conditions [32, 58]. A distinct potential application is the use of these dyes as optical chemical sensors, where the electronic structure of the dyes changes by the effect of the chemical composition of the environment, such as solvent effects, and intermolecular interactions. Numerous studies have been published on this subject, highlighting their versatility. For instance, research has led to the development of highly stable and pH-independent boranil dyes, used for the selective detection of H_2O_2. These dyes have extended applications in the imaging of H_2O_2 in living cells [59]. Similarly, there have been successful efforts in designing novel colorimetric probes tailored for the selective and sensitive detection of NO_2, both in solution and air [60]. Additionally, a series of innovative redox-active, fluorescent halogen bonding and hydrogen bonding (HB) BODIPY-based anion sensors have been introduced [61]. Despite their numerous attractive features, some aspects of their spectroscopic properties require further investigation. By understanding how to control these dyes at a fundamental level, scientists can manipulate their properties to obtain novel materials. In the present thesis, the efforts are focused on the study of the effect of halogen bonding on the spectroscopic properties of organic fluoroborate dyes.

1.2 Halogen Bonding

Non-covalent interactions play a crucial role in determining the physical properties of matter across various states. These interactions shape the structure, stability, and functionality of molecules and materials in fields like biology, chemistry, physics, nanotechnology, and pharmacy [62–64]. Nowadays, there are several known non-covalent interactions, such as hydrogen bonding, π–π stacking, and halogen bonding. This classification of intermolecular interactions can be put on solid quantitative grounds using modern theories like symmetry-adapted perturbation theory (SAPT), i.e. it is possible to analyze quantitatively the stability of molecular complexes in terms of fundamental interaction types (electrostatic, exchange, induction, dispersion).

The history of the study of halogen bonding can be traced back approximately two centuries ago when $I_2 \cdots NH_3$ was serendipitously synthesized by J. J. Colin while working in the laboratory of J. L. Gay-Lussac. However, it was not until a century later that significant discoveries on charge-transfer interactions by R. Mulliken and O. Hassel were made [65]. The new understanding of these kinds of interactions allowed for fundamental advancements in the comprehension of the nature of halogen bonding. These early studies established that the strength of halogen bonding increases with the polarizability of the halogen atom, following the trend F < Cl < Br < I [66–68]. This trend is further emphasized by fluorine, the least polarizable halogen. Fluorine only exhibits halogen bonding when attached to a particularly strong electron-withdrawing group [69, 70]. Additionally, in the 1950s, X-ray crystallography studies by O. Hassel played a key role in understanding how atoms are arranged in halogen-bonded complexes formed by molecules with two halogen atoms (dihalogens) or halogen-containing molecules (halocarbons) and electron-donating molecules. The review by H. A. Bent in 1968 on the chemistry of donor-acceptor adducts comprehensively discussed the crystal structures of halogen-bonded systems known at that time [71]. This review emphasized distinctive geometric features such as short interatomic distances and high directionality. This understanding opened the door to designing halogen-bonded complexes with tailored properties. Scientists discovered they could control the structure and function of these self-assembled adducts by carefully choosing the building blocks (molecules) involved. However, the ability of the halogens to act as an electrophilic species was surprising and counter-intuitive as they are among the most electronegative elements in the periodic table.

A significant breakthrough in understanding the electronic structure of halogen bonding emerged from computational studies in the early 1990s, focusing on the electron density distribution in halogen atoms. Studies by P. Politzer and J. S. Murray were particularly impactful as they demonstrated the anisotropic charge distribution on halogen atoms forming one covalent bond [72–74], leading to the definition of the "σ-hole", a region of depleted and often positive electrostatic potential on the surface of halogen atoms. The σ-hole concept has been expanded and now refers to the electron-deficient outer lobe of a half-filled p (or nearly p) orbital of an atom forming a covalent bond [75].

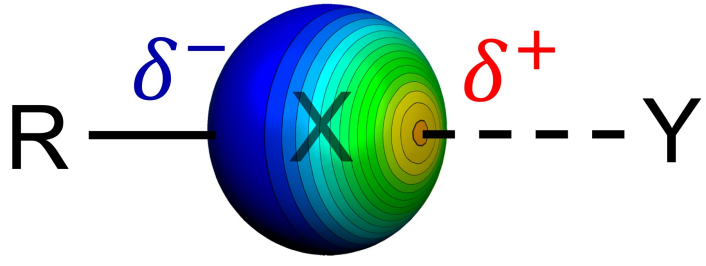

Figure 1.4: Schematic representation of the halogen bond.

If the electron deficiency of the outer lobe is significant, there can be a positive electrostatic potential region, interacting non-covalently with the negative sites on other molecules. The process of characterizing the halogen bond increased the interest of the scientific community in the topic. The strength and tunability of the interaction, resulting from the possible use of four different halogen atoms acting as electron density acceptor sites, resulted in a rapid increase in the number of investigations on XB. Finally, the IUPAC project's inaugural event further refined this consensus. After a 200-year process, the IUPAC definition of the XB finally registered the agreement reached by the scientific community [76]:

> '*A halogen bond occurs when there is evidence of a net attractive interaction between an electrophilic region associated with a halogen atom in a molecular entity and a nucleophilic region in another, or the same, molecular entity.*'
>
> – IUPAC definition of halogen bond

According to this definition, a typical halogen bond is represented as R–X$\cdots$Y, where dots indicate the noncovalent interaction. The XB donor is denoted by R–X. Here, R is an electron-withdrawing group, and X is a halogen atom covalently bonded to R. This halogen atom has an electrophilic region on its surface, as shown in Figure 1.4. The XB acceptor is Y, which donates electron density to R–X. It can be an anion or a neutral molecule containing a nucleophilic region, such as a lone pair or a π-system. Interestingly, the term *halogen bond* offers the advantage of explicitly highlighting the most characteristic and general aspect of the interaction, namely, that it involves halogen atoms. Extensive reviews on the nature of the halogen bond and its applications can be found in the literature [2, 77]. Additionally, this term recalls immediately the term *hydrogen bond*, and by analogy, halogens are presumed to work as electrophiles similar to the hydrogen atoms in hydrogen bonding. However, while both interactions involve a positive site played by the respective atom (halogen or hydrogen), they differ in several aspects.

Notably, halogen bonds exhibit higher directionality compared to hydrogen bonds. Typically, the R–X$\cdots$Y angle for reasonably strong halogen bond adducts is close to 180°. This feature arises from various factors, such as its charge-transfer character in which lone pair electrons of Y are donated into the σ^* orbital of the halogen bond donor, and the electrostatic attraction between Y and the halogen bond donor due to the anisotropic distribution of its electron density. Additionally, repulsive interaction between the p-orbitals of the halogen atom lone pairs and the halogen bond acceptor contributes to the directionality of the noncovalent interaction. Consequently, strong halogen bonds with shorter bond lengths tend to be more directional than weaker ones with longer lengths. Additionally, reducing the polarizability of the halogen bond donor can decrease its linearity. This feature

has been established both experimentally [78] and computationally [79, 80], forming the basis of their high reliability in crystal engineering.

The XB donor ability, which determines the interaction strength, decreases in the order I > Br > Cl > F. This trend is explained by the positive character of the σ hole, which increases with the polarizability and decreases with the electronegativity of the halogen atom [81]. The energy of the XB can also be tuned by structural modifications affecting the electron-withdrawing ability of the moieties covalently bound to a given halogen atom. When electron-withdrawing moieties diminish the electron density in the region called the σ-hole on the XB donor atom, the strengthening of the XB can be achieved. Additionally, the closer the electron-withdrawing moiety is to the halogen atom, the greater the effect. For that reason, haloarenes have been commonly used in crystal engineering based on XB. Nowadays, the partial or full substitution of hydrogen atoms with fluorine atoms on the aromatic ring is a well-established strategy to increase the size and positive potential of the σ-hole at the halogen atom [82].

Halogen atoms, particularly I and Br, are often considered hydrophobic, unlike typical hydrogen bond donors such as OH and NH groups. This difference between the two donor site types results in many useful applications. For instance, drug absorption and delivery to target tissues typically require the compound to cross cell membranes. By incorporating halogen atoms into lead compounds, scientists can increase their lipophilicity (affinity for fats) and therefore their ability to pass through these cell membranes [83]. A well-known example is the drug chloramphenicol, which contains chlorine atoms and exhibits improved lipophilicity compared to its non-halogenated counterpart [84].

Furthermore, the halogen atoms possess larger van der Waals (vdW) radii than the hydrogen atom, leading to differences in some properties of interactions involving these atoms. For instance, vdW radius for iodine is approximately 1.65 times larger than hydrogen. Consequently, XB is more sensitive to steric hindrance than HB. Noteworthy, in certain cases, bromine might be preferred over iodine due to the latter's higher vdW radii overcoming the advantage of its higher polarizability. However, it is important to note that excessive halogenation can sometimes lead to unintended consequences, such as increased toxicity or decreased water solubility. Careful design is crucial for achieving the desired balance of properties.

The unique properties of halogen bonding have spurred extensive research, establishing it as a valuable tool in diverse fields such as self-assembly [66], biochemistry [85], crystal engineering [86], and photoresponsive materials science [87]. Halogen bonding's ability to precisely control molecular alignment, particularly in liquid-crystalline materials, has opened doors for light-powered applications such as photomechanical oscillators [88], plastic micromotors [89], and robotic arm movements [90]. This success largely relies on the directional nature of halogen bonding. Moreover, its tunability offers unprecedented potential for fundamental research on light-induced motions, compared to other material

systems. Despite the successful application of XB in self-assembly designs, certain fundamental aspects of this interaction remain under debate. The σ-hole concept elegantly rationalized the behavior of halogen atoms as electrophiles and it is commonly used. However, documented examples of halogen-bonded complexes exist whose characteristics cannot be solely explained by the σ-hole [91, 92]. Thus, the study of such interactions is needed for the further understanding of its nature and unveiling its effects on the spectroscopic properties of organic dyes.

Understanding the energetic and structural characteristics of molecular interactions is crucial for researchers in various fields. Techniques such as electronic and infrared spectroscopy offer a powerful means of probing the structural features of molecular systems. For instance, electronic spectroscopy is a versatile tool for both qualitative and quantitative analysis. Specifically, fluorescence analysis is widely used across various sample states, including powders, crystals, films, and liquids. It offers numerous advantages, such as high sensitivity, strong selectivity, minimal sample volume requirement, and the provision of multiple physical parameters.

As mentioned in the previous section, organic luminescent materials have received considerable attention due to their potential applications in fields like organic electronics, photonics, and sensing [93]. The packing of these materials in the solid state greatly influences their emissive properties, making it essential to tune these properties via external stimuli such as intermolecular interactions [94]. Duan et al. demonstrated a notable example of utilizing halogen bonding to tune the fluorescence of solid-state materials [95]. They cocrystallized a stilbene derivative with nonfluorescent halogen and hydrogen bond donors. This approach resulted in distinct crystal packing compared to the pure compound, which in turn strongly affected its optical properties, enabling the tuning of emission color from blue to green and yellow. Building on this concept, Taddei et al. further underscored the importance of halogen bonding in modulating luminescence properties, particularly emission intensity or wavelength. For instance, they studied the luminescence properties of several 1,8-naphthalimide derivatives in solution and the crystal/co-crystal state, revealing that solid crystals displayed red-shifted fluorescence with increased emission quantum yield compared to solution [96]. Additionally, the luminescence properties of co-crystals of diiodotetrafluorobenzene and diphenylacetylene were studied by the same group, concluding that depending on the stoichiometry, these cocrystals exhibit both fluorescence and phosphorescence or exclusive phosphorescence at room temperature [97]. The dyes of these studies hold promise for light-emitting solid-state materials due to their unique properties facilitated by halogen bonding. Beyond this, halogen bonding serves as a valuable analytical tool, as demonstrated by recent studies. The Würthner group explored its role in squaraine dye self-assembly [98]. Beer et al. utilized it in porphyrin-based anion sensors with haloimidazolium [99]. Ge et al. investigated the role of XB between iodine and ciprofloxacin in photoinduced electron transfer [100]. These highlighted studies provide

valuable insights into the use of halogen bonding for designing and manipulating functional supramolecular materials for photonic applications.

Moreover, as explained above, recent investigations have revealed that the impact of halogen bonding extends beyond structural parameters, influencing the fluorescence modulation of certain dyes. For instance, a recent study by Priimagi et al. focused on the halogen bonding interaction between a carbazole-based, pyridine-substituted organic semiconductor and a common halogen-bond donor, pentafluoroiodobenzene [101]. This interaction facilitated efficient halogen-bond-driven fluorescence modulation in solution. To elucidate the effect of halogen bonding on dye fluorescence, researchers often combine techniques such as steady-state and time-resolved emission and absorption spectroscopy with density functional theory (DFT) calculations. Priimagi et al. [101], employed this approach to demonstrate that halogen-bond-induced intramolecular charge transfer played a pivotal role in fluorescence modulation. Such fluorescence modulation offers a range of possibilities, both in solution and solid state, including the potential design of tunable luminescent materials for light-emitting devices [102].

Capitalizing on its ability to modulate fluorescence, halogen bonding has proven to be an excellent tool for tailoring supramolecular assemblies of diverse functional materials. However, although some recent studies have reported investigations in the absorption and emission of halogen-bonded BODIPY complexes [103, 104], the mechanism behind the effect of halogen bonding in the absorption and emission signatures of BF/BF_2 dyes remains for further elucidation. A key gap in our understanding lies in solution-phase studies. Most research has focused on the solid state, investigating the impact of halogen bonding on crystal packing and the geometry of molecules in the complexes. Consequently, exploring solution-phase interactions will provide a more comprehensive picture of halogen bonding effects on BF/BF_2 dyes.

While electronic spectroscopy provides insights into the electronic transitions and the excited-state properties of XB complexes, vibrational spectroscopy offers valuable information about their structural aspects. Transitioning from electronic to vibrational spectroscopy, allows us to probe the molecular vibrations involved in XB interactions, offering detailed insights into the geometry and bonding features of XB complexes. A wide variety of vibrational spectroscopy studies, particularly those using IR spectroscopy, have been crucial for determining general features of halogen bonding in solid complexes, with some application to liquid complexes as well. Observing vibrational shifts upon complex formation, particularly for C–X modes, is a powerful tool to establish the presence of an XB. Infrared spectroscopy, including far infrared (FIR), since these C–X modes are found between 100 and 800 cm^{-1}, is among the techniques most commonly employed to study the XB interaction [105, 106]. A common assumption for R–X$\cdots$Y–R' complexes, first expressed by N. F. Cheetham and A. D. E. Pullin [107], acknowledges the weak nature of the X$\cdots$Y bond. Therefore, the X$\cdots$Y stretching modes may present frequencies lower

than 150 cm^{-1}. This assumption suggests that the vibrational spectra of XB complexes can be primarily understood by considering how X$\cdots$Y interaction modifies the original vibrational frequencies of the R–X and Y–R' bonds. This is supported by the observation that similar XB complexes often exhibit analogous changes in their vibrational spectra.

Early works in vibrational spectroscopy revealed several fundamental features of halogen bonding. For instance, researchers observed a small redshift (decrease in wavenumber) of the R–I stretching in the far IR region of iodine cyanide complexes, accompanied by a significant intensity increase in the bands of the infrared spectra [108]. These findings were explained with Mulliken's charge-transfer model [109]. This model proposes that a weak interaction can be formed when lone pair electrons (n) from a Lewis base (Y) donate electron density to a partially positive lobe of an empty anti-bonding σ^* orbital of the halogen in the Lewis acid (R–I). According to this model, as the R–I$\cdots$Y weak bond gains strength due to n $\rightarrow \sigma^*$ transfer, the resonance formula $(R–I)^- \cdots Y^+$ becomes more prominent. Consequently, the R–I force constant (a measure of bond strength) decreases, and the effective charge on the R atom increases. These changes lead, respectively, to a red-shifted and higher-intensity R–I stretching mode observed in the infrared spectrum.

Additionally, Person et al. noted the appearance of new bands in the infrared spectra of pyridine bases upon complexation [110]. Furthermore, a series of infrared spectra of the complex between dimethylacetamide and iodine revealed the appearance of a second C=O stretching band with a 43 cm^{-1} redshift, while the C–N stretching showed a 70 cm^{-1} blue shift [111]. These results suggested iodine coordination with the oxygen atom rather than the nitrogen atom, a binding model confirmed by several X-ray structures. Moreover, the intensities of the complexed and free carbonyl bands showed reciprocal changes with the iodine/dimethylacetamide ratio, indicating the presence of only two main species: free amide and the halogen-bonded complex.

Cheetham and Pullin conducted a detailed study on the vibrational spectra of CF_3–X (X = I, Br) in mixtures with various Lewis bases [112, 113]. They examined mixtures in vapor form, CCl_4 solutions (at room temperature), liquids (at lower temperatures), and solid films (at 80 K). Their observations, particularly for triethylamine complexes, revealed several significant features. These included the emergence of a low-frequency band around 100 cm^{-1}, attributed to non-covalent interaction X$\cdots$N stretching, and a red-shifted C–X stretching band with notably increased intensity at approximately 260 cm^{-1} (X = I) and 330 cm^{-1} (X = Br). Building upon this work, Metrangolo, Resnati, and their colleagues embarked on a systematic investigation in the late 1990s, focusing on halogen-bonded complexes involving iodoperfluoroalkanes and iodoperfluoroarenes using FTIR spectroscopy [114–116]. Their findings supported those of Cheetham and Pullin, particularly concerning shifts in C–F, C–X, and C–H stretching frequencies. They validated these observations not only for longer haloperfluoroalkanes but also for aromatic systems acting as either XB donors or acceptors.

In a recent study, researchers employed matrix-isolation infrared spectroscopy and electronic structure calculations to explore CH_3OH and CCl_4 complexes, investigating the competition between hydrogen bonding ($OH\cdots Cl$) and halogen bonding ($CCl\cdots O$) [117]. By analyzing the C–Cl, C–O, and O–H stretching regions using vibrational spectroscopy, they identified one halogen-bonded minimum and two hydrogen-bonded minima in the dimer potential energy surface, highlighting the capability to characterize halogen bonding using infrared spectroscopy.

In a study by Prof. Herrebout et al., the IR and Raman spectra of solutions containing mixtures of trimethylamine and CHF_2I, as well as of dimethoxyethane and CHF_2I, were analyzed [118]. The results revealed that both hydrogen and halogen-bonded complexes appeared simultaneously in these mixtures. However, when CHF_2I was mixed with methyl fluoride, only a hydrogen-bonded complex was formed. These findings suggest that solvent can be used to favor either halogen bonding or hydrogen bonding, allowing for the rational design of new complexes. Another study presented IR and Raman spectroscopic data demonstrating the formation of $C–X\cdots\pi$ bonded complexes between trifluorohalomethanes CF_3X (with X = Br, I) and aromatic model compounds such as benzene and toluene [119]. Infrared and Raman experiments, supported by ab initio calculations, revealed the formation of a 2:1 complex, in which two CF_3I molecules were bonded to a single molecule of benzene.

Despite numerous studies using infrared spectroscopy to identify halogen bonding, the physical mechanisms behind the observed spectral changes remain elusive. The present thesis focuses on the description and characterization of halogen bonding and its effect on the spectroscopic properties of organic dyes. To achieve this, first, the BF/BF_2 family of organic dyes, known for their intense colors and photostability, will be briefly introduced, followed by a discussion of halogen bonding and its characterization methods. Then, the results obtained during this research will be presented, focusing primarily on the effect of halogen bonding in the fluorescence and infrared spectra of organic dyes. Additionally, a newly developed computational methodology will be described and applied to decompose the IR spectra of molecular complexes and their changes upon complex formation into terms of different physical origins, such as electrostatics, exchange-repulsion, delocalization, and dispersion. With this, we aim to highlight the impact of halogen bonding in electronic and infrared spectroscopy of organic systems and extend its comprehension to the scientific community. This research holds significant importance for two key reasons. First, it will advance the fundamental understanding of XB, which is crucial for various scientific fields. Second, by understanding the physical mechanisms of spectral changes linked to XB, we can achieve precise control over XB molecular assembly and design. This has broad implications across chemistry and materials science, facilitating the development of novel functional materials with tailored properties.

CHAPTER 2

Methodology

Computer simulations might be invaluable in unraveling intermolecular interactions. When the proper theoretical framework is used, it provides valuable insights into the fundamental principles governing molecular behavior. Compared to experimental techniques, computational methods offer a cost-effective and efficient way to explore the interaction pattern at the molecular scale. They can also complement experimental data and guide further experimentation. In this section, I will explain the theoretical framework used in the thesis, emphasizing the less common theoretical approaches. I will first introduce the concept of interaction energy (ΔE), followed by a discussion of the Energy Decomposition Analysis (EDA) employed in this work, specifically the Variational-Perturbational Energy Decomposition Scheme (VP-EDS). Next, I will briefly explain the computational procedures used to determine the interaction energies in molecular complexes. These procedures include methods like Spin-Component-Scaled at the MP2 level (SCS-MP2). I will then describe the procedure used in the thesis to calculate the formation Gibbs Energy, considering relevant experimental conditions. Finally, I will explain the methodology used to compute interaction energy derivatives with respect to an external electric field to obtain properties like excess nuclear relaxation polarizability ($\Delta\alpha^{nr}$) necessary for studying infrared spectra.

One essential property for studying intermolecular interactions is the interaction energy (ΔE) between molecules. For a system *AB* composed of two subsystems *A* and *B*, ΔE is defined as:

$$\Delta E(\mathbf{R}) = E_{AB}(\mathbf{R}) - [E_A(\mathbf{R}) + E_B(\mathbf{R})] \tag{2.1}$$

where $E_{AB}(\mathbf{R})$ represents the electronic energy of the total system, while $E_A(\mathbf{R})$ and $E_B(\mathbf{R})$ denote the electronic energies of the interacting subsystems, respectively, at the geometry they adopt in the complex (denoted by **R**). The two-body interaction energy can be calculated directly through Equation 2.1 as the difference between the energy of the dimer and the sum of energies of the isolated molecules. A negative ΔE indicates an attractive interaction (favorable for complex formation), while a positive ΔE indicates a repulsive interaction.

The supermolecular method offers flexibility in using various electronic structure methods to study interactions between molecules, particularly those involving noncovalent interactions (weaker interactions compared to covalent bonds). However, calculations using finite basis sets are susceptible to basis set superposition error (BSSE). This effect is due to a nonphysical lowering of the energy of the monomer during calculation for the complex, as the monomer "borrows" the basis set from the other subsystem. To address this challenge, the Counterpoise (CP) method was introduced by Boys and Bernardi in 1970 [120]. This method, particularly relevant in studies involving noncovalent interactions, aims to mitigate the effects of basis set superposition, enhancing the accuracy of calculated interaction energies [121].

A different approach to compute interaction energies between molecules is perturbation theory. Its symmetry-adapted variant, known as symmetry-adapted perturbation theory (SAPT), allows for gaining an insight into the physical origins of intermolecular interactions by decomposition of interaction energy into terms with clear physical interpretation (electrostatic, exchange, induction, dispersion; and the mixed terms). Presently available implementation of SAPT at the second-order level with respect to the intermolecular interaction operator allows the determination of interaction energies with low percentage errors [122]. Nowadays SAPT framework is used with Hartree-Fock as well as Kohn-Sham theories [123]. SAPT allows to decompose the total interaction energy into various components and hence it is a powerful tool for understanding and interpreting experimental data. By analyzing the contributions of individual energy terms (electrostatic, induction, dispersion, etc.), researchers can rationalize the stability of different conformers, reactivity patterns, and even spectroscopic properties. SAPT-based energy decomposition analyses (EDA) often provide valuable support for spectroscopic measurements. By linking the observed spectral signatures with specific interaction types, EDA helps bridge the gap between theoretical calculations and experimental observations [124–126]. A vast amount of data is available for numerous molecular complexes, providing deeper insights into how fundamental interaction types govern the structure, stability, and organization of these complexes on a larger scale [127–131]. In the present thesis, the Variational-Perturbational Energy Decomposition Scheme (VP-EDS) framework was employed to study the intermolecular interactions in halogen-bonded complexes. This method uses both the supermolecular approach to calculate the interaction energy between the subsystems (e.g., halogen bond

donor and acceptor) in the complex and perturbation theory framework to determine physically meaningful components (low orders of SAPT) [132, 133]. The VP-EDS is used to decompose the MP2 interaction energy into the Hartree-Fock ($\Delta E_{int}^{\mathrm{HF}}$) and electron correlation ($\Delta E_{corr}^{\mathrm{MP2}}$) contributions:

$$\Delta E_{int}^{\mathrm{MP2}} = \Delta E_{int}^{\mathrm{HF}} + \Delta E_{corr}^{\mathrm{MP2}} \tag{2.2}$$

Subsequently, $\Delta E_{\mathrm{int}}^{\mathrm{HF}}$ can be easily partitioned into first-order (Heitler-London) $E^{(1)}$ and higher-order delocalization $\Delta E_{del}^{\mathrm{HF}}$ contributions (the latter term encompasses induction contributions).

$$\Delta E_{int}^{\mathrm{HF}} = \Delta E^{(1)} + \Delta E_{del}^{\mathrm{HF}} \tag{2.3}$$

Although the partition of $E^{(1)}$ into electrostatic $\varepsilon_{el}^{(10)}$, and exchange $\Delta E_{ex}^{\mathrm{HL}}$ is nontrivial in the variational approach, it can be achieved using perturbation methods [132]. While the calculation of first-order electrostatics is not very time-consuming, the CPU cost of the exchange contributions is ten times higher. For that reason, the most efficient way to obtain $\Delta E_{ex}^{\mathrm{HL}}$ is as the residue between $E^{(1)}$ and $\varepsilon_{el}^{(10)}$:

$$\Delta E_{ex}^{\mathrm{HL}} = \Delta E^{(1)} - \varepsilon_{el}^{(10)} \tag{2.4}$$

Note that for any interaction energy component, $\varepsilon^{(ij)}$, the indices *i* and *j* denote the orders of the intermolecular and intramonomer perturbation operators, respectively. Within this framework, the HF contribution to the interaction energy can be split into the following three terms:

$$\Delta E_{int}^{\mathrm{HF}} = \varepsilon_{el}^{(10)} + \Delta E_{ex}^{\mathrm{HL}} + \Delta E_{del}^{\mathrm{HF}} \tag{2.5}$$

where $\varepsilon_{el}^{(10)}$ represents the Coulombic interaction of the charge distributions of subsystems, $\Delta E_{ex}^{\mathrm{HL}}$ arises due to the antisymmetrization of the wavefunction to fulfill Pauli principle, and $\Delta E_{del}^{\mathrm{HF}}$ describes the polarization effects, e.g. the second-order induction energy results from the mutual polarization of the subsystems by the static electric fields of unperturbed partners. Furthermore, $\Delta E_{corr}^{\mathrm{MP2}}$ can be decomposed as:

$$\Delta E_{corr}^{\mathrm{MP2}} = \varepsilon_{el,r}^{(12)} + \varepsilon_{disp}^{(20)} + \Delta E_{ex}^{(2)} \tag{2.6}$$

where $\varepsilon_{el,r}^{(12)}$ is the second-order electron correlation correction to the electrostatic interaction energy, $\varepsilon_{disp}^{(20)}$ is the dispersion energy, which may be interpreted as the stabilizing energetic contribution due to the correlations of instantaneous multipole moments of the subsystems, and $\Delta E_{ex}^{(2)}$ is the remaining second-order electron correlation effects [134, 135]. Finally, the complete decomposition under the VP-EDS framework can be presented as:

$$\Delta E_{int}^{\mathrm{MP2}} = \varepsilon_{el}^{(10)} + \Delta E_{ex}^{\mathrm{HL}} + \Delta E_{del}^{\mathrm{HF}} + \varepsilon_{el,r}^{(12)} + \varepsilon_{disp}^{(20)} + \Delta E_{ex}^{(2)} \tag{2.7}$$

The accuracy of perturbation theory methods, like MP2, can be improved by using the Spin-Component-Scaled MP2 (SCS-MP2) methods. SCS-MP2 modifies the standard MP2 approach by introducing scaling factors for the opposite-spin (OS) and same-spin (SS) components of the correlation energy [136, 137]. SCS-MP2 recognizes that the correlation experienced by electrons with the same spin differs from that of opposite-spin electrons. By applying targeted scaling factors to these components, SCS-MP2 improves the accuracy of MP2 calculations, particularly for weakly interacting complexes like the ones studied in this thesis [138]. The correlation energy can be separated into contributions of electron pairs with the same spin (SS) and opposite spin (OS):

$$E_C = E_C^{\mathrm{SS}} + E_C^{\mathrm{OS}} \tag{2.8}$$

In the HF method, the SS electron pairs are already correlated (Fermi hole), whereas the OS pairs remain uncorrelated. Low (second) order perturbation theory cannot fully correct for this unbalanced starting point. Hence, the non-HF-correlated pair contribution (OS) must be scaled up (it is underestimated in MP2), whereas the HF-correlated contribution (SS) must be scaled down according to:

$$E_C[\text{SCS-MP2}] = c_{\mathrm{OS}} E_C^{\mathrm{OS}}[\text{MP2}] + c_{\mathrm{SS}} E_C^{\mathrm{SS}}[\text{MP2}] \tag{2.9}$$

where c_{OS} and c_{SS} are empirical scaling factors with values of 6/5 and 1/3, respectively, which have been obtained from a fit to a set of representative reaction energies [139]. While SCS-MP2 is usually more accurate than MP2, it has a similar computational cost, which can be high for large molecules or molecular clusters. Such high computational cost can be reduced using the density fitting (DF) approximation, a technique to approximate four-center, two-electron repulsion integrals using three-index integrals, thus reducing the scaling of computational cost with respect to the basis set size. DF method achieves this by expanding electron densities using auxiliary basis sets and fitting coefficients. This integral approximation allows for the efficient determination of interaction energies of large chemical systems using the SCS-MP2 level of theory, which is why it was chosen for this thesis.

In addition to interaction energy, an important thermodynamic magnitude used in the field for studying the formation of molecular complexes is the formation Gibbs energy (ΔG). Using established thermodynamic definitions, the Gibbs energy of a system (G) can be expressed as:

$$G = H - TS \tag{2.10}$$

where H is the enthalpy, T is the temperature, and S is the entropy. According to the supermolecular approach, ΔG is often computationally determined as:

$$\Delta G = G_{AB} - [G_A + G_B] \tag{2.11}$$

where G_{AB} represents the free energy of the total system, while G_A and G_B denote the free energies of the interacting subsystems, calculated at their corresponding optimized nuclear positions. The formation Gibbs energy is crucial for the understanding of the chemical equilibria. The equilibrium constant of a reaction is directly related to the difference in Gibbs energy between the products and reactants at their standard conditions. Therefore, determining the free energy of all species involved in the formation of a complex enables accurate predictions of equilibrium concentrations, indicating whether a compound is energetically favorable to be formed under specific conditions.

Gibbs (free) energies are often calculated using Equation 2.11. However, the Gaussian code computes by default the Gibbs energy of a molecule in gas phase standard conditions (i.e. 1.0 atm), G^*. Therefore, using the Gibbs energies obtained from default calculations using the Gaussian code, ΔG^* can be defined as:

$$\Delta G^* = G^*_{AB} - [G^*_A + G^*_B] \tag{2.12}$$

where G^*_{AB}, G^*_A, and G^*_B represent the standard-state gas-phase Gibbs energy at 1 atm of the *AB*, *A*, and *B* chemical systems, respectively, calculated at their corresponding optimized geometries. However, experimental conditions differ from standard-state gas-phase conditions. Consequently, the Gibbs energy change associated with the conversion from a standard-state gas-phase pressure of 1 atm to a given standard-state solvent phase concentration of *X* M (where *X* is the molarity concentration of reagents and products in agreement with experimental data) must be considered when computing ΔG. The conversion between different thermodynamic conditions can be expressed as:

$$\Delta G = \Delta G^* + RT\ln\left(\frac{Q}{Q^*}\right) \tag{2.13}$$

Q is the reaction quotient of the contractions of the product and reactants, *R* is the universal gas constant (1.987 cal/Kmol), and *T* is the temperature in Kelvin. Consider the following reaction as an example:

$$A + B \rightarrow C \tag{2.14}$$

Then, the reaction quotient *Q* becomes [*C*]/([*A*][*B*]). If *A*, *B*, and *C* are ideal gases, their concentration at 1 atm may be derived from the ideal gas law as $\frac{1}{24.5}$mol L^{-1} at 298 K. Assuming a standard-state solvent phase concentration of 1M (ΔG°), Equation 2.13 becomes:

$$\Delta G^{\circ} = \Delta G^{*} + RT\ln\left(\frac{\frac{[C]^{\circ}}{[A]^{\circ}[B]^{\circ}}}{\frac{[C]^{*}}{[A]^{*}[B]^{*}}}\right) = \Delta G^{*} + RT\ln\left(\frac{\frac{1}{1\cdot 1}}{\frac{\left(\frac{1}{24.5}\right)}{\left(\frac{1}{24.5}\right)\left(\frac{1}{24.5}\right)}}\right) = \Delta G^{*} - RT\ln(24.5) \tag{2.15}$$

To better describe the experimental conditions, one should work with the experimental concentration in solvent-phase for each compound. An equivalent compound-by-compound equation to equation (2.13) can be expressed as:

$$\Delta G = \Delta G^{*}_{X} + RT\ln\left(\frac{[X]_{exp}}{\frac{1}{24.5}}\right) \tag{2.16}$$

where subscript *X* refers to the chemical compound.

Once the procedure for calculating ΔG has been defined, it is necessary to present the algorithm for evaluating energy derivatives with respect to an external electric field that was used for the new method developed in this thesis described in Chapter 5. The electronic energy of a chemical system at a frozen field-free equilibrium geometry under a static uniform electric field, $E^{el(0)}(\mathbf{F})$, can be expressed as a Taylor expansion series on the electric field strength:

$$E^{el(0)}(\mathbf{F}) = E^{el(0)}(\mathbf{0}) + \left(\frac{\partial E^{el(0)}(\mathbf{F})}{\partial \mathbf{F}}\right)\mathbf{F} + \frac{1}{2!}\left(\frac{\partial^2 E^{el(0)}(\mathbf{F})}{\partial \mathbf{F^2}}\right)\mathbf{F}\mathbf{F}... \tag{2.17}$$

For a static electric field, each derivative can be computed using the Finite-Field method (FF). This method is computationally efficient as it only requires the calculation of the energy of a system at several electric field strengths. Applying the FF method, the second derivative of the energy with respect to an external electric field (polarizability, α) can be calculated using the following equation:

$$\frac{\partial^2 E^{el(0)}(\mathbf{F})}{\partial \mathbf{F^2}} = \frac{E^{el(0)}(\mathbf{F}) + E^{el(0)}(-\mathbf{F}) - 2E^{el(0)}(\mathbf{0})}{\mathbf{F}^2} \tag{2.18}$$

While the finite-field method offers numerous advantages, its accuracy is highly sensitive to the chosen electric field strengths. The Romberg-Rutishauser (RR) method addresses this by iteratively correcting the results obtained with a specific field strength using information from derivatives calculated at higher field strengths [140]. In essence, the RR method tackles the truncation error, which arises because higher-order terms in the Taylor series expansion are neglected in the calculation of the numerical derivatives. By incorporating derivatives obtained at higher fields, RR refines the approximation and delivers more accurate results. Let me demonstrate the procedure defining *h* as:

$$h = \mathbf{F}/2^j \tag{2.19}$$

for some integer $j \geq 0$. In this context, h represents the different external electric field strengths applied to obtain the different energies used in the Romberg extrapolation method. For the particular case of the application of Romberg's approach to the calculation of the electronic polarizability, using Equation 2.18, it is defined:

$$R(j,0) = -\left(\frac{E(\mathbf{h}) + E(-\mathbf{h}) - 2E(\mathbf{0})}{\mathbf{h}}\right) \qquad \text{for } j \geq 0 \tag{2.20}$$

where *R(j,0)* represents the polarizability obtained using the FF method at different electric fields. To correct the truncation errors, the following expression is defined:

$$R(j,k) = \frac{4^k R(j,k-1) - R(j-1,k-1)}{4^k - 1} \qquad \text{for } j \geq \mathrm{k} > 0 \tag{2.21}$$

The values obtained from Equation 2.21 are commonly arranged in a triangular extrapolation table:

$$\begin{array}{cccccc}
R(0,0) & & & & & \\
R(1,0) & R(1,1) & & & & \\
R(2,0) & R(2,1) & R(2,2) & & & \\
R(3,0) & R(3,1) & R(3,2) & R(3,3) & & \\
\vdots & \vdots & \vdots & \vdots & \ddots & \\
\uparrow & \uparrow & \uparrow & \uparrow & & \\
O(h) & O(h^2) & O(h^3) & O(h^4) & &
\end{array}$$

where *O(h^n)* are the truncation errors avoided using this method. The advantage of this method is that the only expensive computations are in the first column, while the extrapolation procedure itself is simple arithmetic. In an ideal scenario without any other numerical errors, the bottom-right element in the table is expected to be the most accurate approximation. However, roundoff errors due to the finite precision of computers' numerical calculations can influence this tendency. To avoid such inconvenience, the criteria to choose the most accurate numerical derivative out of all the possible values given by this method is based on comparing the values of two consecutive field strengths along every iteration. The smallest difference determines which is the most accurate derivative.

CHAPTER 3

Objectives

In this thesis, various computational tools are used to study different areas of chemical science, such as thermodynamics, and electronic and infrared spectroscopy. Computational chemistry can offer a more precise description of some chemical processes compared to experimental methods, especially when certain properties can not be measured directly. Additionally, it provides a more detailed view of molecular electronic structures since the electron distribution can be easily calculated using quantum chemistry.

The thesis has two main general goals. The first one is the computational analysis of the stability of halogen bonding in complexes formed by BF/BF_2 dyes and perfluoro-haloarenes, as well as the study of its impact on the photophysical properties of the dyes. The specific objectives to achieve the first general goal are:

- Exploring the three-dimensional arrangements and relative thermodynamic stability of molecules in halogen-bonded complexes with BF/BF_2 organic dyes.
- Examining the changes in the electronic structure of halogen-bonded complexes, with a particular focus on the electron density distribution within BF/BF_2 dyes.
- Analyzing how halogen bonding impacts the optical properties of BF/BF_2 organic dyes, specifically their absorption and emission characteristics.

The second goal is the development and application of a new methodology to determine the physical origin of spectral feature changes in the infrared spectra upon the formation of molecular complexes. The specific objectives to achieve the second general goal are:

- Developing and implementing a new approach to split the changes in the infrared spectrum upon the formation of a molecular complex into terms with different physical origins using any energy decomposition analysis (EDA).
- Applying this approach to real systems to demonstrate its interpretative power in the analysis of the IR spectra of molecular complexes.

These objectives collectively contribute to advancing our understanding of halogen bonding and its role in shaping the spectroscopic properties of organic dyes.

CHAPTER 4

Effect of halogen bonding on spectroscopic properties of organic fluoroborates

In this section, I describe the results of the investigations in two series of boron-containing dyes interacting with perfluorohaloarenes, aiming to establish connections between their interaction patterns and resulting properties. I performed the computational analysis of this research to elucidate the measurements conducted by my group associates. Specifically, Judyta Zielak-Milewska (Nicolaus Copernicus University, Toruń) synthesized the **A**-dyes series and performed their NMR titration. Prof. Borys Ośmiałowski (Nicolaus Copernicus University, Toruń) synthesized the **B**-dyes series and performed the measurements of the electronic spectra of **A** and **B**-dyes series in different solvents. The NMR titrations for the **B**-dyes series were performed by Izabela Barańska (Nicolaus Copernicus University, Toruń). The infrared spectra of pyridine, C_6F_5I, and their mixture were measured by Dr. Tomasz Misiaszek (Wrocław University of Science and Technology, Wrocław).

The protocol applied for the simulations of the electronic structure in the ground and excited state of fluorescent dyes and their corresponding complexes is schematically illustrated in Figure 4.1. The initial phase of the applied protocol involved optimizing the ground state (GS) geometry of the dyes and their complexes using the MN15 hybrid density functional [141] combined with aug-cc-pVDZ basis set [142, 143]. For bromine and iodine atoms, the aug-cc-pVDZ-PP [144] basis set along with the corresponding pseudopotential was used to include scalar relativistic effects.

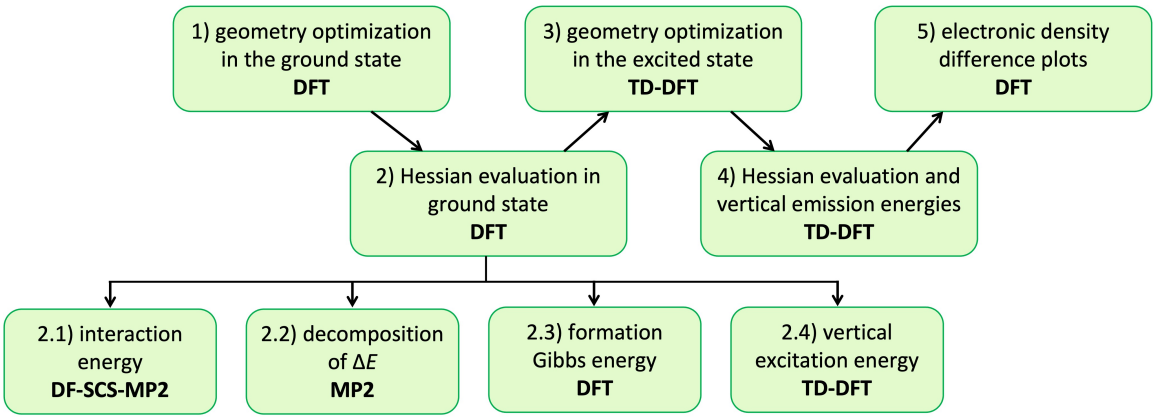

Figure 4.1: Protocol applied for the simulations of the structural features and electronic structure of fluorescent dyes and their complexes.

The optimization process was followed by the evaluation of the Hessian matrix to confirm that the resulting geometry corresponds to a minimum on the potential energy surface (PES). Optimizations and Hessian evaluation were performed using the Gaussian 16 program [145]. The equilibrium geometries were used as inputs for the interaction energies calculation at the SCS-MP2 level of theory using the density fitting method to improve the efficiency of the calculations. The DF-SCS-MP2 interaction energies were computed using the MOLPRO program [146]. Furthermore, to elucidate the origin of the interaction energy, the VP-EDS method at the MP2 level of theory was applied to decompose the interaction energy into terms with clear physical interpretation using a modified version of GAMESS (US) program [147]. To assess the thermodynamics of the complex formation, the output from the Hessian evaluation was used to compute the formation energy of the complexes. The ΔG was calculated as the difference between the Gibbs energy of the complex and the sum of the Gibbs energies of the isolated molecules. The correction when transitioning from standard-state gas-phase Gibbs energy at 1 atm to a solvent-phase with a specific concentration was added to the supermolecular approach used for ΔG. The ground state equilibrium geometries were used as inputs for electronic-structure calculations employing time-dependent density functional theory (TD-DFT) to determine the vertical excitation energies of the complexes. These calculations were performed using the MN15/aug-ccpVDZ(PP) level of theory using the Gaussian 16 program [145]. Furthermore, the geometry optimization of the complexes in the excited state employing TD-DFT was performed to determine the vertical emission energies of the complexes. The optimization process was followed by the evaluation of the Hessian matrix to confirm that the resulting geometry corresponds to a minimum on the potential energy surface. Using the equilibrium geometries in the ground and excited state and the electron density distribution in both geometries, the density difference plots for the vertical absorption and emission processes were obtained using the *cubegen* and *cubman* utilities from the Gaussian pro-

gram. This protocol can be used in simulations of the electronic structure of fluorescent dyes and their complexes in both the ground and excited states. By analyzing these density difference plots for the vertical, it is possible to pinpoint the specific influence of halogen bonding on the observed changes in absorption and emission spectra.

I will now discuss the set of dyes studied in this chapter. These dyes have been designed to promote XB and intramolecular charge transfer (ICT) in their lowest excited state (Figure 4.2). They feature the N–BF(–O)$_2$ fragment as the electron acceptor and a N,N-dimethylaniline group with the dimethylamino acting as the electron donor. The molecules have been designed in such way that the halogen bond acceptor is distinct from the primary electron acceptor involved in ICT. This ensures that shifting the nitrogen position does not significantly alter the intrinsic electronic structure of the dye. As a result, the effects of intermolecular interactions on the dyes' photophysical properties can be isolated. The solvents used in this study are also shown in Figure 4.2.

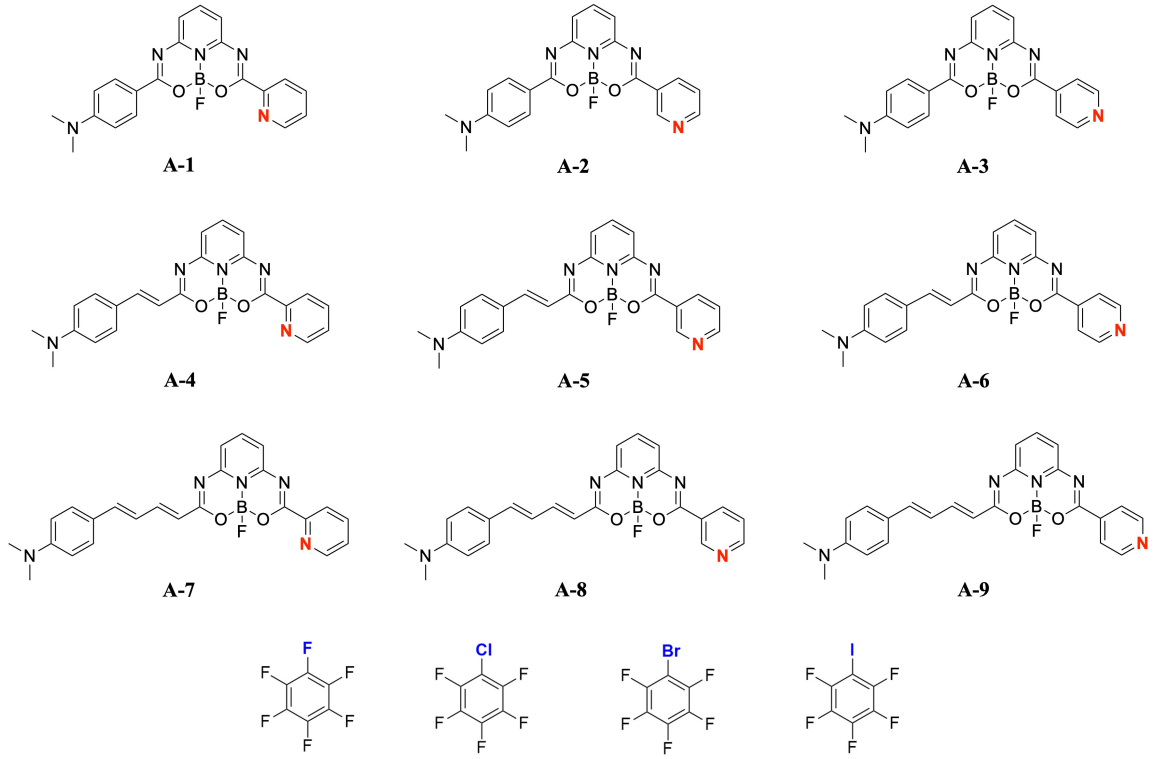

Figure 4.2: Studied compounds of the series **A** and the solvents used.

Unlike many studies on halogen bonding in solutions using electronic spectroscopy, a non-competitive environment has been employed in the research described here. Within this approach, the solvent itself acts as the halogen bond donor. The designed series of dyes **A** features a pyridyl moiety as the halogen bond acceptor, linked to the N–BF(–O)$_2$ core by a single C–C bond. The N,N-dimethylaniline group is linked to the N–BF(–O)$_2$ core by a single C–C bond (**A-1**, **A-2**, and **A-3**), vinyl group (**A-4**, **A-5**, and **A-6**)

or butadienyl group (**A-7**, **A-8**, and **A-9**). These linkers aimed to extend the conjugation within the system and potentially influence the photophysical properties. While extending conjugation through vinyl or butadienyl groups could be significant, it also introduces a potential drawback: cis-trans photoisomerization. This phenomenon, while interesting for photochromic applications, is undesirable for the current study as it could complicate the interpretation of the results. Therefore, the synthesis of dyes containing these linker groups was not pursued.

Building on prior research on two-photon absorption in diazines [55], the experimental efforts of this research were focused on the isomer with the additional nitrogen atom in position 5 of the *heterocyclic* ring giving the 4-aminopyrimidine derivative (**A-3**). This specific isomer has been shown to exhibit the highest fluorescence quantum yield in previous studies. The decision to focus on the **A-3** dye was driven by two key considerations. First, the position of nitrogen in the dye substituted containing a pyridin-4-yl introduces a very sensitive probe for any interaction, a feature strengthened by the second argument. Second, the free rotation of the nitrogen-containing moiety would not lead to the formation of multiple, energetically similar conformations. This factor eliminates a potential complication in interpreting the results. While the experimental measurements were performed solely on the **A-3** dye, computational modeling encompassed the entire set of dyes (**A-1** to **A-9**). For the dyes containing a conjugated linker, I considered only their trans conformation. The theoretical part of this study aimed to synergically complement measurements with more data which is not feasible to access experimentally. This comprehensive computational analysis is crucial in achieving the goals of this study. Specifically, it allows us to explore the formation of a halogen bond between the dye and the solvent molecule and analyze the influence of this halogen bond on the photophysical properties of the dyes.

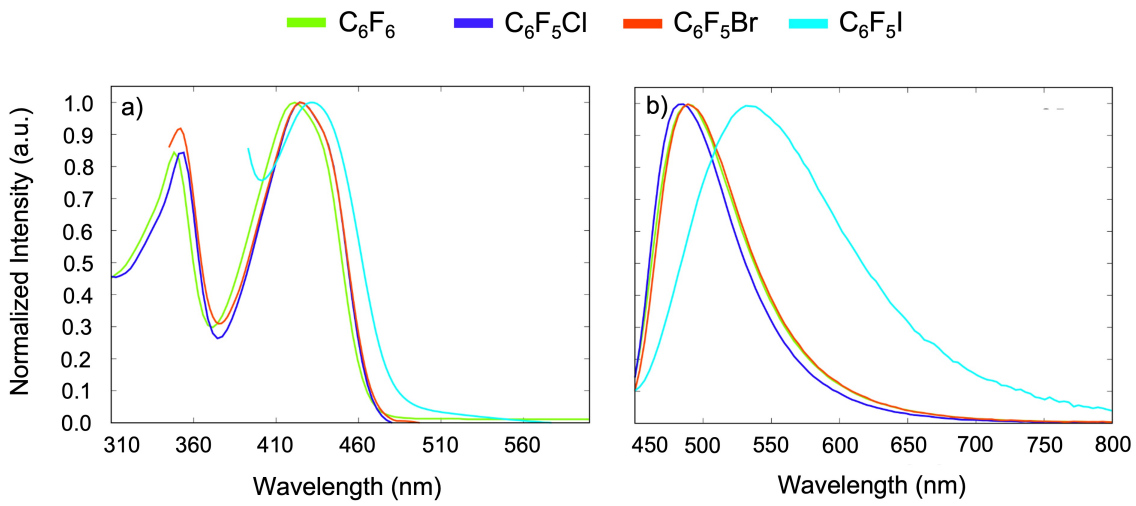

Figure 4.3: Normalized (a) absorption and (b) fluorescence spectra of **A-3** in C_6F_6, C_6F_5Cl, C_6F_5Br, and C_6F_5I as solvents.

Having established the systems considered in the first part of this study, let me shift the attention to the electronic absorption and fluorescence spectroscopy measurements conducted by my research associates. Figure 4.3 illustrates (a) the electronic absorption and (b) emission spectra of **A-3** in C_6F_6, C_6F_5Cl, C_6F_5Br, and C_6F_5I as solvents. The absorption spectra of C_6F_5Br and C_6F_5I have been cut around 349 nm and 390 nm, respectively, due to the strong absorption of the respective solvents. Consistent with the intramolecular charge transfer character of these organic fluoroborate dyes, the absorption spectra of **A-3** recorded in all four solvents display broad absorption bands lacking any well-resolved vibrational structure. Interestingly, a slight red shift is observed in the maximum absorption band of **A-3** measured in the C_6F_5I solvent compared to C_6F_6. This red-shifting trend becomes even more pronounced in the emission spectra of **A-3** dye in C_6F_5I solvent when using C_6F_6 as a reference. In the iodinated solvent, the emission band appears significantly broader and exhibits a more substantial red shift compared to the corresponding absorption band when using C_6F_6 as a reference. Furthermore, the changes observed in the emission bands for the other solvents with respect to C_6F_6 are much less significant.

To elucidate the reasons for these observations, my group associates measured the emission spectra of the dyes in C_6F_5Cl, C_6F_5Br, and C_6F_5I as solvents at various temperatures (Figure 4.4). These spectra reveal a clear distinction between C_6F_5I and the other solvents (C_6F_5Cl and C_6F_5Br).

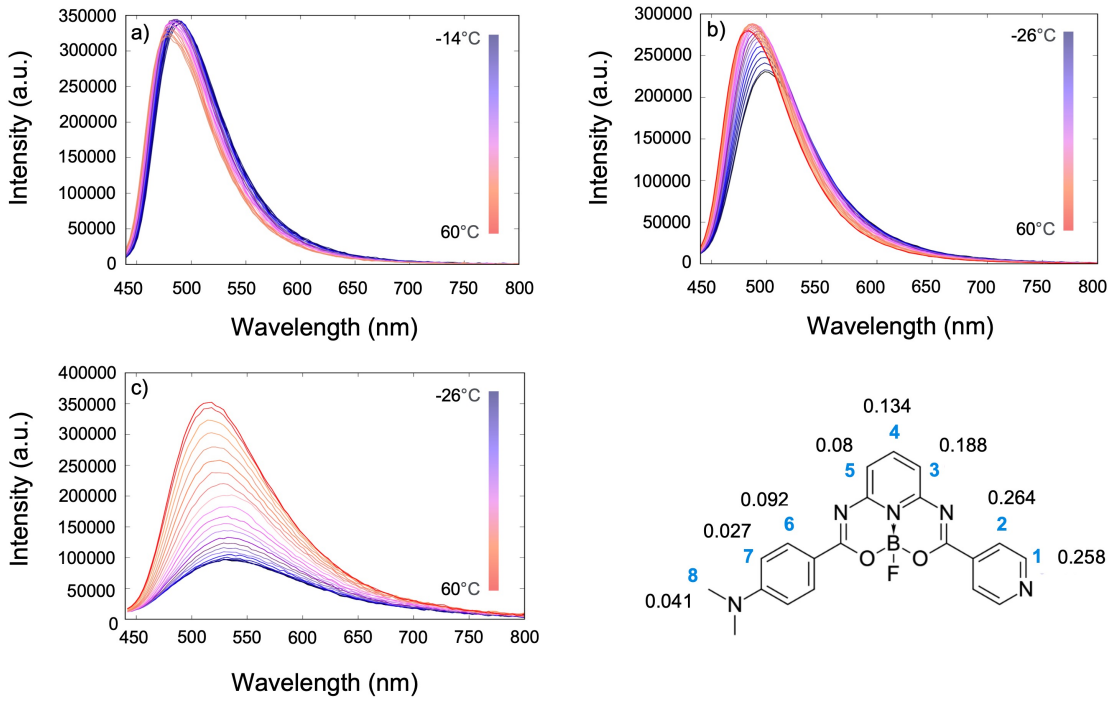

Figure 4.4: Fluorescence spectra of **A-3** recorded in (a) C_6F_5Cl, (b) C_6F_5Br, and (c) C_6F_5I as solvents in different temperatures, and CIS values for the protons of **A-3** obtained by the NMR titration by addition of C_6F_5I in C_6F_6 solution.

The fluorescence intensity in C_6F_5I exhibits a significantly stronger response to temperature changes compared to the other two solvents. Interestingly, the emission intensity is lowered when the temperature decreases, which is opposite to the typical behavior of fluorophores. One reason for this behavior may be an additional stabilization of the complex in the excited state at a lower temperature and fluorescence quenching within the complex.

To further elucidate the interaction between **A-3** and C_6F_5I, titration experiments using nuclear magnetic resonance (NMR) spectroscopy were performed. The stacked spectra for the titration of compound **A-3** with C_6F_5I in a C_6F_6 solution are provided in Figure S6.1. From this data, the association constant and the complexation-induced shift (CIS), defined as the difference in chemical shift (δ [ppm]) between a specific proton in the free dye molecule and the corresponding proton in the dye-solvent complex at saturation, have been determined. Figure 4.4 depicts the labeled protons in dye **A-3** along with their corresponding CIS values. The largest CIS values correspond to protons **1** (0.258 ppm) and **2** (0.264 ppm), which are located in the vicinity of the halogen bond acceptor site. Conversely, protons further away from this site exhibit significantly lower CIS values (below 0.09 ppm). The association constant (K_a = 750 M^{-1}) can be considered as moderate in magnitude for XB systems [148]. Together with the CIS values, these results strongly support the formation of a halogen bond interaction between the ground state of dye **A-3** and C_6F_5I. Additionally, Figure 4.5 depicts the far infrared spectrum (FIR) measured in the 100-600 cm^{-1} range for (a) pyridine, which represents the halogen bond acceptor moiety of dyes **A**, (b) C_6F_5I, and (c) their 1:1 mixture.

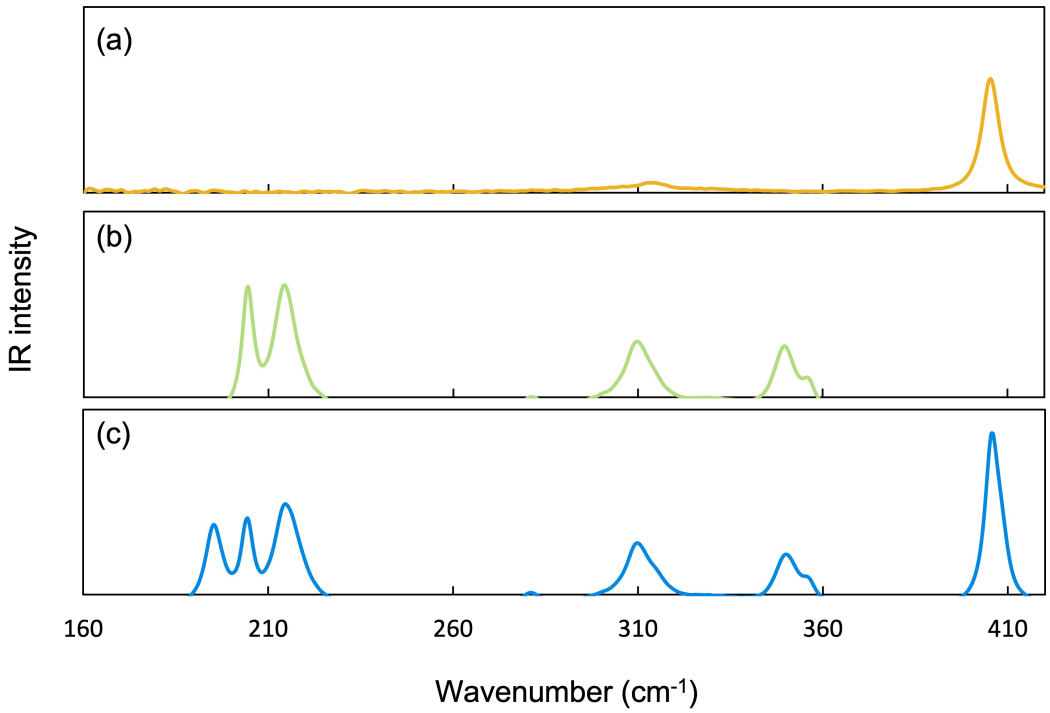

Figure 4.5: Measured far IR spectra for (a) pyridine, (b) C_6F_5I, and (c) their 1:1 mixture.

Interestingly, a new band appears at 195 cm $^{-1}$ when the complex is formed (Figure 4.5c) and has been assigned to the I$\cdots$N stretching demonstrating the formation of an XB complex between the pyridine and the C_6F_5I.

The theoretical component of this study complements the experimental findings by providing insights that are not readily obtainable through laboratory measurements. The main goal is to take advantage of computational modeling to support the experimental evidence for halogen bonding's influence on the electronic spectra of the **A** dyes and rationalize the observed spectral changes. To achieve this, I followed the protocol described in Figure 4.1, performing the optimization and electronic structure calculations for the complexes formed between the **A**-series dyes and the perfluorohaloarene solvents. However, before discussing the photophysical properties of the dyes in the different solvents, let me describe the structural and energetic features observed during the optimization of the **A**:C_6F_5X complexes. To understand the structures of these complexes and achieve accurate computational reproductions of the experimental measurements, I investigated and classified different groups based on the type of intermolecular interaction present.

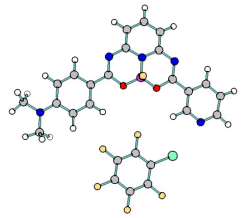

A-2:C_6F_5Cl

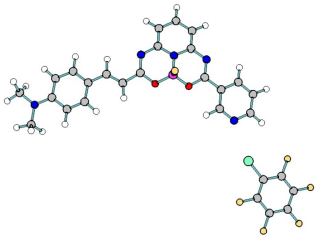

A-5:C_6F_5Cl

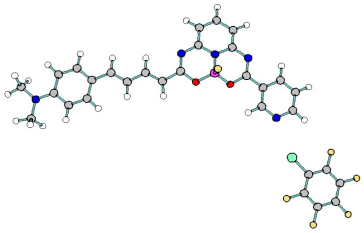

A-8:C_6F_5Cl

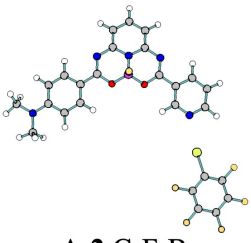

A-2:C_6F_5Br

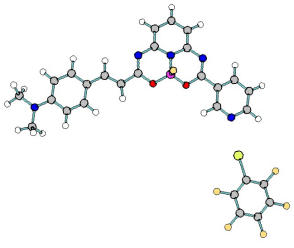

A-5:C_6F_5Br

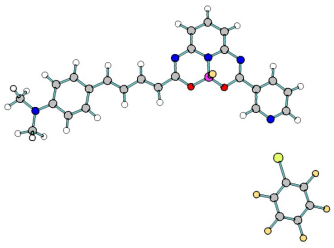

A-8:C_6F_5Br

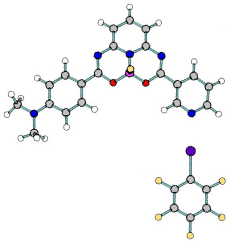

A-2:C_6F_5I

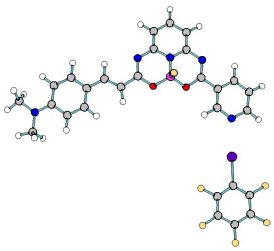

A-5:C_6F_5I

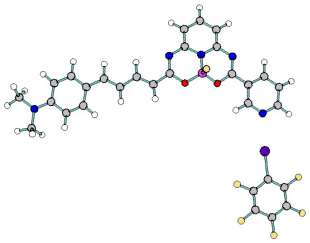

A-8:C_6F_5I

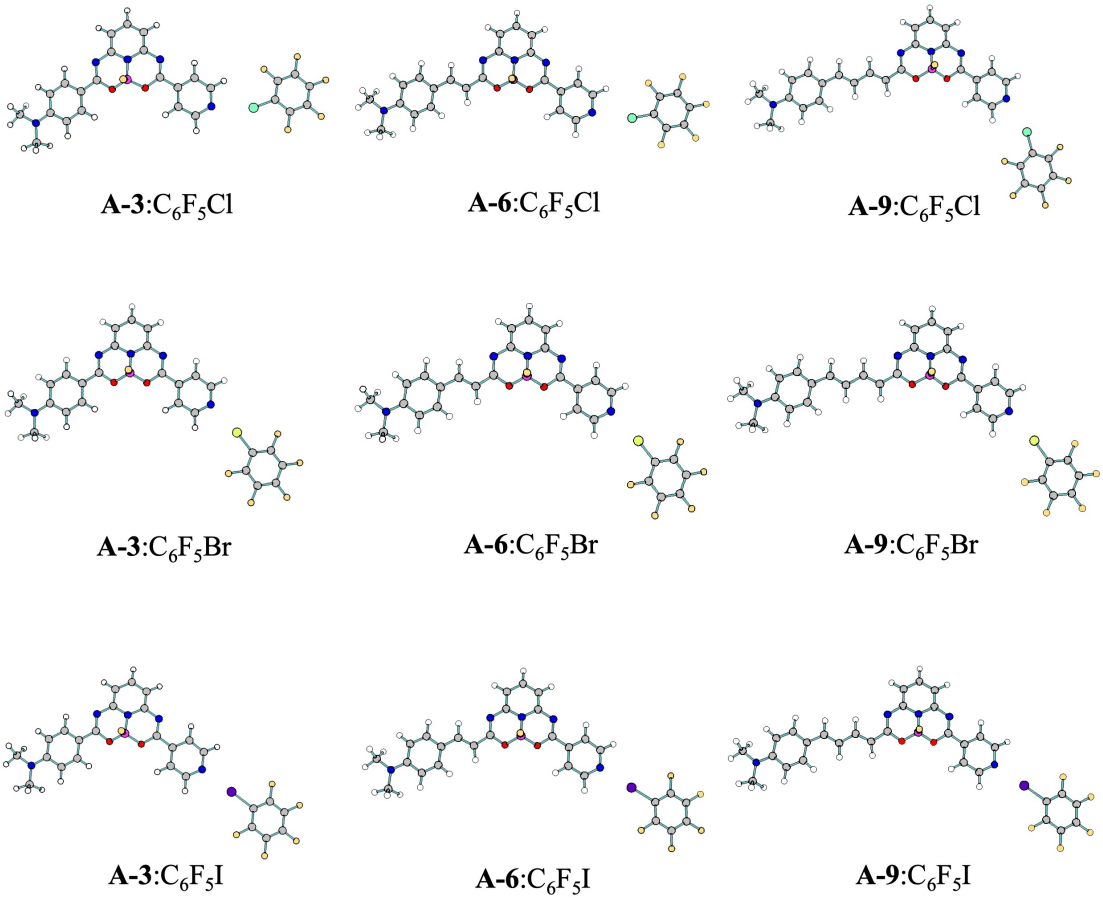

Figure 4.6: Computed equilibrium geometries of the 18 complexes classified as group 1 formed by halogen bonding. The geometries were obtained using the MN15/aug-cc-pVDZ(PP) level of theory.

The first group identified (group 1) comprises complexes formed through halogen bonding intermolecular interactions. This group is particularly intriguing for this work and encompasses 18 complexes in total (Figure 4.6). These complexes involve dyes with the nitrogen atom at positions 3 or 4 of the halogen bond acceptor site when counting from the point of heterocycle attachment to the core of the dyes, interacting with various perfluorohaloarenes excluding C_6F_6. Given the focus of this thesis, I dedicated the analysis primarily to understanding these halogen-bonded complexes. Interestingly, the C–X$\cdots$N angle exhibits significant variations depending on the specific halogen atom involved. Complexes containing C_6F_5Cl display the largest deviation from linearity, while those containing C_6F_5I form a near-perfect 180° angle. Complexes with C_6F_5Br fall between these two extremes, which agrees well with established trends in halogen bonding: stronger halogen bonds tend to be more linear. My calculations also reveal that the linker separating the electron donor and acceptor moieties generally has minimal influence on the halogen bond complexes' structural features. However, some exceptions exist, including the **A-2**:C_6F_5Cl complex.

The second group (group 2) consists of complexes in stacked arrangements stabilized mainly by dispersion interactions. This group comprises 12 complexes (Figure S6.2), involving dyes where the nitrogen atom resides at position 2 of the halogen bond acceptor site, again counting from the bond between heterocycle and central core (**A-1**, **A-4**, and **A-7**). Interestingly, π–stacking is observed for these dyes with all perfluorohaloarenes except C_6F_6. For dyes **A-3**, **A-6**, and **A-9**, π–stacking interactions were also obtained with C_6F_6.

The third group (group 3) encompasses the remaining complexes. These involve dyes with the nitrogen atom either at positions 2 or 3 of the halogen bond acceptor site, interacting with the C_6F_6 molecule. Complexes within this group exhibit various intermolecular interactions beyond halogen bonding and π–stacking (Figure S6.3).

Since the primary focus of this thesis is halogen bonding, my in-depth analysis concentrates on the first group of complexes. I used the equilibrium geometries of complexes of group 1 to compute the interaction energy using the wave function-based DF-SCS-MP2 method. The interaction energies at the DF-SCS-MP2 level are presented in Table 4.6. The results for complexes classified in groups 2 and 3 are presented in the supplementary information (Table S6.1) for reference purposes and will not be discussed in detail within the main body of the text. Focusing on the halogen-bonded complexes, the calculated interaction energies follow the well-established trend observed in typical halogen-bonded systems. Complexes where the iodine atom acts as the halogen bond donor exhibit the most negative (most stable) interaction energies, regardless of the specific **A** dye involved. This trend is followed by bromine and chlorine atoms as the halogen bond donor, respectively. Interestingly, the interaction energies for complexes formed by the same halogen bond donor display remarkable similarity across all the studied dyes. For example, the difference between the most negative and least negative interaction energies for complexes formed with C_6F_5I is less than 0.25 kcal/mol.

Table 4.1: Intermolecular interaction energy (ΔE, in kcal/mol) computed using DF-SCS-MP2 method and the aug-cc-pVDZ(PP) basis set.

	A-2	**A-3**	**A-5**	**A-6**	**A-8**	**A-9**
C_6F_5Cl	-3.28	-2.33	-2.38	-2.41	-2.32	-2.38
C_6F_5Br	-3.97	-4.03	-3.96	-4.05	-3.96	-4.02
C_6F_5I	-6.32	-6.41	-6.28	-6.43	-6.21	-6.42

From now on, and to effectively illustrate the key findings from the obtained results, I will focus on a specific subset of dyes: **A-2**, **A-3**, and **A-6**. These three dyes have been selected due to their distinct structural features that allow to explore various aspects of the halogen bonding interaction and its influence on photophysical properties. Dye **A-2** possesses a nitrogen atom at position 3 within the heterocyclic moiety and lacks a vinyl group

as a spacer linker. In contrast, dye **A-3** carries the nitrogen atom at position 4 within the heterocycle and does not include a vinyl linker, similar to **A-2**. Dye **A-6** also features a nitrogen atom at position 4, but it incorporates a vinyl group as a spacer linker, differentiating it from the other two dyes. By comparing **A-2** to **A-3**, it is possible to investigate how the position of the XB interaction affects the photophysical properties of compounds within the **A**-series. On the other hand, comparing **A-6** to **A-3** allows for the examination of the impact of extending the distance between the electron-acceptor group in the charge transfer pathway and the XB acceptor on the photophysical properties of the compounds within the **A**-series.

To gain further insights into the energetic contributions within the complexes, I employed Variational Perturbation Energy Decomposition Analysis (VP-EDS) for complexes formed by the three dyes (**A-2**, **A-3**, and **A-6**) with different solvents. It is important to note that VP-EDS is not implemented with the density-fitting approach. Consequently, the computational demands associated with the system size do not allow a complete partitioning of the interaction energy (ΔE) for **A**:C_6F_5X complexes at the MP2 level of theory. Therefore, I focused on partitioning the HF contribution to the interaction energy ($\Delta E_{int}^{\mathrm{HF}}$) into its components: electrostatics ($\varepsilon_{el}^{(10)}$), exchange-repulsion ($\Delta E_{ex}^{\mathrm{HL}}$), and delocalization ($\Delta E_{del}^{\mathrm{HF}}$). The remaining terms have been grouped under the MP2 correlation term ($\Delta E_{corr}^{\mathrm{MP2}}$), which can be calculated by subtraction of $\Delta E_{int}^{\mathrm{HF}}$ from $\Delta E_{int}^{\mathrm{MP2}}$ obtained at the DF-SCS-MP2/aug-cc-pVDZ(PP) level of theory. The partitioning of the interaction energy for the selected systems is presented in Figure 4.7 and Table S6.2. The results are ordered according to the increasing value of the total interaction energy.

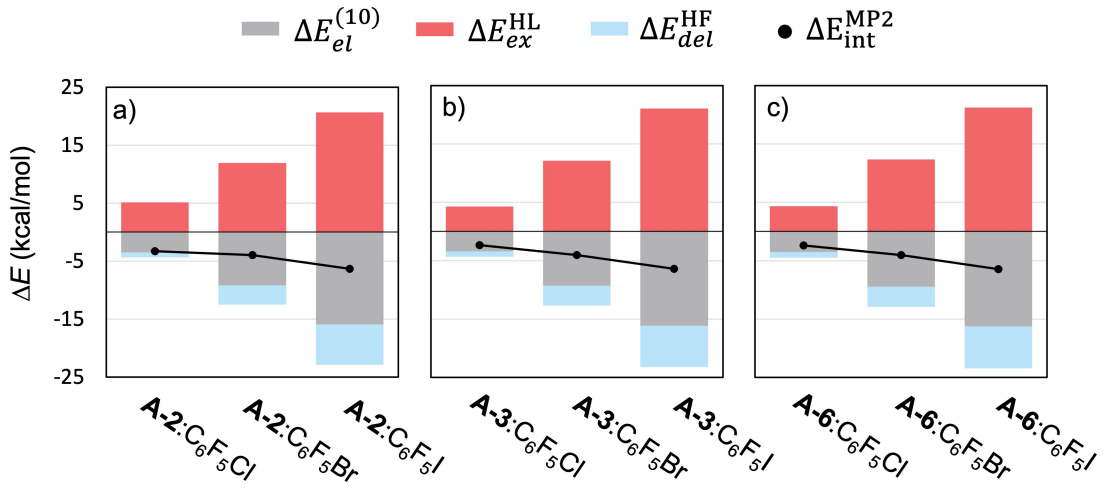

Figure 4.7: Partitioning of the HF interaction energy ($\Delta E_{int}^{\mathrm{HF}}$) of (a) **A-2**:$C_6F_5X$, (b) **A-3**:$C_6F_5X$, and (c) **A-6**:$C_6F_5X$ complexes at the equilibrium geometries at the MP2/aug-cc-pVDZ(PP) level of theory. The black dots combined with black lines indicate the total MP2 interaction energy computed using the DF-SCS-MP2 method.

Interestingly, the analysis of the ΔE decomposition reveals similar trends within each dye across the different perfluorohaloarene, regardless of the specific dye involved in the complex formation. This observation suggests that the primary driving force behind the intermolecular interaction originates from the type of interaction itself (in this case, halogen bonding). A closer look at the individual components reveals that the exchange-repulsion term makes the largest contribution, destabilizing the complexes. However, this destabilization is counterbalanced by the combined effects of electrostatics and delocalization, which both contribute significantly to stabilizing the complexes. Thus, the negative total interaction energy highlights the importance of including the electron correlation for accurate prediction of the total interaction energy, which implies that dispersion effects play a crucial role in defining the nature of halogen bonding. These results are consistent with previous studies conducted by some of my group associates [149].

To further emphasize the value of EDA in elucidating the nature of intermolecular interactions, I examined the partitioning of ΔE for complexes formed through π–stacking interactions. An example of these complexes involves the π system of dye **A-4** interacting with the π system of the perfluorohaloarenes. The results are presented in Figure 4.8 alongside the corresponding equilibrium geometries and Table S6.2.

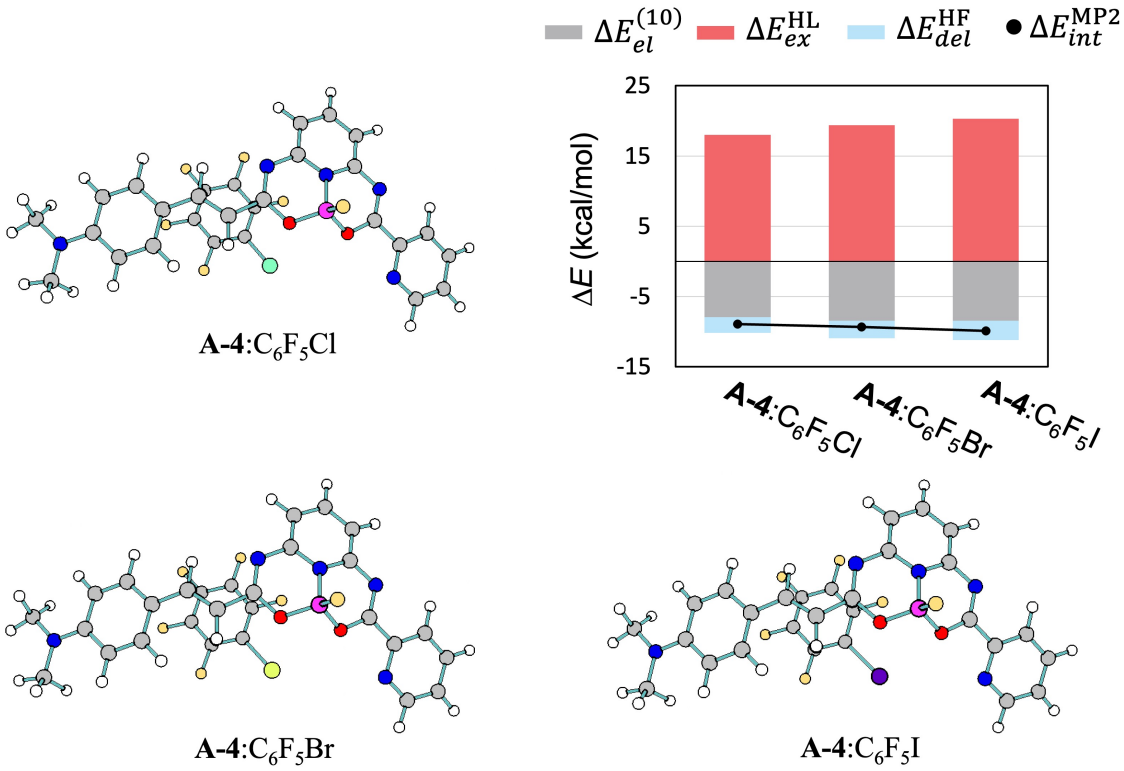

Figure 4.8: Equilibrium geometries of **A-4**:C_6F_5X complexes computed at the MN15-/aug-cc-pVDZ(PP) level of theory, and their corresponding partitioning of the interaction energy. The black dots combined with black lines indicate the total MP2 interaction energy computed using the DF-SCS-MP2 method.

Comparing these findings with the partitioning data for halogen-bonded systems (Figure 4.7) leads to significant differences observed in the relative contributions of the individual terms. In π–π stacked arrangements, the exchange-repulsion term exhibits a more pronounced contribution compared to halogen-bonded systems. Additionally, the combined effect of electrostatics and delocalization is weaker than the exchange-repulsion term in π–stacking complexes. Despite this observation, the MP2 interaction energies are negative for all three π-stacking complexes, indicating that the dispersion term, included in the MP2 correlation terms, is essential for an accurate assessment of such molecular interactions. The partitioning of interaction energies across the different π-stacking complexes is remarkably similar. This suggests that the dominant force underlying the interaction between **A-4** and the C_6F_5X perfluorohaloarenes through π-stacking is independent of the specific halogen atom involved.

Before performing the analysis of the computed photophysical properties of the complexes, I have compared the interatomic distances within the N$\cdots$X bond in the ground and excited equilibrium geometries for the **A-2**, **A-3**, and **A-6** compounds interacting with the C_6F_5X molecules. The differences between the halogen bond lengths of each complex in the ground (S_0) and excited (S_1) state are illustrated in Figure 4.9. Interestingly, all complexes exhibit a shortening of the bond length upon excitation, with the most significant changes observed in the **A-3**:C_6F_5X complexes. Furthermore, the extent of this bond length change correlates with the polarizability of the halogen atom in the halogen bond donor. In all complexes, the largest variation is observed for C_6F_5I (most polarizable halogen), while the smallest shift occurs for C_6F_5Cl (least polarizable halogen). According to the theory of halogen bonding, these shortenings of the intermolecular bond distance suggest a strengthening of the intermolecular interaction upon excitation of the complex.

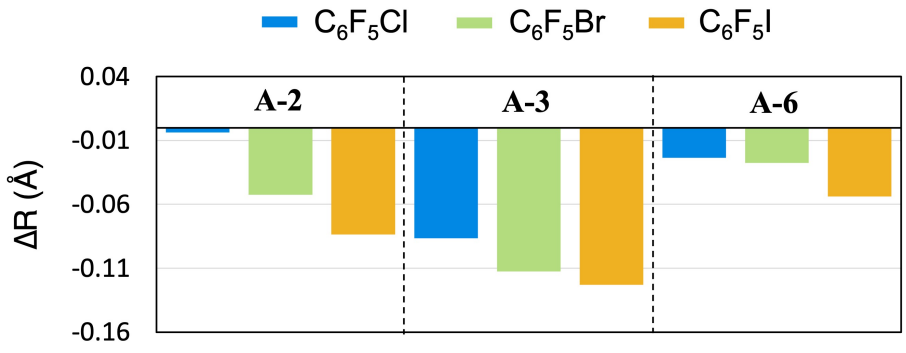

Figure 4.9: Differences in the length between the N$\cdots$X bond distance in the excited state equilibrium geometry and the N$\cdots$X bond distance in the ground state equilibrium geometries of the set of **A**:C_6F_5X complexes studied.

Once the structural aspects of the complexes studied in this thesis have been discussed, I will focus my analysis on the results obtained from the electronic structure calculations in order to support the experimental measurements. The summary of the calculated electronic

absorption and emission spectra of **A-2**, **A-3**, and **A-6** in C_6F_5X solvents is collected in Table 4.2. The calculations to obtain these results have been performed in the gas phase. This decision was based on the observation that the implicit solvation model (PCM) using C_6F_6 and C_6F_5I predicts a minimal change (only 7 nm) in the dyes' emission. The C_6F_5I solvent effect was simulated using a dielectric constant 5.6 [150] within PCM. Due to the results obtained, the effect of solvent polarity has been considered negligible. Furthermore, the calculations of the isolated dye in the gas phase, indicated as *not present* in the table, have been used as analogous to experimental measures in the C_6F_6 solvent.

Table 4.2: Summary of electronic structure calculations of **A-2**, **A-3**, and **A-6** in various solvents at TD-DFT level. Maximum absorption wavelength (λ_{abs}), maximum emission wavelength (λ_{em}), oscillator strengths (f), and Stokes shift. Values in bold were measured at r. t.

Compound	Halogen bond donor	λ_{abs} nm	f	λ_{em} nm	f	Stokes shift cm-1
A-2	not present	378	0.68	418	0.55	2532
	C_6F_5Cl	381	0.60	422	0.46	2550
	C_6F_5Br	382	0.66	432	0.43	3030
	C_6F_5I	384	0.61	444	0.34	3519
A-3	not present	381	0.64	431	0.43	3045
	C_6F_6	**420**		**490**		**3400**
	C_6F_5Cl	382	0.68	437	0.43	3295
		425		**484**		**2870**
	C_6F_5Br	385	0.64	454	0.34	3948
		425		**493**		**3245**
	C_6F_5I	388	0.64	473	0.28	4623
		430		**539**		**4702**
A-6	not present	401	1.17	443	1.23	2364
	C_6F_5Cl	402	1.22	443	1.27	2302
	C_6F_5Br	405	1.19	444	1.22	2169
	C_6F_5I	407	1.20	447	1.09	2199

The analysis of the electronic structures of the excited states reveals interesting findings. I will examine the theoretical results for the **A-3** dye in the first place and compare them directly to the corresponding experimental measurements. The trends observed in the calculated absorption spectra for all the complexes are consistent with the experimental data. This indicates a minimal change in the wavelength corresponding to the maximum absorption when the perfluorohaloarene is varied. Similar to the experimental observations, the largest shift in the theoretical absorption maxima is predicted between the isolated **A-3**

dye and **A-3**:C_6F_5I complex. Furthermore, the red shift of the calculated emission wavelengths correlates with the established trend in halogen bond strengths (Cl < Br < I).

To elucidate the reasons behind the observed results, Figure 4.10 illustrates the difference in electron density ($\Delta\rho$) between the ground and excited electronic states at (a) the GS geometry and (b) the ES geometry of the **A-3**:C_6F_5I complex. The two panels of Figure 4.10 offer insights into the changes in electron density during the excitation and emission processes in the **A-3**:C_6F_5I complex. Figure 4.10a depicts the difference in electron density upon absorption (vertical transition). In this process a relatively small change in the density around the N$\cdots$I bond is observed, suggesting a minimal influence of the halogen bond on the absorption process.

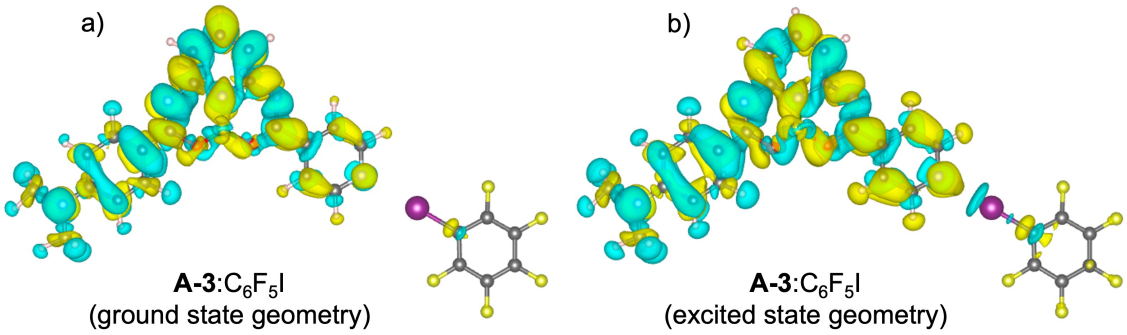

Figure 4.10: Electron density difference between the excited and ground states of the (a) absorption and (b) emission process for the **A-3**:C_6F_5I complex. In blue the regions with decreased electron density, and in yellow the regions with increased electron density.

Figure 4.10b illustrates the difference in electron density during emission. In contrast to the absorption process, a significant change in density is observed across the N$\cdots$I bond, suggesting a pronounced influence of the halogen bond on the emission process. These findings highlight that the emission wavelength is more sensitive to the effect of the halogen bond compared to the absorption wavelength and explain the differences observed in the measurements.

Although the TD-DFT calculations generally agree well with experimental observations, a notable discrepancy arises in the emission spectra of **A-3**:C_6F_5Cl and **A-3**:C_6F_5Br complexes. Experimentally, the emission maxima in C_6F_6, C_6F_5Cl, and C_6F_5Br show minimal shifts. Conversely, the theoretical spectra exhibit more pronounced shifts, reflecting the expected trend in halogen bonding strength. To investigate this discrepancy, I computed the Gibbs free energy (ΔG) for the formation of all studied complexes. This calculation includes a correction term to account for the experimental concentrations of reactants and products. The detailed methodology employed to obtain the results presented in Table 4.3 is provided in Chapter 2. Analysis of the ΔG values in Table 4.3 reveals that only the interaction between the dyes and C_6F_5I leads to an energetically favorable (exergonic) complex

formation due to halogen bonding. This suggests that only the C_6F_5I halogen bond donor forms thermodynamically stable complexes with **A**-dyes series under the studied conditions according to DFT calculations. In contrast, the positive ΔG values for complexes involving C_6F_5Cl and C_6F_5Br suggest that they are not energetically favorable under experimental conditions. This finding agrees well with the experimental observations, particularly explaining the significant spectral shifts observed for the **A-3** dye in C_6F_5I compared to C_6F_6, while minimal shifts are seen for C_6F_5Cl and C_6F_5Br solvents compared to C_6F_6 solvent. Consequently, the selectivity of the experiments is reproduced and rationalized by the DFT calculations.

Table 4.3: Corrected formation Gibbs energy (ΔG, in kcal/mol) taking into account the concentration of the reactants and product used in the measurements for **A**:C_6F_5X complexes.

	A-2	**A-3**	**A-5**	**A-6**	**A-8**	**A-9**
C_6F_5Cl	4.10	3.19	2.69	2.78	2.96	3.11
C_6F_5Br	0.62	0.50	0.56	0.68	1.05	0.41
C_6F_5I	-1.55	-1.71	-1.68	-1.96	-1.77	-2.47

While the ΔG values in Table 4.3 indicate favorable complex formation also for **A-2**:C_6F_5I and **A-6**:C_6F_5I, the photophysical response of **A-2** and **A-6** to halogen bonding differs from **A-3** as revealed by TD-DFT calculations. **A-3** exhibits a significantly larger red shift in its emission maximum wavelength upon complexation with C_6F_5I compared to **A-2** and **A-6**. The Stokes shift difference for **A-2** and **A-6** induced by C_6F_5I with respect to the isolated dye is substantially smaller than for **A-3** (1000 cm^{-1} and -100 cm^{-1}, respectively, vs. 1700 cm^{-1} for **A-3**). These observations suggest a weaker influence of halogen bonding on the electronic structure of **A-2** compared to **A-3** and a negligible impact on **A-6**.

To explain this observation, I computed the electronic density changes during the emission process of **A-2**:C_6F_5I and **A-6**:C_6F_5I complexes (Figure 4.11). By analyzing these changes, the observed discrepancies in the measured emission maximum wavelength shifts between **A-3**, **A-2**, and **A-6** upon solvent change from C_6F_6 solvent to C_6F_5I can be explained. The substantial emission maximum wavelength shift observed for **A-3**:C_6F_5I compared to the isolated dye (Table 4.2) correlates well with the significant change in density across the N$\cdots$I bond during emission in Figure 4.10b. Conversely, the smaller shift observed for **A-2**:C_6F_5I compared to **A-3**:C_6F_5I agrees with the considerably weaker density change over the N$\cdots$I bond in Figure 4.11a. These findings suggest that the position of the nitrogen atom in the halogen bond acceptor significantly impacts the influence of halogen bonding on the dyes' photophysical properties. Furthermore, the negligible change in emission maximum wavelength for **A-6** upon complex formation is rationalized by the

absence of density change over the N···I bond in Figure 4.11b. These results suggest that extending the conjugation system has a significant influence on the interplay between halogen bonding and the photophysical properties of the studied dyes. Specifically, the extension of the conjugation appears to neglect the influence of halogen bonding on the dye's intramolecular charge transfer.

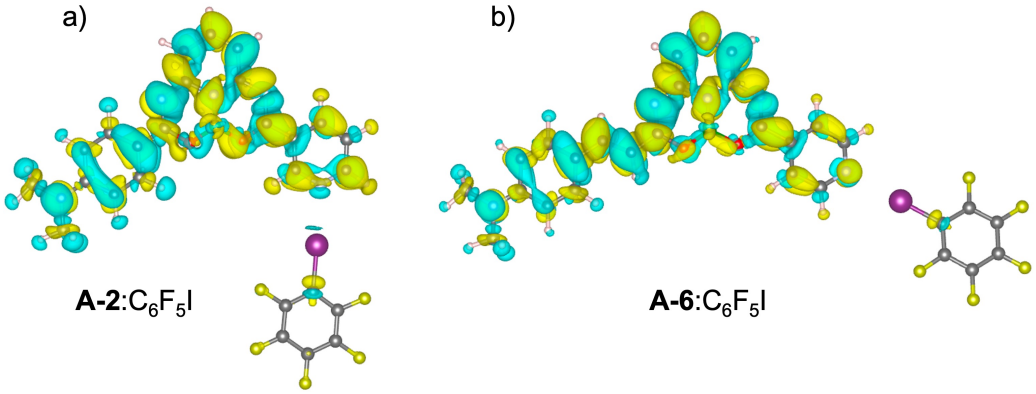

Figure 4.11: Electron density difference between the excited and ground states of the emission process for the (a) **A-2**:C_6F_5I and (b) **A-6**:C_6F_5I complexes. In blue the regions with decreased electron density, and in yellow the regions with increased electron density.

Having elucidated the halogen bonding effect in **A**-series dyes, I will now explore **B**-series dyes (Figure 4.12). These dyes have been designed to include the halogen bond acceptor positioned near the BF_2 acceptor within the CT path, unlike the complexes of the series **A** where it was distant from the CT path. **B**-series dyes possess a dipolar structure with an N–BF_2–O electron-accepting group and a dimethylamino electron-donor group connected by a single bond. Their design allows halogen bonding at two distinct sites: the *heterocyclic* nitrogen (red in Figure 4.12) and the *imine* nitrogen (green). As in measurements for series **A**, it is important to note that this work employs the solvent itself as the halogen bond donor.

Previous research on similar dyes examined their photophysical properties and revealed how changes in the nitrogen position impact these properties [55]. The study revealed that all the compounds studied exhibit 2PA within the first biological window, making them suitable for biological applications. The introduction of an additional nitrogen atom in the *heterocyclic* ring of these compounds leads to a redshift in the excitation wavelength. Moreover, the presence of the additional nitrogen atom enhances the magnitude of 2PA and demonstrates that the fluorescence quantum yield (FQY) can be modulated by strategically placing the nitrogen atom, allowing for controlled tuning of photophysical properties. Similarly, the present study investigates the effects of halogen bonding on the photophysical properties of compounds in series **B**. Before discussing the computational results, it is important to highlight the experimental characterization of the **B**-series dyes in C_6F_5X solvents performed by my group associates.

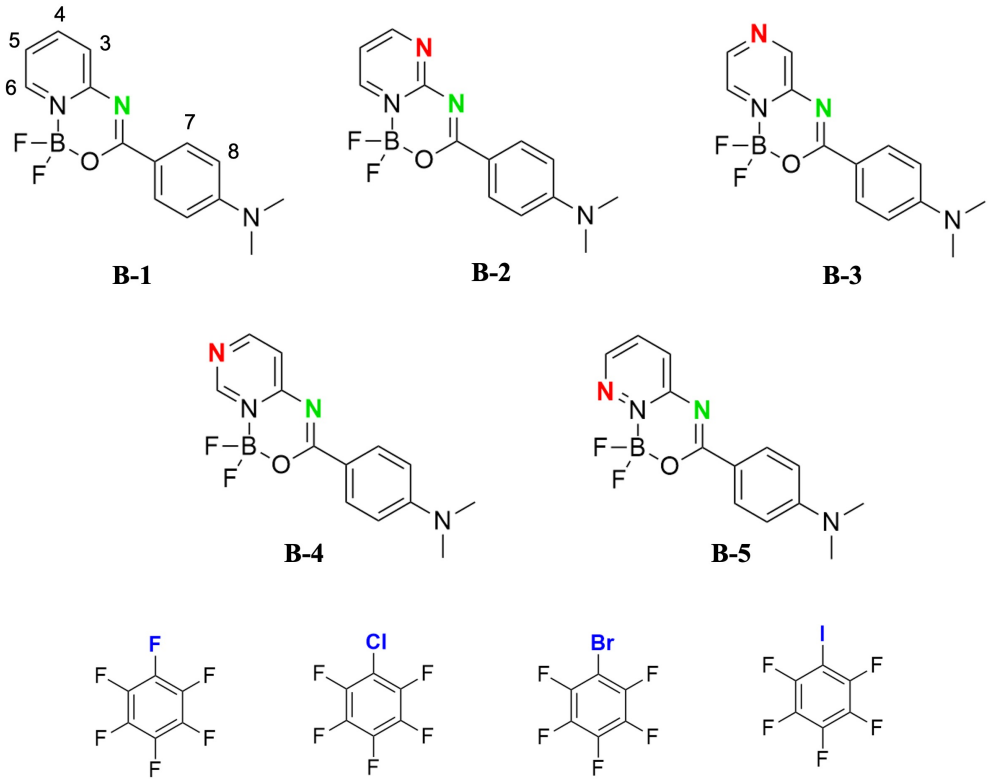

Figure 4.12: Studied compounds of series **B** and the solvents used.

The summary of the measurements of the absorption and emission spectra of dyes of series **B** is presented in Table 4.4. In agreement with earlier investigations on similar dyes, the position of the nitrogen atom on the *heterocyclic* ring significantly impacts the absorption maximum wavelength. In C_6F_6 solvent, varying the nitrogen position allows for tuning the absorption maximum wavelength (λ_{abs}) across the violet-blue range, from 393 nm for **B-1** to 420 nm for **B-3**. Furthermore, the trends in λ_{abs} with solvent changes remain consistent across all dyes. For instance, C_6F_5I consistently yields the highest λ_{abs}, while C_6F_5Cl yields the lowest one.

Figure 4.13a depicts the shift in the absorption maximum wavelength of **B**-series dyes in C_6F_5X with respect to the absorption maximum wavelength of **B**-series dyes in C_6F_6 solvents. Notably, **B-1** exhibits a minimal solvent effect on λ_{abs}. Interestingly, all dyes show a progressive redshift in the order $C_6F_5Cl < C_6F_5Br < C_6F_5I$, reaching a maximum 14 nm shift for **B-3** in C_6F_5I compared to C_6F_6. Additionally, the λ_{abs} difference between C_6F_5Cl and C_6F_5Br is smaller compared to C_6F_5Br and C_6F_5I, suggesting a stronger effect on absorption coming from C_6F_5I solvent. These results allow for the rational design of dyes using different solvents, allowing for the tuning of λ_{abs} across a wide color spectrum, reaching 435 nm for **B-3** in C_6F_5I. The emission maximum wavelength (λ_{em}) is more sensitive to environmental changes compared to the absorption maximum wavelength. This

is evident from the larger shifts observed for λ_{em} upon solvent changes in Figure 4.13b. For instance, **B-3** in C_6F_5I solvent exhibits a 60 nm red-shifted λ_{em} compared to measurements in C_6F_6 solvent.

Table 4.4: Summary of measured photophysical properties of **B** dyes in the palette of solvents studied. Maximum absorption wavelength (λ_{abs}), maximum emission wavelength (λ_{em}), fluorescent quantum yield (FQY), and Stokes shift.

Compound	Solvent	λ_{abs} nm	λ_{em} nm	FQY	Stokes shift cm^{-1}
B-1	C_6F_6	393	437	0.872	2562
	C_6F_5Cl	395	435	0.978	2328
	C_6F_5Br	397	438	0.860	2358
	C_6F_5I	401	452	0.078	2863
B-2	C_6F_6	398	472	0.357	3939
	C_6F_5Cl	400	465	0.466	3495
	C_6F_5Br	402	472	0.361	3689
	C_6F_5I	411	525	0.018	5283
B-3	C_6F_6	420	517	0.376	4467
	C_6F_5Cl	423	505	0.635	3839
	C_6F_5Br	425	517	0.592	4187
	C_6F_5I	435	578	0.037	5740
B-4	C_6F_6	407	455	0.920	2592
	C_6F_5Cl	409	452	1.000	2326
	C_6F_5Br	412	456	0.930	2342
	C_6F_5I	420	488	0.670	3318
B-5	C_6F_6	400	513	0.206	5507
	C_6F_5Cl	402	500	0.401	4876
	C_6F_5Br	404	502	0.409	4832
	C_6F_5I	411	555	0.052	6313

This shift is significantly larger than the 14 nm for λ_{abs} for the same system. Consequently, it is clear that the choice of the solvent and the position of the halogen bond acceptor can tune the λ_{em} for **B**-series dyes, ranging from 435 nm (**B-1**:C_6F_5Cl) to 578 nm (**B-3**:C_6F_5I). Furthermore, the trend in the emission maximum wavelength shifts for the set of dyes in C_6F_5I with respect to C_6F_6 agree with those observed in absorption (i.e., **B-1 < B-4 < B-2 < B-5 < B-3**). However, there are notable differences in the solvent's impact on each compound. Figure 4.13b reveals that while all compounds exhibit a substantial redshift in the emission maximum wavelength in C_6F_5I, a slight blueshift occurs in C_6F_5Cl

and C_6F_5Br for each compound. Furthermore, **B-1** dye, which only contains the halogen bond acceptor in the *imine* nitrogen, exhibits the smallest shift upon solvent change, suggesting XB occurring at the *heterocyclic* nitrogen site plays a pivotal role in the variations in the photophysical properties of series **B** dyes.

The Stokes shift observed for each dye in different solvents is summarized in Table 4.4. Smaller Stokes shifts for **B-1** and **B-4** indicate potentially weaker intramolecular charge transfer compared to other dyes. The largest Stokes shifts are observed in C_6F_5I for all **B**-series dyes, again suggesting that C_6F_5I interacts with the dyes via halogen bonding (XB) at the *heterocyclic* nitrogen site. This interaction likely affects the electronic structure of the dyes and promotes CT.

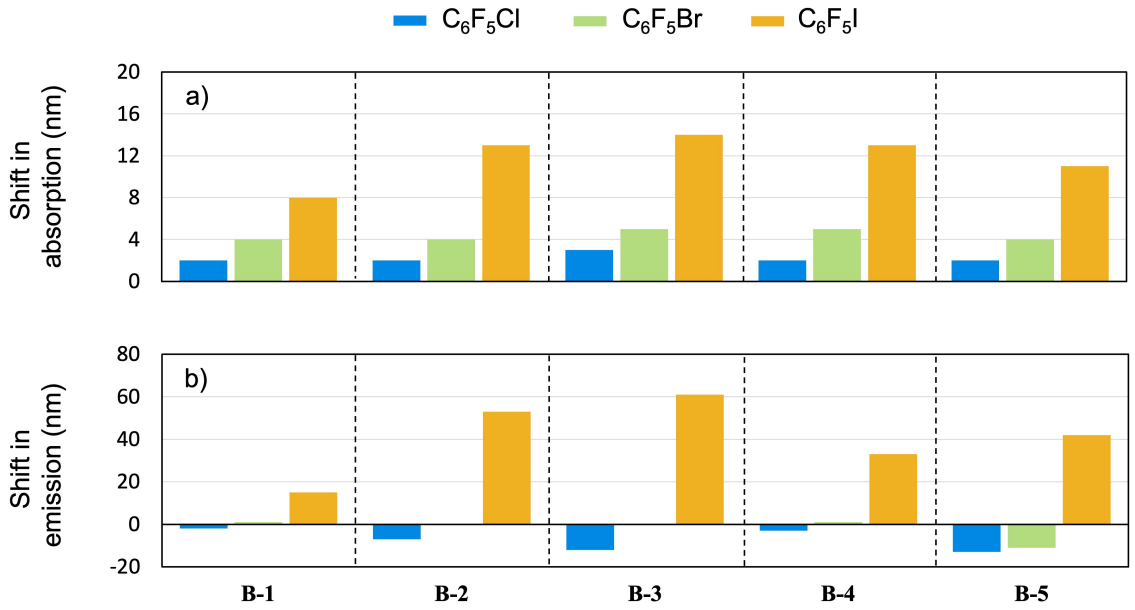

Figure 4.13: Changes in (a) absorption and emission (b) maximum wavelengths for **B**-series dyes in C_6F_5X with respect to C_6F_6 as solvents.

Several experimental techniques have been used to elucidate the structures of the complexes formed between the **B**-series dyes and C_6F_5X solvents, such as NMR. The C_6F_5X solvents can also interact with the **B**-series dyes through π-stacking, which may hinder the detection of halogen bonds. Therefore, the ^{1}H-NMR titrations by the addition of 1-iodononafluorobutane (C_4F_9I) in C_6F_6 were performed to study the halogen-bonding interaction, excluding **B-5** due to its low solubility. The complexation-induced shift (CIS) values have been calculated from the measurements and are depicted in Figure 4.14a. The results provide valuable insights into the interactions and behavior of the **B**-series dyes. The CIS values observed for protons 3 and 7 of **B-1** are remarkably large, suggesting significant XB interaction at the *imine* nitrogen atom. For other dyes (**B-2**, **B-3**, **B-4**, and **B-5**), in C_4F_9I, proton 7 exhibits the most significant CIS, highlighting its sensitivity to halogen-

bonding interactions. Then, my group associates performed the ^{1}H-NMR titrations by the addition of C_6F_5I in C_6F_6 solution (Figure 4.14b). The first observation from this titration is the low association constants of the dyes to the C_6F_5I molecules, which are below 10 M^{-1}. However, these observations are in agreement with previously published studies by Taylor et al. [151, 152] and can be explained by the strong electron-accepting properties of the BF_2 group that remarkably withdraw electron density from the halogen bond acceptor atom (nitrogen). This behavior disfavors the interaction between the nitrogen and the σ-hole of the halogen atom.

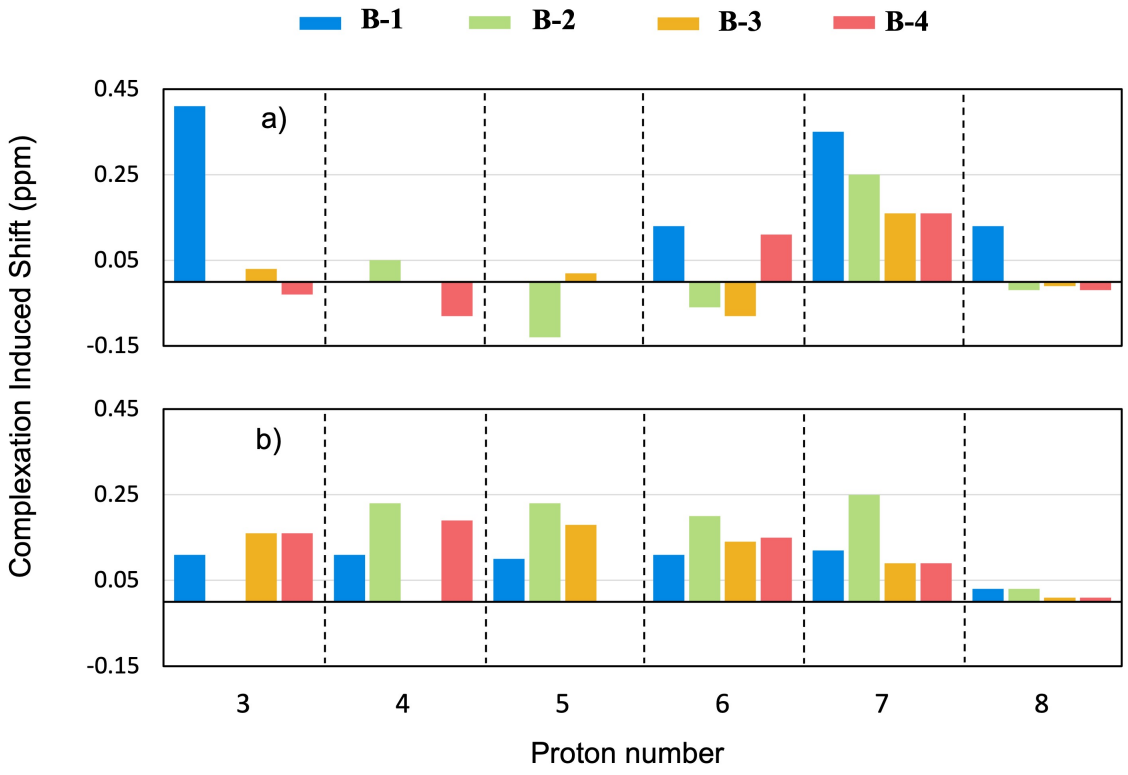

Figure 4.14: CIS values for every proton of **B-1**, **B-2**, **B-3**, and **B-4** obtained by the NMR titration by the addition of (a) C_4F_9I in C_6F_6 solution and (b) C_6F_5I in C_6F_6 solution. Proton labels are shown in Figure 4.12.

Although low association constants have been found, it is important to remark that their photophysical properties have been recorded in pure C_6F_5X solvents, ensuring that all the dye molecules are surrounded by solvent molecules acting as halogen bond donors. Furthermore, in C_6F_5I, which can interact with the dye through π-stacking, all protons show smaller shifts, with proton 8 exhibiting negligible changes. This pattern points toward a competitive balance between halogen bonding and π-stacking effects.

To further investigate the electronic environment of the nitrogen atoms, ^{1}H-^{15}N HMBC NMR spectroscopy for all **B**-series dyes except **B-1** because of its lack of *heterocyclic* nitrogen, and **B-5** due to its low solubility was performed. Table 4.5 summarizes the ^{15}N

chemical shift changes in C_6F_5I compared to C_6F_6. The data reveals shielding effects for the *heterocyclic* nitrogen in **B-2**, **B-3**, and **B-4**, indicating a more electron-rich environment due to halogen bonding. Conversely, the NMe_2 nitrogen experiences deshielding, likely due to the donor-to-acceptor charge transfer in the ground state, caused by halogen bonding in the acceptor part.

Table 4.5: Difference between the ^{15}N NMR chemical shift in C_6F_5I solvent and C_6F_6 solvent for the *heterocyclic* and *dimethylamino* nitrogen. Results from calculations in parentheses.

Compound	$\Delta\delta$ heterocyclic N	$\Delta\delta$ NMe_2
	ppm	ppm
B-2	-4.8 (-19.4)	2.9 (2.8)
B-3	-4.7 (-26.7)	2.3 (2.8)
B-4	-3.7 (-16.0)	3.6 (2.7)
DMAP	-15.4 (-22.8)	5.9 (7.6)

These patterns suggest that the nitrogen atom in the *heterocyclic* ring might be involved in XB interactions. These interactions could potentially enhance charge transfer within the dye molecule [153]. To confirm this hypothesis, my coworkers used 4-dimethylaminopyridine (**DMAP**) as a reference compound. **DMAP** exhibits similar interactions with C_6F_5I as the **B**-series dyes, displaying a notable shielding effect for the *heterocyclic* nitrogen and a deshielding effect in the NMe_2 nitrogen. However, **DMAP** shows larger complexation-induced shifts compared to the **B**-series dyes, indicating stronger halogen bonding. This finding supports the notion of lower association constants observed in series **B** due to the influence of the nearby boron site on the electronic properties of the key nitrogen atom. To investigate the factors influencing the NMR shifts, I further employed quantum chemical calculations. These calculations suggested that solvent polarity has minimal impact on the observed shifts (Table S6.3). This highlights the dominant roles played by halogen bonding and π-stacking interactions in shaping the NMR chemical shifts. Additionally, I calculated the changes in the ^{15}N-NMR chemical shifts upon complexation. The results are depicted in parentheses in Table 4.5 and exhibit a notable agreement with the experimental measurements. In particular, shielding effects for the *heterocyclic* nitrogen and deshielding effects for the nitrogen atom on the NMe_2 group are observed. This agreement between experimental and computational data further supports the hypothesis that halogen bonding can be formed at the *heterocyclic* nitrogen site.

The theoretical part of this study aims to provide a robust explanation for the experimental observations. I employed computational methods to rationalize the experimental findings, particularly the influence of halogen bonding on the electronic spectra of **B**-series dyes. These methods offer insights that might be difficult or impossible to obtain through

experiments alone. To understand the influence of halogen bonding on the dyes' photophysical properties, I first analyze the optimized geometries of the **B**:C_6F_5X complexes (Figure 4.15). **B-1**, lacking the *heterocyclic* nitrogen for halogen bonding, serves as a reference for the **B**-series dyes. Comparing **B-1** to the others will isolate the effect of halogen bonding in the nitrogen atom in the *heterocyclic* ring. I studied various **B**:C_6F_5X complexes classified into different groups by their intermolecular interactions to understand their structures and computationally reproduce the experimental data.

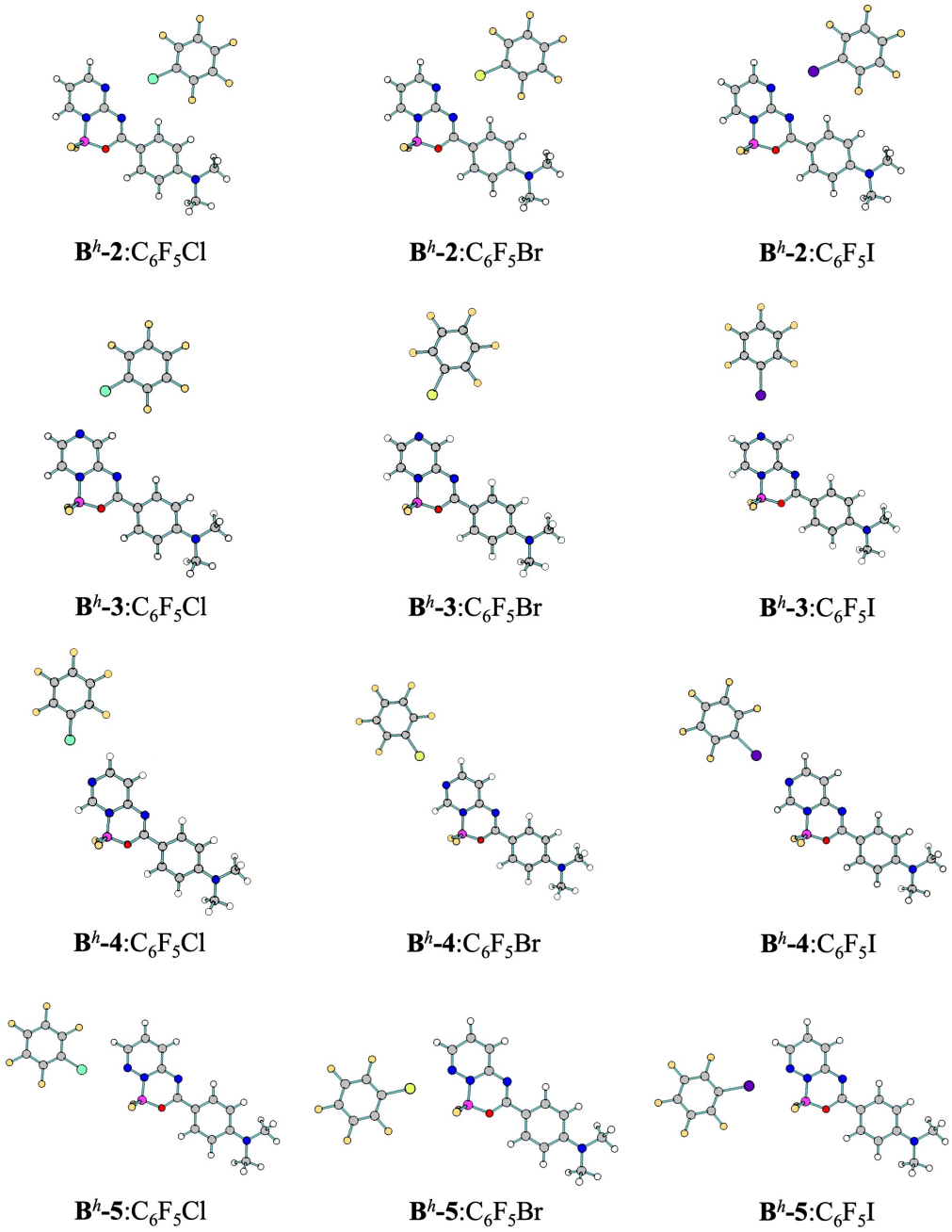

Figure 4.15: Equilibrium geometries of complexes formed by **B** and the halogen bond donors studied interacting through halogen bonding in the *heterocyclic* nitrogen, obtained at the MN15/aug-cc-pVDZ(PP) level of theory.

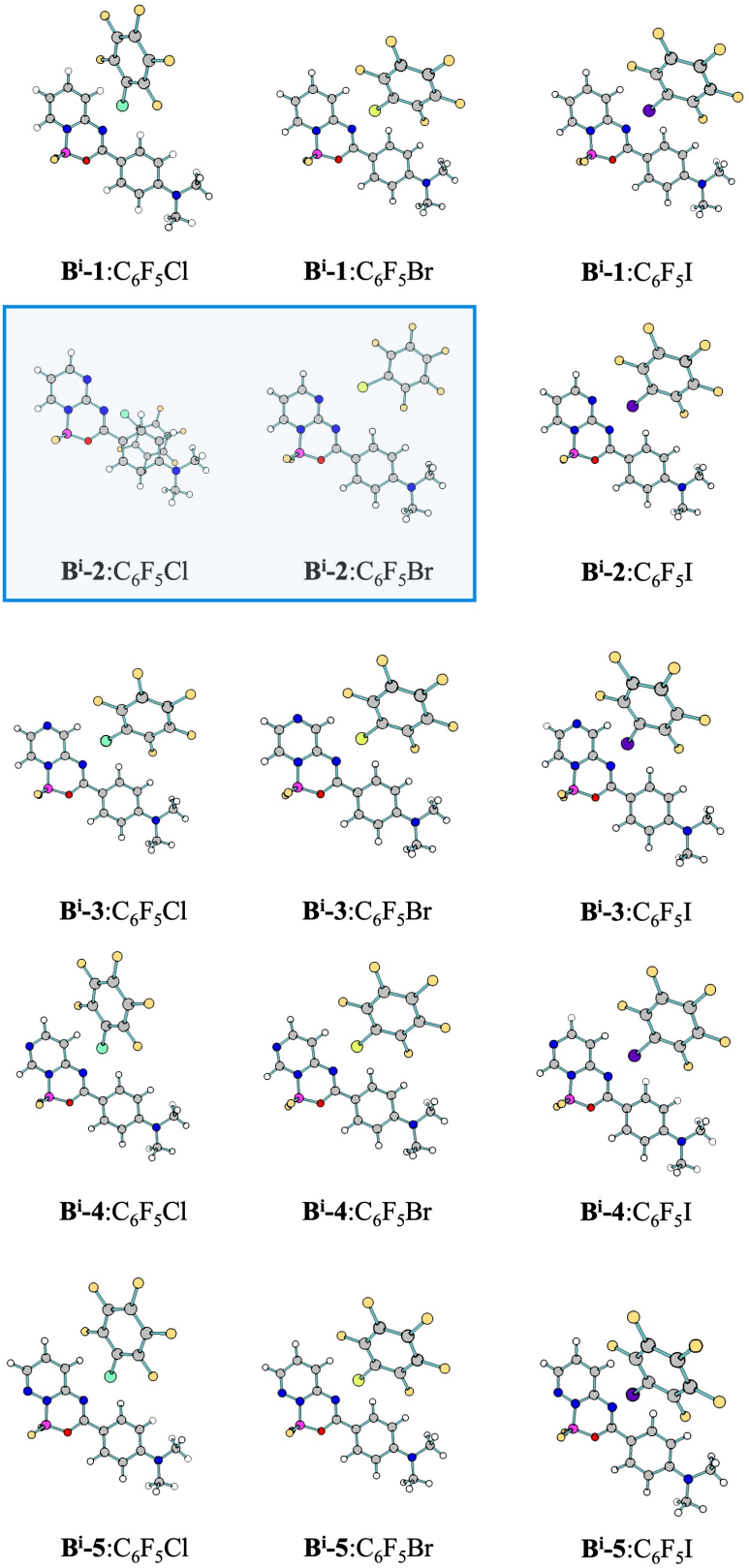

Figure 4.16: Equilibrium geometries of complexes formed by **B** and the halogen bond donors studied interacting through halogen bonding in the *imine* nitrogen, obtained at the MN15/aug-cc-pVDZ(PP) level of theory.

The first group comprises complexes formed through halogen bonding at the *heterocyclic* nitrogen, denoted by *h* ($\mathbf{B}^h$). Since **B-1** lacks this nitrogen, it cannot participate in this interaction and is excluded (Figure 4.15). The analysis reveals a key similarity between **B**-series dyes and those from series **A**: the C–X$\cdots$N angle is significantly affected depending on the halogen atom. Complexes formed between **B**-series dyes and C_6F_5Cl exhibit angles significantly deviated from linearity, suggesting a weaker halogen bond interaction. Conversely, complexes with C_6F_5I maintain near-linear angles (around 180°), indicative of stronger XB. Complexes with C_6F_5Br fall in between, agreeing with the trend of stronger XBs having more linear angles. An interesting exception arises in complexes involving **B-2**. Here, the proximity of the two nitrogen atoms appears to strengthen the interaction, leading to more linear angles even with C_6F_5Cl.

The second group consists of complexes formed via halogen bonding at the *imine* nitrogen and will be denoted by *i* ($\mathbf{B}^i$). The equilibrium geometries of the complexes within this group are illustrated in Figure 4.16. A notable distinction between these complexes and previous ones is that the halogen bond donor is positioned out-of-plane relative to the plane of the dye **B**, with the halogen atom oriented towards the *imine* nitrogen. These structural differences between the two interaction positions may have implications for the photophysical properties and overall performance of the dyes. The XB interaction at the *imine* nitrogen exhibits a unique and consistent geometry across all **B**-series dyes with various halogen bond donors. However, two exceptions (marked in blue) emerged during their geometry optimization: $\mathbf{B}^i$**-2**:C_6F_5Cl and $\mathbf{B}^i$**-2**:C_6F_5Br. Interestingly, $\mathbf{B}^i$**-2**:C_6F_5Cl adopts a geometry characteristic of π-stacking interactions, suggesting a different dominant interaction in this complex. In contrast, $\mathbf{B}^i$**-2**:C_6F_5Br adopts a geometry similar to $\mathbf{B}^h$**-2**:C_6F_5Br. This suggests a preference for in-plane XB at the heterocyclic nitrogen for **B-2** when interacting with the weaker halogen bond donor, C_6F_5Br.

The third group comprises complexes formed through π-stacking interactions. However, given the scope of this Thesis, the results on π-stacking geometries are not discussed here. Consequently, the focus of this study is the investigation of halogen bonding (XB) at the *heterocyclic* ($\mathbf{B}^h$) and *imine* ($\mathbf{B}^i$) nitrogen sites, which will be discussed in detail. All the equilibrium geometries of complexes belonging to the third group are depicted in Figure S6.4.

Using the equilibrium geometries depicted in Figures 4.15 and 4.16, I computed the interaction energies of XB complexes at the DF-SCS-MP2/aug-cc-pVDZ(PP) level of theory. The results of the calculations are depicted in Table 4.6. The interaction energies agree with well-known trends for halogen-bonded complexes. Complexes with C_6F_5I as the halogen bond donor consistently exhibit the strongest interaction energy for all **B**-series dyes, followed by C_6F_5Br and C_6F_5Cl.

It is worth noting that the interaction energies for complexes $\mathbf{B}^i$**-2**:C_6F_5Cl and $\mathbf{B}^i$**-2**:C_6F_5Br are absent. This is because the equilibrium geometries obtained during the

optimization process lead to complexes exhibiting π-stacking and XB interaction at the *heterocyclic* nitrogen, respectively, thereby preventing XB involving the *imine* nitrogen.

Table 4.6: Intermolecular interaction energies (ΔE, in kcal/mol) for halogen-bonded complexes between **B**-series dyes and C_6F_5X at the *heterocyclic* ($\mathbf{B}^h$) and *imine* ($\mathbf{B}^i$) nitrogen calculated using the DF-SCS-MP2 method and the aug-cc-pVDZ(PP) basis set.

dye	C_6F_5Cl	C_6F_5Br	C_6F_5I
$\mathbf{B}^h$**-2**	-3.43	-4.83	-6.40
$\mathbf{B}^h$**-3**	-1.97	-3.05	-4.64
$\mathbf{B}^h$**-4**	-1.98	-3.00	-4.43
$\mathbf{B}^h$**-5**	-2.53	-3.41	-4.72
$\mathbf{B}^i$**-1**	-3.03	-4.24	-5.73
$\mathbf{B}^i$**-2**	-	-	-5.72
$\mathbf{B}^i$**-3**	-2.79	-3.86	-5.09
$\mathbf{B}^i$**-4**	-2.88	-3.89	-5.17
$\mathbf{B}^i$**-5**	-3.11	-4.10	-5.40

Interestingly, the interaction energies of $\mathbf{B}^i$ complexes are generally consistent across different **B**-series dyes for the same halogen bond donor. For instance, for complexes with C_6F_5I as a halogen bond donor, the difference in interaction energy for the least stable complex ($\mathbf{B}^i$**-3**:C_6F_5I) and the most stable complex ($\mathbf{B}^i$**-1**:C_6F_5I) is lower than 0.7 kcal/mol. This agrees with expectations as the XB site remains constant in these complexes. In contrast, an exception is found in halogen-bonded complexes with the interaction at the *heterocyclic* nitrogen, where **B-2** complexes exhibit larger interaction energy compared to the other complexes. This can be attributed to the unique structural configuration of **B-2**, where the proximity of the two nitrogen atoms enhances the intermolecular interaction. When comparing the two XB positions (*heterocyclic* vs. *imine* nitrogen) for the same dye and halogen bond donor, $\mathbf{B}^i$:C_6F_5X complexes generally show slightly more stable interaction energies than their $\mathbf{B}^h$:C_6F_5X counterparts. However, these differences are relatively small, typically less than 1 kcal/mol.

To investigate the origin of these types of interactions, I used VP-EDS to perform the interaction energy decomposition for these complexes. Similar to series **A**, partitioning the interaction energy for **B**:C_6F_5X complexes at the MP2 level of theory is computationally expensive due to system size. Therefore, I focused on the HF contribution ($\Delta E_{int}^{\mathrm{HF}}$) to the interaction energy, further decomposing it into electrostatics ($\varepsilon_{el}^{(10)}$), exchange-repulsion ($\Delta E_{ex}^{\mathrm{HL}}$), and delocalization ($\Delta E_{del}^{\mathrm{HF}}$) terms. The remaining contributions have been included in the MP2 correlation term ($\Delta E_{corr}^{\mathrm{MP2}}$). I will not analyze the interaction energy decomposition for **B**-series dyes with C_6F_5Cl and C_6F_5Br because, as shown in Figure 4.7,

the decomposition is very similar for complexes that differ only in the halogen atom involved in the XB interaction. For **B**-series dyes with C_6F_5I, the interaction energy decomposition at the *heterocyclic* nitrogen shows consistent contributions from electrostatic, exchange-repulsion, and delocalization terms across all complexes (Figure 4.17a and Table S6.4).

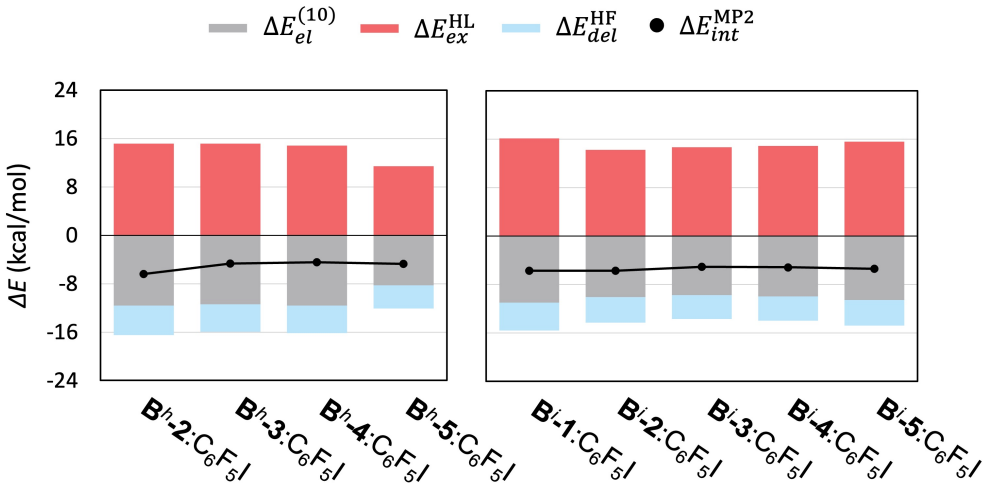

Figure 4.17: Partitioning of the HF interaction energy (ΔE_{int}^{HF}) of (a) $\mathbf{B}^h$:C_6F_5I, and (b) $\mathbf{B}^i$:C_6F_5I, complexes at the equilibrium geometries at the MP2/aug-cc-pVDZ-PP level of theory. The black dots combined with black lines indicate the total MP2 interaction energy computed with the DF-SCS-MP2 method.

Notably, $\mathbf{B}^h$**-5**:C_6F_5I exhibits slightly lower contributions, but the overall energy remains similar due to comparable relative weights within the components. These findings agree with the observations for series **A** (Figure 4.7), highlighting the consistent nature of the interaction energy in halogen bonding across systems. In this intermolecular interaction, exchange repulsion appears to be the dominant contribution, while the combined effect of electrostatics and delocalization provides additional stabilization to the complex. Furthermore, Figure 4.17b reinforces this consistency, demonstrating similar contribution patterns for all complexes studied in this work. This agrees with the broader trends observed throughout the thesis.

To understand how halogen bonding affects the dyes' photophysical properties, I compare the interatomic distances within the N$\cdots$X bridge across the **B**-series dyes in C_6F_5X solvents. The differences between the halogen bond lengths in the excited state (S_1) and the halogen bond lengths in the ground state (S_0) of each complex are illustrated in Figure 4.18. Interestingly, the N$\cdots$X bridge distances consistently decrease upon excitation compared to the ground state for all complexes. This trend suggests a strengthening of the halogen bond in the excited state. $\mathbf{B}^h$**-4** exhibits the smallest shortening of the bond length across C_6F_5X solvents, except for C_6F_5Cl where it shortens similarly to $\mathbf{B}^h$**-2** and $\mathbf{B}^h$**-5**. Furthermore, the shortening is more pronounced for complexes with C_6F_5I as the halo-

gen bond donor compared to other perfluorohaloarenes. Unlike series **A**, the changes in interatomic distances upon excitation in C_6F_5Cl and C_6F_5Br are not consistent across all **B**-series dyes. This agrees with the combined experimental and computational observations of weaker intermolecular interactions in series **B**.

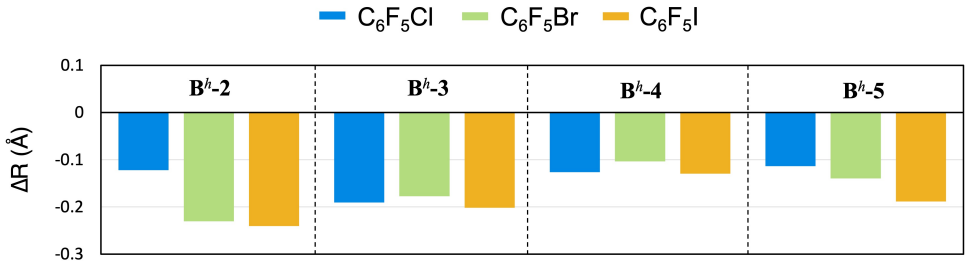

Figure 4.18: Differences in the length between the N$\cdots$X bond distance in the excited state equilibrium geometry and the N$\cdots$X bond distance in the ground state equilibrium geometries of the set of **B**:C_6F_5X complexes studied.

To connect the structural and energetic findings to experimental observations, Table 4.7 summarizes the calculated absorption and emission spectra for **B**^{h}**-2**, **B**^{h}**-3**, **B**^{h}**-4**, and **B**^{h}**-5** interacting with C_6F_5X via halogen bonding. While I initially explored the impact of solvent polarity (C_6F_6 and C_6F_5I) on emission spectra using the PCM model, gas-phase calculations yielded better agreement with experimental results. Therefore, the data presented here corresponds to gas-phase calculations. Figure 4.19 explores the impact of halogen bonding formation and solvation effects on emission spectra, as simulated by the PCM approach. Three distinct emission shifts are displayed alongside the corresponding experimental values. The blue line represents the emission wavelength shift for **B**-series dyes in C_6F_5I solvent (PCM) compared to C_6F_6 solvent (PCM). The green line shows the emission wavelength shift for **B**^{h}:C_6F_5I complexes (gas phase) compared to the corresponding isolated **B**^{h} dyes (gas phase). This shift reflects the influence of XB formation at the *heterocyclic* nitrogen. The orange line displays the emission wavelength shift for **B**^{i}:C_6F_5I complexes (gas phase) compared to the corresponding isolated **B**^{i} dyes (gas phase). This shift isolates the effect of XB at the *imine* nitrogen. My analysis using the PCM solvation model indicates minimal influence of solvent polarity on the emission spectra of **B**-series dyes. This agrees with the approach used for **A**-series dyes, where gas-phase TD-DFT calculations accurately reproduce experimental emission maxima for **B**^{h}:C_6F_5I complexes. This consistency suggests that gas-phase calculations are a reliable method to rationalize the photophysical properties of these XB complexes and suggest that this type of dye in C_6F_6 behaves as in the gas state. The calculated absorption maxima agree with experimental data, exhibiting a small redshift upon changing the XB donor from Cl to Br to I (C_6F_5X). Notably, the variations observed for **B**-series dyes interacting with C_6F_5I are within a narrow range of 10 nm. This consistency between theory and experiment highlights the minimal influence of the halogen bond donor on the dyes' absorption properties.

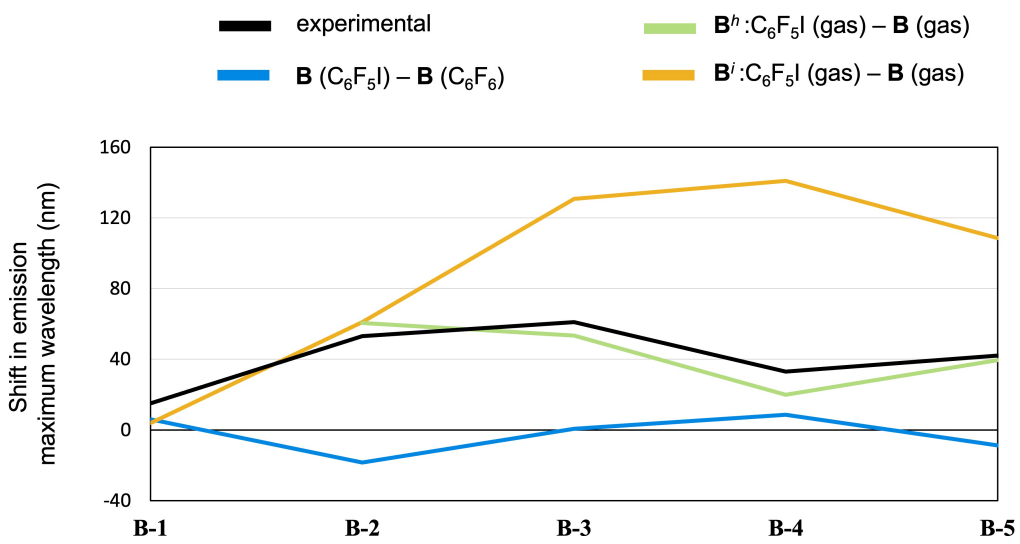

Figure 4.19: Effect of the solvent in the shift in emission maximum wavelength of the isolated dye using PCM solvation model (blue), shift in emission maximum wavelength upon complex formation in the *heterocyclic* nitrogen in the gas phase (green), shift in emission maximum wavelength upon complex formation in the *imine* nitrogen in the gas phase (orange), and comparison with the experimental shifts in emission maximum wavelength of **B**-dyes series in C_6F_5I with respect to C_6F_6 (black).

On the other hand, the maximum emission wavelength red-shifts upon halogen bond formation, with the magnitude of the shift correlating to the halogen bond strength (Cl < Br < I) for each **B**-series dye. C_6F_5I, the strongest XB donor, induces the largest red shift for all complexes. Interestingly, $\mathbf{B}^h$**-4** displays the smallest shift (23 nm), while $\mathbf{B}^h$**-2** and $\mathbf{B}^h$**-3** exhibit the largest shifts (59 nm and 60 nm, respectively). The oscillator strength suggests that $\mathbf{B}^h$**-4** may be the strongest emitter, followed by $\mathbf{B}^h$**-3** and $\mathbf{B}^h$**-5**, with $\mathbf{B}^h$**-2** likely being the weakest. Furthermore, it decreases along with the interaction energy of the halogen bond. Overall, these findings highlight the significant influence of halogen bonding on the dyes' emission properties. The strength of the halogen bond dictates the extent of the red shift and emission intensity.

To understand the observations in the electronic spectra of **B**-series dyes, I computed the difference in electron density between the excited and ground states of $\mathbf{B}^h$**-3**:C_6F_5I at both the ground-state (absorption) and excited-state (emission) geometries. These differences are visualized in Figure 4.20 and help to explain the spectral behavior of the complex. The electron density difference during the absorption process (Figure 4.20a) reveals minimal change near the halogen bond, suggesting a weak influence on light absorption. Conversely, a significant density change is observed across the N$\cdots$I bond during emission. This highlights a stronger influence of the halogen bond on the emission spectrum, agreeing with observations in series **A**. These findings imply that the electronic structure of the complex is more sensitive to the halogen bond during emission, leading to a more pronounced effect on the emission maximum wavelength.

Table 4.7: Summary of the electronic structure calculations of **B** dyes and their complexes formed with C_6F_5X halogen bond donors interacting at the *heterocyclic* nitrogen using TD-DFT at MN15/aug-cc-pVDZ level of theory. Maximum absorption wavelength (λ_{abs}), maximum emission wavelength (λ_{em}), oscillator strengths (f), and Stokes shift.

Compound	Halogen bond donor	λ_{abs} nm	f	λ_{em} nm	f	Stokes shift cm-1
B-1	not present	348	0.91	368	0.82	1579
B^h-2	not present	349	0.83	452	0.08	6523
	C_6F_5Cl	354	0.75	468	0.06	6909
	C_6F_5Br	357	0.72	489	0.05	7535
	C_6F_5I	361	0.68	513	0.04	8159
B^h-3	not present	368	0.77	438	0.31	4376
	C_6F_5Cl	370	0.74	447	0.29	4633
	C_6F_5Br	377	0.75	468	0.26	5202
	C_6F_5I	382	0.76	492	0.24	5834
B^h-4	not present	351	0.95	368	0.84	1367
	C_6F_5Cl	352	1.05	371	0.93	1448
	C_6F_5Br	357	1.11	379	0.92	1668
	C_6F_5I	361	1.17	388	0.90	1988
B^h-5	not present	356	0.64	453	0.13	6029
	C_6F_5Cl	357	0.71	463	0.13	6395
	C_6F_5Br	364	0.67	478	0.12	6581
	C_6F_5I	367	0.67	493	0.12	6927

While TD-DFT calculations generally agree with experimental data, a discrepancy arises in the emission spectra of **B**^{h} complexes with C_6F_5Cl and C_6F_5Br. Experimentally, these complexes exhibit minimal or even blue-shifted emission maxima when compared to C_6F_6 solvent. In contrast, the calculations predict larger redshifts following the halogen bond strength trend.

To investigate this discrepancy between experimental and computational data further, I calculated the Gibbs free energy (ΔG) for the formation of all complexes, incorporating a correction term for simulating the experimental concentrations. The analysis of the calculated Gibbs free energy shown in Table 4.8 reveals that only complexes formed with C_6F_5I, both in *heterocyclic* and *imine* positions, exhibit negative ΔG values, indicating thermodynamically favorable halogen bonding under the specific experimental conditions. This suggests strong stabilization by iodine for both interaction sites on the dyes.

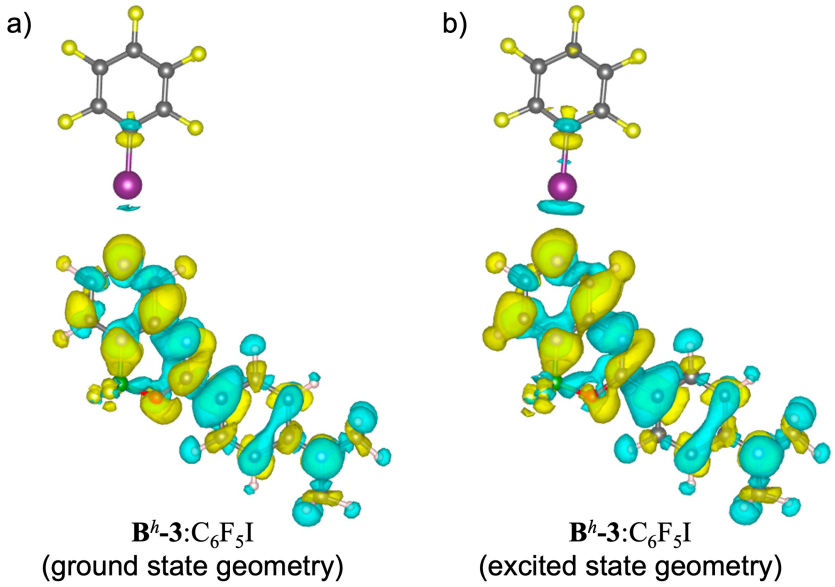

Figure 4.20: Electron density difference between the electronic excited and ground states at (a) the equilibrium ground state geometry (absorption) and (b) equilibrium excited state geometry (emission) for the **B**^{h}**-3**:C_6F_5I complex. In blue the regions with decreased electron density, and in yellow the regions with increased electron density.

In contrast, complexes with C_6F_5Cl and C_6F_5Br show positive ΔG values, implying these interactions are not energetically favorable. This highlights the crucial role of C_6F_5I in promoting stable complex formation compared to weaker halogen bond donors, including C_6F_5Cl and C_6F_5Br. Furthermore, ΔG values for series **B** are generally less negative compared to series **A**, suggesting lower thermodynamic stability. This agrees with experimental observations of smaller emission shifts for **B**:C_6F_5I complexes compared to **A**:C_6F_5I and low association constants from NMR titrations.

Table 4.8: Corrected formation Gibbs energy (ΔG, in kcal/mol) taking into account the concentration of the reactants and product used in the measurements for **B**^{h}:C_6F_5X and **B**^{i}:C_6F_5X complexes.

dye	C_6F_5Cl	C_6F_5Br	C_6F_5I
B^h**-2**	2.69	0.30	-1.37
B^h**-3**	4.85	1.77	-0.22
B^h**-4**	3.16	1.86	-0.13
B^h**-5**	2.60	1.36	-0.54
B^i**-1**	1.68	1.88	-1.06
B^i**-2**	-	-	-1.48
B^i**-3**	2.30	0.40	-0.81
B^i**-4**	1.56	0.13	-0.91
B^i**-5**	2.16	-0.05	-1.08

While several insights have been gained into the differing effects of halogen bonding on absorption and emission processes, the reasons for the variations observed between different dyes of the series **B** remain unexplained. To elucidate these changes, I computed the differences in electronic density between the excited and ground states at the excited-state geometries of $\mathbf{B}^h$**-2**:C_6F_5I, $\mathbf{B}^h$**-3**:C_6F_5I, $\mathbf{B}^h$**-4**:C_6F_5I, and $\mathbf{B}^h$**-5**:C_6F_5I, simulating the change of the electronic density in the emission process. These differences are depicted in Figure 4.21.

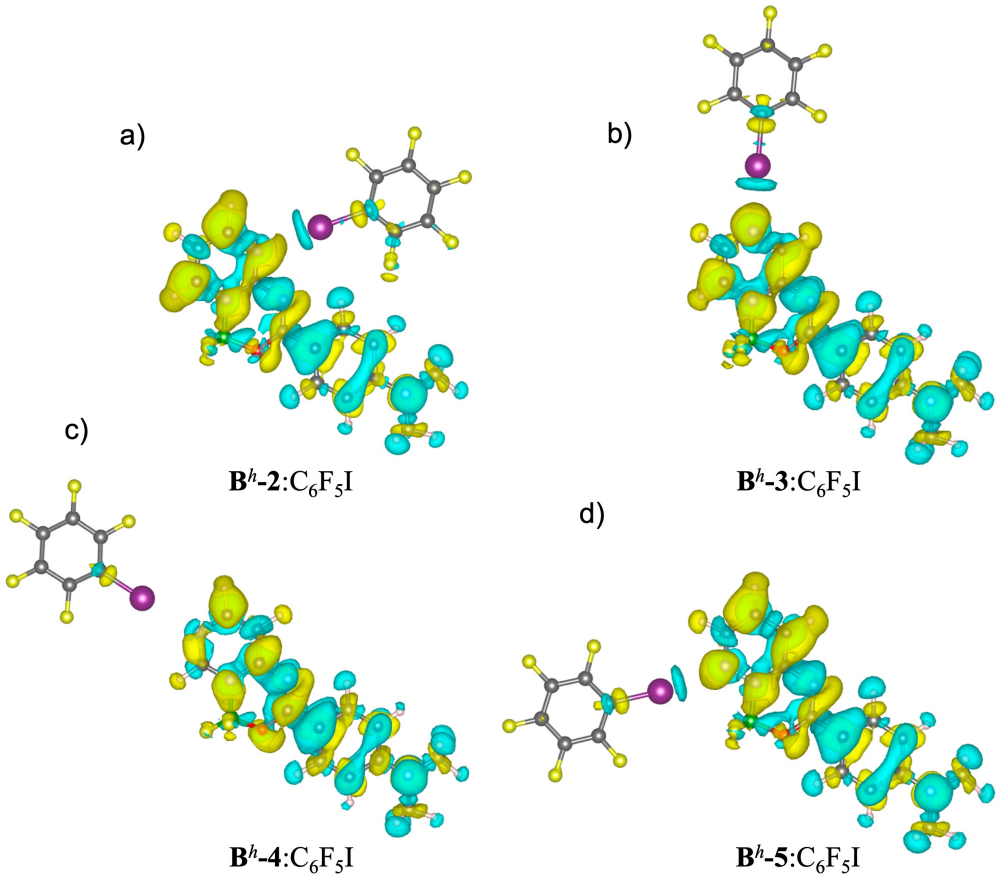

Figure 4.21: Electron density difference between the excited and ground states of the emission process for the a) $\mathbf{B}^h$**-2**:C_6F_5I, b) $\mathbf{B}^h$**-3**:C_6F_5I, c) $\mathbf{B}^h$**-4**:C_6F_5I, and d) $\mathbf{B}^h$**-5**:C_6F_5I complexes. In blue the regions with decreased electron density, and in yellow the regions with increased electron density.

The minimal change in electron density near the N$\cdots$I bond in $\mathbf{B}^h$**-4**:C_6F_5I (Figure 4.21c) explains the small shift in its emission maximum wavelength upon changing the solvent from C_6F_6 to C_6F_5I. This suggests a weaker dependence of $\mathbf{B}^h$**-4**'s emission on halogen bonding compared to other **B**-series dyes. This observation agrees with the calculated Gibbs free energy values (Table 4.8). $\mathbf{B}^h$**-4**:C_6F_5I complex has the least negative ΔG, indicating a weaker thermodynamic driving force for complex formation compared to other **B**-series dyes with C_6F_5I.

Conversely, the substantial changes in electron density near the N$\cdots$I bond for $\mathbf{B}^h$-**2**:C_6F_5I and $\mathbf{B}^h$-**3**:C_6F_5I (Figure 4.21) correlate well with the larger emission maximum wavelength shifts observed in these complexes upon solvent change. These results suggest a stronger dependence of the **B-2** and **B-3** emissions on halogen bonding effects. $\mathbf{B}^h$-**5**:C_6F_5I also exhibits a significant density change, but less pronounced compared to $\mathbf{B}^h$-**2** and $\mathbf{B}^h$-**3**. This agrees with the moderate emission shift observed for $\mathbf{B}^h$-**5**, falling between the larger shifts of $\mathbf{B}^h$-**2** and $\mathbf{B}^h$-**3** and the minimal shift of $\mathbf{B}^h$-**4**. Overall, the combined analysis of TD-DFT calculations, thermodynamics, and excited-state electron density changes underscores the critical role of halogen bonding in dictating the photophysical properties of **B**-series dyes.

Remarkably, an unexplained outcome from the analysis performed of ΔG values (Table 4.8) and electronic structure calculations (Table 4.7) has been observed. While the ΔG suggests that the *imine* nitrogen position might be favorable for halogen bonding and complex stability, only the calculations for complexes with halogen bonding at the *heterocyclic* nitrogen position agree with experimental observations (Figure 4.19). Therefore, it is necessary to analyze the results for $\mathbf{B}^i$:C_6F_5I to understand why they do not predict the experimental observations. The summary of electronic structure calculations of $\mathbf{B}^i$:C_6F_5I complexes are depicted in Table 4.9.

Table 4.9: Summary of electronic structure calculations of $\mathbf{B}^i$-**1**, $\mathbf{B}^i$-**2**, $\mathbf{B}^i$-**3**, $\mathbf{B}^i$-**4**, and $\mathbf{B}^i$-**5** complexes formed with C_6F_5I halogen bond donor at TD-DFT level. Maximum absorption wavelength (λ_{abs}), maximum emission wavelength (λ_{em}), oscillator strengths (f), and Stokes shift.

Compound	λ_{abs} nm	f	λ_{em} nm	f	Stokes shift cm-1
$\mathbf{B}^i$-**1**:C_6F_5I	351	0.80	372	0.73	1608
$\mathbf{B}^i$-**2**:C_6F_5I	355	0.73	513	0.03	8676
$\mathbf{B}^i$-**3**:C_6F_5I	371	0.69	569	0.00	9379
$\mathbf{B}^i$-**4**:C_6F_5I	356	0.82	509	0.00	8444
$\mathbf{B}^i$-**5**:C_6F_5I	360	0.59	562	0.00	9984

The calculated Stokes shifts for $\mathbf{B}^i$:C_6F_5I complexes deviate significantly from both experimental data and the values obtained for $\mathbf{B}^h$-series complexes (Table 4.7). Interestingly, two exceptions are found within this group. $\mathbf{B}^i$-**1**:C_6F_5I exhibits a very low Stokes shift, suggesting minimal intramolecular charge transfer within the complex. In contrast, $\mathbf{B}^i$-**2**:C_6F_5I displays a Stokes shift similar to its $\mathbf{B}^h$ counterpart.

The differences in Stokes shifts between $\mathbf{B}^i$:C_6F_5I and their corresponding $\mathbf{B}^h$:C_6F_5I (with these two exceptions) are intriguing, especially considering that the only difference is found in the halogen bonding sites (*imine* vs. *heterocyclic* nitrogen).

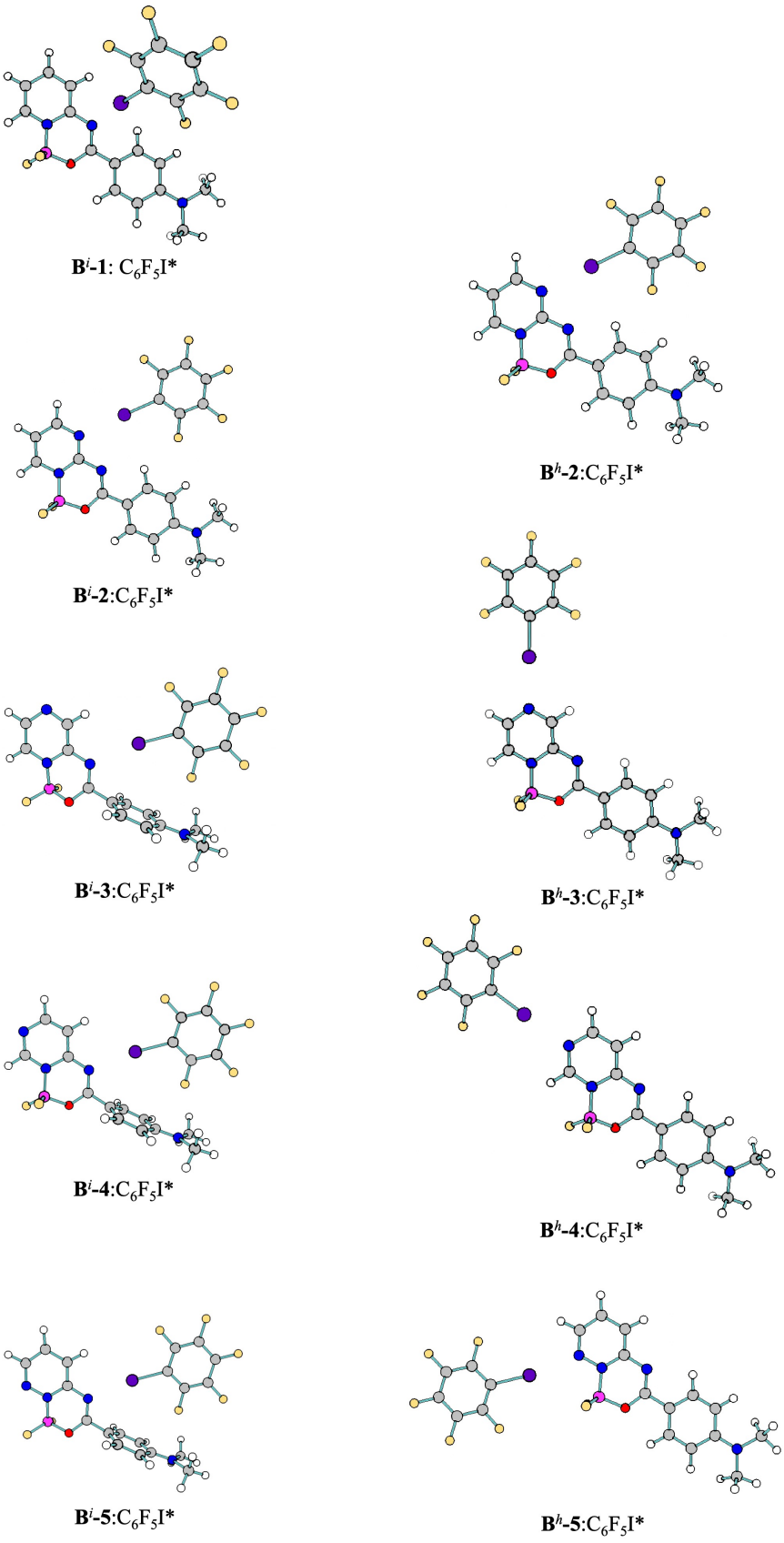

Figure 4.22: Equilibrium excited state geometries of complexes formed by **B** and C_6F_5I interacting through halogen bonding in the *heterocyclic* and *imine* nitrogen.

To understand this observation, further analysis of the excited-state geometries is necessary (Figure 4.22). The similarity between excited-state geometries of $\mathbf{B}^{i}$**-2**:C_6F_5I and $\mathbf{B}^{h}$**-2**:C_6F_5I suggest comparable effects from halogen bonding at the *imine* and *heterocyclic* nitrogen positions, explaining the similar Stokes shift. This makes it challenging to isolate the specific influence of halogen bonding in the *imine* nitrogen on **B-2**'s properties.

Furthermore, all $\mathbf{B}^{i}$-series complexes except $\mathbf{B}^{i}$**-1**:C_6F_5I and $\mathbf{B}^{i}$**-2**:C_6F_5I exhibit a significant twist in the excited state. This unique planarity of $\mathbf{B}^{i}$**-1**:C_6F_5I in the excited state indicates a distinct interaction compared to other complexes in the series, explaining the differences in the calculated emission maximum wavelength. In contrast, the significant twist observed in the excited state geometries of $\mathbf{B}^{i}$**-3**:C_6F_5I, $\mathbf{B}^{i}$**-4**:C_6F_5I, and $\mathbf{B}^{i}$**-5**:C_6F_5I leads to a predicted zero oscillator strength for their emission processes. This suggests negligible intensity and potentially undetectable emission bands in experiments for these complexes.

The consistency between computational chemistry and experimental measurements helps validate the theoretical approach and rationalize the experimental observations. However, it is important to consider that the non-competitive environment, where the solvent itself acts as the XB donor, allows the interactions at different positions on the dye to occur simultaneously. This complexity can influence the overall photophysical properties of the system and may contribute to discrepancies between the calculations and experimental data.

Future work could benefit from incorporating molecular dynamics simulations. These simulations can explore the specific interactions between the solvent and the dye at different bonding sites, providing a more comprehensive understanding of the dynamic behavior within the complexes. This would offer valuable insights into how the halogen bond donor position influences the dyes' properties. Ultimately, such knowledge can aid in refining models and enhancing the accuracy of theoretical predictions in future research efforts.

CHAPTER 5

Decomposition of the changes in the IR spectra induced by halogen bonding

The previously described research successfully elucidated and characterized the electronic structure of complexes formed by organic fluoroborates and halogenated perfluoroarenes through halogen bonding, expanding our understanding of such interactions. As highlighted in the Introduction chapter, infrared (IR) spectroscopy has been extensively used to confirm the formation and quantify the strength of halogen bonding. The measured infrared spectra (Figure 4.5) observed in the previous chapter revealed intriguing changes upon complex formation. These observations captured my attention to explore the physical origin of these spectral changes.

To gain further insight into the observed spectral changes in Figure 4.5, I performed calculations on the vibrational structure of pyridine, which is the halogen bond acceptor moiety of the **A**-series dyes, C_6F_5X molecules (X = Cl, Br, and I), and their complexes (**pyr**:C_6F_5X). Figure 5.1 illustrates the impact of these intermolecular interactions on IR spectra. The figure compares the calculated infrared spectra of a) pyridine, b) C_6F_5I, and c) the complex formed by the pyridine interacting with C_6F_5I through halogen bonding. Figure 5.1d depicts the difference between the IR spectrum of the complex and the IR spectra of their components, revealing significant changes in the infrared spectrum upon complex formation. These changes include frequency and intensity shifts for several bands. Consistent with the measured spectra (Figure 4.5), a new band attributed to the intermolecular vibration appears at a short wavenumber in the IR spectrum of the complex (Fig-

ure 5.1c). Another example of the effect of halogen bonding in the vibrational structure of the molecules forming the complex is the pair of bands around 1000 and 1100 cm^{-1} in Figure 5.1d. For the first of the bands, a combined shift in intensity and frequency can be observed, while for the higher-frequency band, an increase in intensity is noticed. Furthermore, the band corresponding to the C–I stretching at 200 cm^{-1} exhibits a notable intensity change upon complex formation (Figure 5.1c). These spectral variations are characteristic of vibrational modes affected by intermolecular interactions and highlight their impact on the observed features.

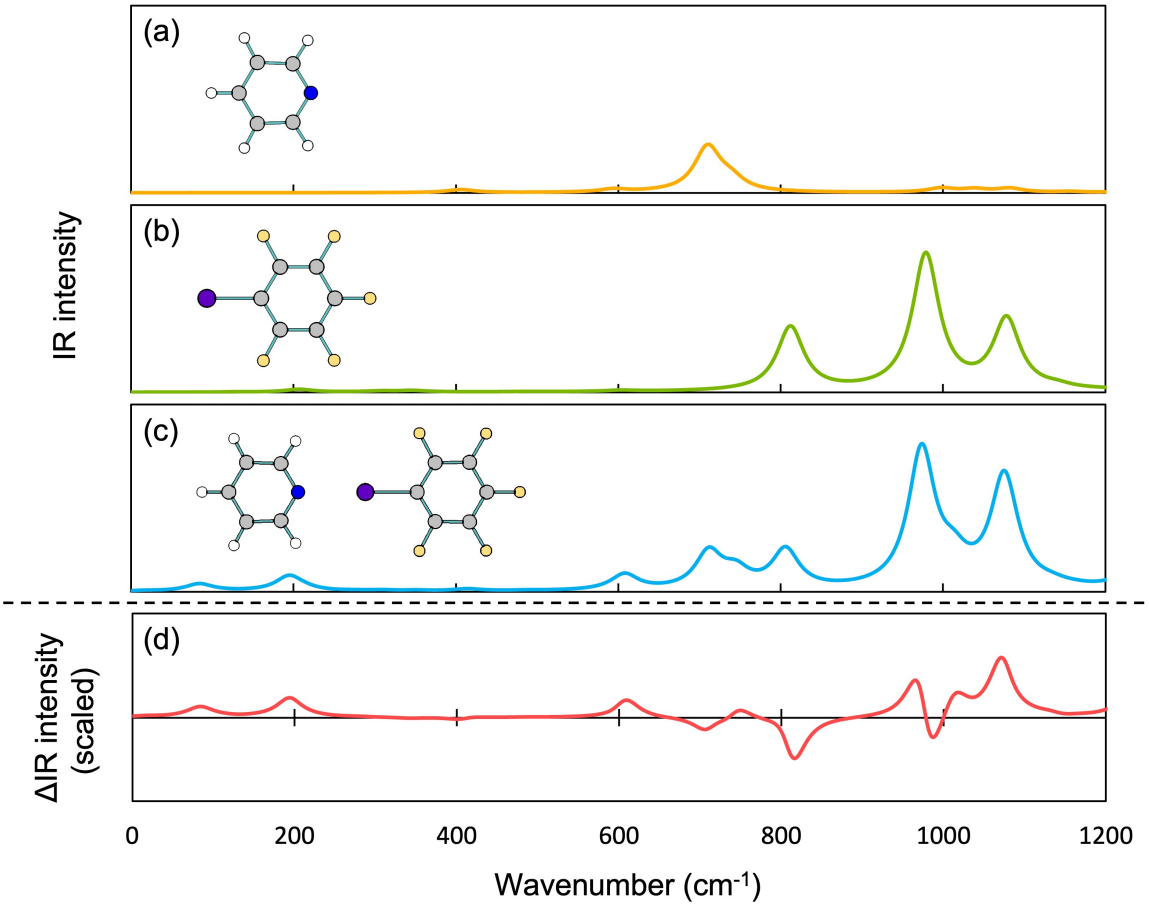

Figure 5.1: Normalized simulated IR spectra of (a) pyridine, (b) C_6F_5I, and (c) **pyr**:C_6F_5I, and (d) their difference with the intensity scaled 5 times.

Some studies complement infrared spectroscopy measurements by energy decomposition analyses. EDA provides an indirect link between spectroscopic features and the underlying interaction types. However, it is important to acknowledge that interaction energies (related to complex stability) and electric properties (influencing spectral intensities) may exhibit distinct patterns of interaction types. This point has been highlighted in seminal works by Fowler and Sadlej [124], Bishop and Dupuis [125], and Heijmen, Moszyński

et al. [154], along with subsequent research [126, 155, 156]. These differences complicate the analysis of the physical origin of the spectral changes influenced by intermolecular interactions.

To address this limitation, this chapter introduces the theoretical framework for the novel computational tool developed by me and my coworkers: Infrared Spectra Decomposition Analysis (IRS-DA). Unlike traditional energy decomposition analysis (EDA) focused on complex stability, IRS-DA enables *direct* correlation of spectral changes with specific intermolecular interaction types (electrostatics, exchange, induction, dispersion). This allows for a more direct understanding of how these interactions affect the observed spectral features. The interpretative power of IRS-DA is subsequently demonstrated through its application to specific halogen-bonded systems. This novel method builds upon my group associates' previous work on the physical origin of nuclear relaxation contributions to the polarizability (α^{nr}) of molecular complexes [129, 149, 157]. A fundamental understanding of α^{nr} is essential for the derivation of the IRS-DA method. The polarizability describes a molecule's susceptibility to polarization in the presence of an external electric field. The total polarizability (α^{tot}) comprises two main components: electronic (α^{el}) and nuclear relaxation (α^{nr}) contributions [158, 159]:

$$\alpha^{tot} \approx \alpha^{el} + \alpha^{nr} \tag{5.1}$$

The α^{el} describes the pure electronic response of the molecule's electron cloud to an external electric field at its equilibrium geometry. In contrast, α^{nr} arises from the change in the electronic energy caused by the field-induced distortion of the molecules's equilibrium geometry. While calculating α^{el} is computationally feasible for small and medium-sized molecules using accurate ab initio methods, obtaining α^{nr} is more demanding. It requires either field-dependent optimizations maintaining the Eckart conditions [160, 161] or the calculation of the Hessian and first derivatives of the dipole moment with respect to the nuclear coordinates [158]. Both approaches are computationally expensive. Consequently, it is common to compute only the electronic contribution to polarizability. However, recent studies have emphasized the importance of the nuclear relaxation contribution to the polarizability in understanding the total polarizability of molecular complexes [130, 149, 157, 162]. The electronic polarizability, can be calculated from Equation 2.17, using the Hellman-Feynman theorem:

$$\alpha^{el} = -\frac{\partial^2 E^{el(0)}(\mathbf{F})}{\partial \mathbf{F^2}} \tag{5.2}$$

While this derivative can be efficiently calculated using the standard Finite Field (FF) method (Equation 2.18), obtaining the nuclear relaxation term requires a different approach. Unlike the standard FF method where nuclei are fixed, α^{nr} calculations involve allowing the geometry to relax in response to the applied electric field. This relaxation,

which should be evaluated while maintaining the Eckart conditions, leads to a new equilibrium geometry that incorporates the field's influence. The polarizability obtained in this scenario reflects the combined effect of electronic response and nuclear relaxation. Unlike in Eq 2.18, to compute this property the electronic energy of a chemical system at a field-dependent relaxed equilibrium geometry under a static and uniform electric field is defined, denoted with the superscript *r*, as a Taylor expansion series on the electric field intensity:

$$E^{el(r)}(\mathbf{F}) = E^{el(r)}(\mathbf{0}) + \left(\frac{\partial E^{el(r)}(\mathbf{F})}{\partial \mathbf{F}}\right)\mathbf{F} + \frac{1}{2!}\left(\frac{\partial^2 E^{el(r)}(\mathbf{F})}{\partial \mathbf{F^2}}\right)\mathbf{F}\mathbf{F}... \tag{5.3}$$

where the total polarizability can be written as:

$$\alpha^{tot} = -\frac{\partial^2 E^{el(r)}(\mathbf{F})}{\partial \mathbf{F^2}} \tag{5.4}$$

The procedure to obtain α^{tot} requires the determination of optimized field-dependent geometries in the subspace of the vibrational 3N-6(5) coordinates. Therefore, the rotations and translations of the molecular geometry should be avoided during the field-dependent optimizations, which could be achieved with the proper application of Eckart conditions [158, 163, 164]:

$$\sum_i m_i(\mathbf{a}_i \times \mathbf{r}_i) = 0 \tag{5.5}$$

where $\mathbf{r}_i$ is the vector from the center of mass of the system to atom *i* in the field-dependent equilibrium geometry, $\mathbf{a}_i$ is the field-free equilibrium value of that vector, and m_i is the atomic mass. Then, the field-dependent geometry optimization may be carried out by the following procedure:

1. Using any standard quantum chemistry program a complete optimization of the field-free geometry is performed.

2. At this geometry, three rotations (two for linear molecules) and three translational Eckart coordinates are constructed.

3. A set of variable coordinates is read as input. These coordinates may be of any type (internal, normal, etc.) and any number from one to 3N-6(5).

4. The input coordinates expressed in terms of mass-weighted Cartesian displacements are orthogonalized to the field-free translations and rotations.

5. A field-dependent geometry optimization is performed in this subspace of orthogonalized coordinates. This step can be performed using the Broyden, Fletcher, Goldfarb, and Shanno (BFGS) method [165–168].

Following the field-dependent geometry optimization for the nuclei, the FF method is employed again. This time, its use will provide the combined electronic and nuclear relaxation contributions to the polarizability. Subtracting the previously obtained electronic contribution from this value yields the isolated nuclear relaxation contribution. Furthermore, when orthogonalizing the coordinates of the system, the methodology allows the isolation of the nuclear relaxation contribution to the polarizability for a specific vibrational mode a. Then, α_a^{nr} is obtained by performing the field-dependent geometry optimization within the subspace defined solely by the vibrational mode of interest.

Having established the method for calculating the nuclear relaxation contribution for a specific vibrational mode, I now delve into the development of the IRS-DA method itself. The analytical expression of the average nuclear relaxation contribution for a given vibrational mode *a* is given by:

$$\alpha_a^{nr} = \frac{1}{3\omega_a^2}\left[\left(\frac{\partial\mu_x}{\partial Q_a}\right)^2 + \left(\frac{\partial\mu_y}{\partial Q_a}\right)^2 + \left(\frac{\partial\mu_z}{\partial Q_a}\right)^2\right] \tag{5.6}$$

where ω_a is the vibrational harmonic frequency of the mode a, μ_x, μ_y and μ_z are the Cartesian components of the molecular electric dipole moment, and Q_a denotes the normal mode coordinate a. The IR intensity for vibrational mode *a* can be expressed as:

$$I_a = \frac{N\pi}{3c^2}\left[\left(\frac{\partial\mu_x}{\partial Q_a}\right)^2 + \left(\frac{\partial\mu_y}{\partial Q_a}\right)^2 + \left(\frac{\partial\mu_z}{\partial Q_a}\right)^2\right] \tag{5.7}$$

where N corresponds to Avogadro's number, and c denotes the speed of light. Interestingly, both properties depend on the square of the first derivative of the dipole moment μ with respect to the normal mode Q_a. By combining these equations, it is obtained:

$$\alpha_a^{nr} = \frac{c^2}{N\pi} \times \frac{I_a}{\omega_a^2} \tag{5.8}$$

Equation 5.8 relates the nuclear-relaxation polarizability for a specific vibrational mode to the ratio between the IR intensity and the square of the frequency of that vibrational mode. Based on the previous demonstration, α_a^{nr} can be computed as a second derivative of the field-dependent electronic energy, i.e. Equation 5.4. My coworkers and I have previously shown the use VP-EDS method to decompose this property [129], although any decomposition scheme (ETS-NOCV, ALMO-EDA, etc.) can be used. Thus, Equation 5.8 allows for the partitioning of the ratio between the IR intensity and the square of the frequency of any vibrational mode. However, this Thesis is devoted to the study of halogen bonding and its influence on the spectroscopic properties of dyes. Consequently, similar to the interaction energy, the excess (interaction-induced) property (ΔP) of the molecular complexes, i.e. the change of a property due to the intermolecular interactions, can be described as:

$$\Delta P = P_{AB} - [P_A + P_B] \tag{5.9}$$

where *AB* refers to the complex formed by the subsystems *A* and *B*. Combining Equation 5.8 and Equation 5.9 leads to the following expression for the *excess* nuclear relaxation polarizability for a given vibrational mode *a*:

$$\Delta\alpha_a^{nr} = \frac{c^2}{N\pi} \times \Delta\left(\frac{I_a}{\omega_a^2}\right) \tag{5.10}$$

The corresponding expression for each interaction type, *i*, when an EDA is applied to the nuclear relaxation polarizability is given by:

$$\Delta\alpha_a^{nr,i} = \frac{c^2}{N\pi} \times \Delta\left(\frac{I_a^i}{\omega_a^{2,i}}\right) \tag{5.11}$$

Equation 5.11 enables interpreting the simultaneous change in the IR intensity and the vibrational frequency upon the formation of a complex in terms of the interaction types, using the procedure previously developed to decompose the *excess* nuclear relaxation polarizability. Consequently, this approach allows the quantitative analysis of the physical terms' contribution to the ratio between IR intensity and the square of the frequency induced upon the formation of a molecular complex *AB*.

$$\Delta\left(\frac{I_a^i}{\omega_a^{2,i}}\right) = \frac{I_a^i}{\omega_a^{2,i}}(AB) - \frac{I_a^i}{\omega_a^{2,i}}(A) - \frac{I_a^i}{\omega_a^{2,i}}(B) \tag{5.12}$$

Commonly, for the molecular modes, only one of the subsystems of the complex, i.e., *A* or *B* is responsible for the studied vibrational mode *a*. Thus, only one subtraction to the IR band of the complex is needed. On the other hand, for the purely intermolecular modes, neither *A* nor *B* is responsible for the studied vibrational mode *a*, and therefore no subtraction to the IR band of the complex is needed. Furthermore, two possible limiting cases arise when applying Equation 5.12: (a) constant transition intensity or (b) constant transition frequency. The former is not practically useful as the relation $\Delta\omega_a^i \sim \sqrt{1/\Delta\alpha_a^{nr,i}}$ does not permit the direct decomposition of frequency changes using the decomposition of $\Delta\alpha_a^{nr}$. However, if the frequency change for a particular vibrational mode upon complex formation is negligible, then the decomposition of ΔI_a from the corresponding decomposition of the α_a^{nr} can be directly obtained:

$$\Delta I_a^i = \frac{N\pi\omega_a^2}{c^2} \times \Delta\alpha_a^{nr,i} \tag{5.13}$$

This equation facilitates the direct decomposition of the changes in IR intensity for a specific vibrational mode during complex formation into various interaction types, enabling a physical understanding of the variations in IR spectra caused by intermolecular interactions.

The protocol I used in this chapter for applying the developed method for decomposing the changes in the IR spectrum of molecular complexes into physical terms to real cases, such as **pyr**:C_6F_5X complexes, is schematically illustrated in Figure 5.2.

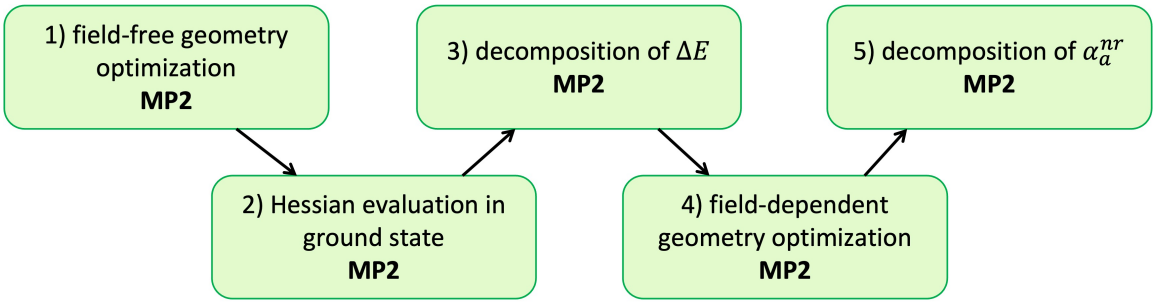

Figure 5.2: Protocol applied for the decomposition of the changes in the IR intensity induced by halogen bonding into physical terms.

The first step of the protocol involved the field-free equilibrium geometries optimization of the studied complexes applying tight convergence criteria (10^{-11} Hartree and 10^{-9} Hartree Bohr^{-1} for energy and gradients, respectively) employing the MP2 method [169] in combination with the aug-cc-pVDZ basis set [142, 143]. For the heavy atoms (bromine and iodine), the corresponding effective core potential (aug-cc-pVDZ-PP) to account for scalar relativistic effects was included [144]. I evaluated the Hessian to verify that the optimized geometries correspond to true energy minima. All field-free computations were performed using the Gaussian program [145].

To decompose the field-free interaction energy into terms with clear physical interpretation, I applied the VP-EDS method at the MP2 level of theory using a modified version of the GAMESS (US) program [147]. After optimization and Hessian evaluation of the equilibrium geometries of the complexes, I identified and selected several vibrational modes to be analyzed using the IRS-DA approach. I carried out the field-dependent restricted geometry optimizations using custom computer programs based on the electronic energies and gradients obtained with the Gaussian program, enforcing again tight convergence thresholds [161]. I calculated the nuclear relaxation polarizability using the FF method and applied the VP-EDS method to decompose it into terms with physical origin using a modified in-house version of the GAMESS (US) program.

To demonstrate the interpretive power of the above-described scheme I applied this protocol and analyzed the IR intensity changes upon formation of halogen-bonded complexes formed by pyridine (**pyr**) and perfluorohaloarenes, such as C_6F_5Cl, C_6F_5Br, or C_6F_5I. The structure of the complexes is shown in Figure 5.3, where the nitrogen in the pyridine acts as the halogen bond acceptor and the halogen (Cl, Br, or I) of the perfluorhaloarene acts as the halogen bond donor. The selection of these complexes for this study was driven by sev-

eral key considerations. Firstly, compatibility with infrared spectroscopic measurements was crucial. The far-infrared spectra of these systems allow us to validate my computational results. Secondly, the structural similarity to **A**- series dyes studied in previous chapters (Figures 4.2) played a significant role. This shared motif (pyridine interacting with a perfluorohaloarene) facilitates comparisons and strengthens the connection between this chapter and the previous one. Finally, the size of these complexes enables the application of the VP-EDS method at the computationally efficient MP2 level of theory, adhering to the methodology outlined above.

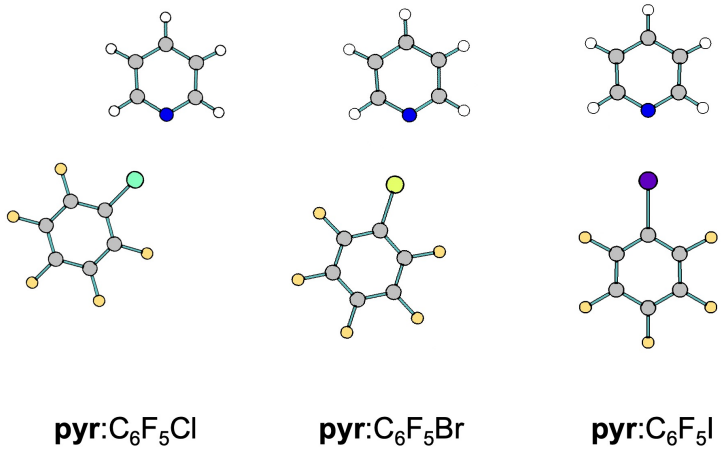

Figure 5.3: Equilibrium geometries of **pyr**:C_6F_5X complexes computed at the MP2/aug-cc-pVDZ-PP level of theory.

The structural features of **pyr**:C_6F_5X complexes exhibit interesting similarities to the **A** and **B** complexes containing C_6F_5X molecules. Notably, the **pyr**:C_6F_5I complex displays the typical linear C–I$\cdots$N bond angle of 180° and a halogen bond distance of 2.739 Å. As the electronegativity of the halogen atom increases (I < Br < Cl), the bond strength weakens. This weakening is manifested by a deviation from linearity in the C–X$\cdots$N bond angle and a corresponding increase in the intermolecular interaction distance. The C–X$\cdots$N bond angles and bond distances for **pyr**:C_6F_5Br and **pyr**:C_6F_5Cl are 174° and 2.770 Å, and 162° and 2.929 Å, respectively.

The interaction energies between pyridine and C_6F_5X molecules were computed at the MP2/aug-cc-PVDZ level of theory. The results, -7.75 kcal/mol (**pyr**:C_6F_5I), -5.07 kcal/mol (**pyr**:C_6F_5Br), and -3.07 kcal/mol (**pyr**:C_6F_5Cl), support the observed weakening trend in halogen bonding with increasing halogen electronegativity. This weakening is reflected both in geometry and the interaction energy values.

Further analysis involved the decomposition of the interaction energy (ΔE) for the **pyr**: C_6F_5X complexes. Figure 5.4 and Table S6.5 present the interaction energies and their components for (a) the **A-3**:C_6F_5X complexes studied in the previous chapter and (b) the corresponding **pyr**:C_6F_5X complexes. The partitionings are ordered according to the

increasing value of the total interaction energy. As mentioned earlier, the decomposition of the interaction energy for the larger **A–3**:C_6F_5X complexes from the previous chapter was done at the Hartree-Fock (HF) level due to computational limitations. In contrast, the partition of the interaction energy for the **pyr**:C_6F_5X could be performed at the MP2 level. For **pyr**:C_6F_5X complexes, the MP2 correlation term ($\Delta E_{corr}^{\mathrm{MP2}}$) has been further partitioned according to Equation 2.6 into the second-order electron correlation correction to the first-order electrostatic interaction ($\varepsilon_{el,r}^{(12)}$), dispersion ($\varepsilon_{disp}^{(20)}$), and the remaining second-order electron correlation effects ($\Delta E_{ex}^{(2)}$) terms.

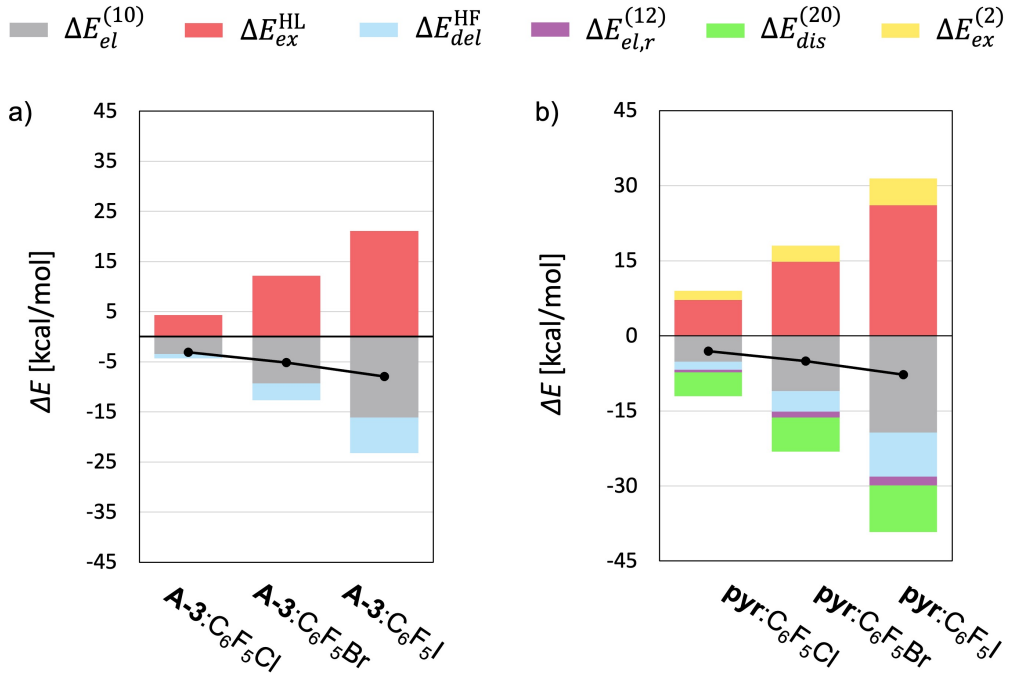

Figure 5.4: Partitioning of the interaction energy (ΔE) for the (a) **A-3**:C_6F_5X and (b) **pyr**:C_6F_5X complexes at the equilibrium geometries at the MP2/aug-cc-pVDZ-PP level of theory. The black dots combined with black lines indicate the total interaction energy.

Comparing the partitioning of ΔE for **A-3** and **pyr** complexes reveals a similar pattern on the relative weight of the HF contribution terms. Furthermore, the decomposition of the interaction energy of **pyr**:C_6F_5X is very similar across the different halogen bond atoms (X = Cl, Br, and I), with the only significant difference found in the magnitude of the contributions. A deeper look into the results unveils a significant destabilizing contribution from the exchange-repulsion term for all complexes. However, this is counterbalanced by the combined effect of the electrostatic and delocalization terms. At the uncorrelated level (without considering electron correlation), this balance results in a very weak predicted binding (Table S6.5). Therefore, the same conclusions can be obtained from these results compared to the analysis of the decomposition of ΔE for **A** and **B**-series dyes. Notably, it highlights the crucial role of electron correlation effects ($\Delta E_{corr}^{\mathrm{MP2}}$), particularly the dispersion term ($\varepsilon_{disp}^{(20)}$), in governing the observed stability of these halogen-bonded systems.

To investigate this further, I conducted a comprehensive analysis exploring the relationship between the VP-EDS terms obtained for the ΔE decomposition of each **A-3**:C_6F_5X complex with their corresponding **pyr**:C_6F_5X complexes in each set. I calculated the linear correlation between the contributing terms to the interaction energies for the three pairs: **pyr**:C_6F_5Cl vs. **A-3**:C_6F_5Cl, **pyr**:C_6F_5Br vs. **A-3**:C_6F_5Br, and **pyr**:C_6F_5I vs. **A-3**:C_6F_5I. The results of this analysis are presented in Figure 5.5. The contributions to the interaction energy of **pyr**:C_6F_5X have been depicted in the y-axis, and the contributions to the interaction energy of **A-3**:C_6F_5X have been depicted in the x-axis. The analysis reveals a strong linear correlation for all three pairs of halogen-bonded complexes. The correlation coefficient (R^2) strengthens progressively from 0.9771 for the Cl-containing systems to 0.9972 for Br and to 0.9977 for I. This trend suggests that the partitioning of the interaction energy, and consequently, the underlying physical origin of the interaction, becomes increasingly similar as the strength of the halogen bond increases. The strong linear correlations observed in Figure 5.5 establish a clear connection between the partitioning of the interaction energy for **A-3**:C_6F_5X and **pyr**:C_6F_5X.

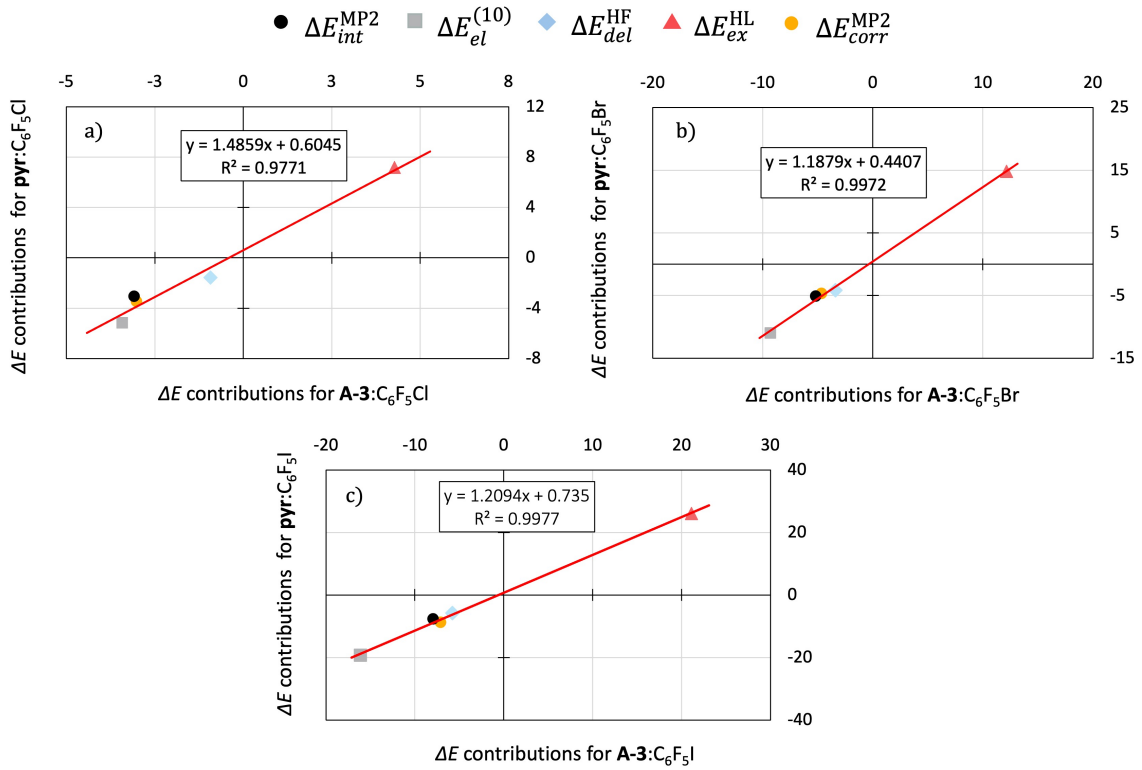

Figure 5.5: Linear regressions between interaction-type contributions for the interaction energy of **A-3**:C_6F_5X complexes and the corresponding terms of interaction energy of **pyr**:C_6F_5X complexes. Energies are given in kcal/mol.

This finding aligns with previous work by my group associates [13, 129], suggesting that the nature of halogen bonding exhibits minimal dependence on the specific chemi-

cal composition of the interacting molecules. Furthermore, similar analyses performed on different **pyr**:C_6F_5X complexes (**pyr**:C_6F_5Cl vs. **pyr**:C_6F_5I, **pyr**:C_6F_5Br vs. **pyr**:C_6F_5I, and **pyr**:C_6F_5Cl vs. **pyr**:C_6F_5Br) yielded comparable results (Figure S6.5). These additional analyses support the conclusion that the partitioning of interaction energy, and consequently, the underlying physical origin of the interaction, remains largely unchanged across various halogen-bonded systems within the **pyr**:C_6F_5X family.

Following the results obtained from calculations, the changes in IR spectra for **pyr**:C_6F_5Cl, **pyr**:C_6F_5Br, and **pyr**:C_6F_5I induced by halogen bonding are displayed in Figure 5.6.

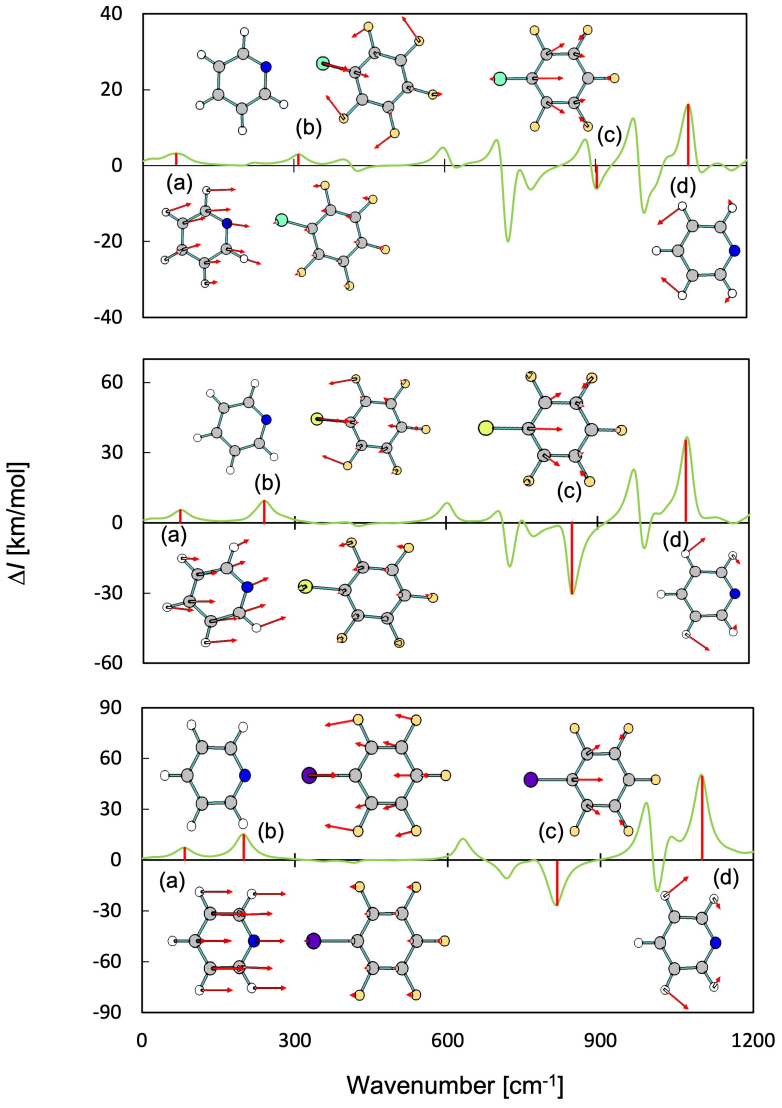

Figure 5.6: Difference IR spectrum obtained by subtracting the simulated IR spectra of pyridine and C_6F_5X from the IR spectrum of **pyr**:C_6F_5X complex, as well as the displacements of (a) the intermolecular vibrational stretching mode (ν_a^{int}), (b) the C-X stretching mode of C_6F_5I, which involves a change the halogen bond distance ($\nu_b^{\mathrm{C-X}}$), (c) one local vibrational mode of C_6F_5I ($\nu_c^{\mathrm{C_6F_5I}}$) and (d) one local vibrational mode of pyridine (ν_c^{pyr}). The top panel is for X=Cl, the middle panel is for X=Br, and the bottom panel is for X=I.

The analysis reveals significant changes in the IR spectra of the subsystems upon complex formation. I have centered the focus on the IRS-DA analysis of four representative bands attributed to a) the intermolecular vibrational mode (ν_a^{int}), b) the C–X stretching, which involves a direct change in the halogen bond distance ($\nu_b^{\text{C-X}}$), and two vibrational modes that involve movements of the atoms of only one monomer: c) a distortion of the ring of the C_6F_5X ($\nu_c^{C_6F_5X}$), and d) a rocking in-plane bending of the hydrogens of the pyridine (ν_d^{pyr}). The advantage of studying these three systems is that they share the same vibrational modes, facilitating a detailed IRS-DA analysis to gain a comprehensive understanding of the interaction across varying halogen bond strengths.

The mode ν_a^{int} is exclusive to the complex and is attributed to the halogen bonding. Therefore, the analysis of the physical origin of ΔI for this band will be performed in the first place. The remaining three vibrational modes share two main characteristics: there is a significant change in the band intensity, and the frequency shifts upon complex formation are modest. This behavior, in accordance with Eq. 5.13, allows for a straightforward decomposition of the observed changes in IR intensity for these bands. However, it's crucial to note that the first two modes (intermolecular vibration and C–X stretching) are distinct from the latter two in terms of their impact on halogen bonding. The significant variations in halogen bond distance observed with the ν_a^{int} and $\nu_b^{\text{C-X}}$ vibrational modes suggest they directly influence the intermolecular interaction. In contrast, the C_6F_5X ring distortion ($\nu_c^{C_6F_5X}$) and pyridine hydrogen rocking (ν_d^{pyr}) modes likely play a less direct role in the interaction due to their minimal impact on the halogen bond distance.

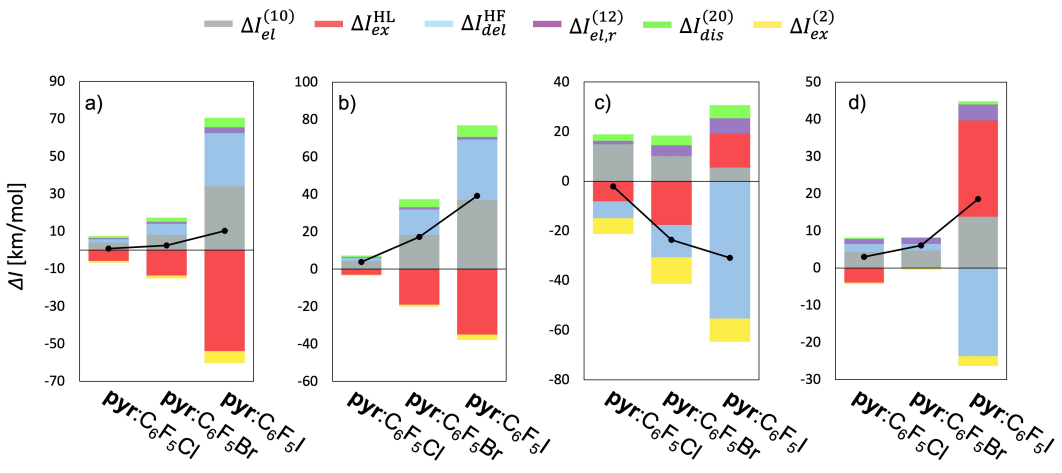

Figure 5.7: Partitioning of the excess IR intensity (ΔI) of (a) the intermolecular vibrational stretching mode (ν_a^{int}), (b) the C–X stretching $\nu_b^{\text{C-X}}$), (c) the distortion of the ring of the C_6F_5X ($\nu_c^{C_6F_5X}$), and (d) the rocking in-plane bending of the hydrogens of the pyridine (ν_d^{pyr}) for the **pyr**:C_6F_5X complexes at the equilibrium geometries at the MP2/aug-cc-pVDZ-PP level of theory. The black dots combined with black lines indicate the total excess IR intensity.

The partitioning of the changes in the IR intensity for a) the intermolecular vibrational mode (ν_a^{int}), b) C–X stretching vibration ($\nu_b^{\text{C-X}}$), c) C_6F_5X ring distortion ($\nu_c^{C_6F_5X}$), and d) pyridine hydrogen rocking (ν_d^{pyr}) of the three **pyr**:C_6F_5X complexes is presented in Figure 5.7 and Table S6.5.

The analysis of the ΔI partitioning for the ν_a^{int} (Figure 5.7a) reveals trends similar to those observed for interaction energy. The largest changes in IR intensity occur in the complex with C_6F_5I, and the intensity decreases as the electronegativity of the halogen atom increases from I to Cl.

The similar trends between ΔE and ΔI_a are further supported by the linear correlation analysis presented in Table 5.1. The high R^2 value of 0.93 indicates a strong linear relationship between these two properties across the three complexes. This finding suggests a close link between the strength of the halogen bond and the intensity changes observed in the intermolecular vibrational mode. The strong correlation observed between interaction energy and change in IR intensity extends to all four investigated vibrational modes. The lowest R^2 value is 0.88, indicating a significant linear relationship in each case. This correlation observed for all the vibrational modes strongly confirms that the strength of the halogen bond directly influences the changes in IR intensity across these vibrational modes.

The partitioning of the IR intensity for the intermolecular vibrational mode for each complex mirrors the decomposition of ΔE for their corresponding complex. The strong linear correlation between the decomposed terms of ΔE and ΔI_a with $R^2 > 0.89$, suggests that both properties share a common underlying physical origin. This correlation strengthens as the intermolecular interaction intensifies, reaching its peak for the **pyr**:C_6F_5I complex.

Table 5.1: Coefficient of determination (R^2) of the linear fits between the excess IR intensity contributions and interaction energy contributions for the three **pyr**:C_6F_5X complexes for each vibrational mode.

Vibrational Mode	**pyr**:C_6F_5Cl	**pyr**:C_6F_5Br	**pyr**:C_6F_5I
ν_a^{int}	0.89	0.93	0.93
$\nu_b^{\text{C-X}}$	0.78	0.89	0.88
$\nu_c^{C_6F_5X}$	0.57	0.62	0.08
ν_d^{pyr}	0.76	0.41	0.22

The parallelism between the contribution of each of the terms to the two properties highlights the influence of halogen bonding on the IR spectra. Specifically, the changes in the IR intensity for ν_a^{int} are associated with a dominant exchange-repulsion contribution, although electrostatic and delocalization terms partially counterbalance this term, leading to a low stabilizing energy at the HF level. Consequently, taking into account electron correlation effects, such as dispersion, is crucial to understanding the IR intensity of these

vibrational modes of molecular complexes formed by halogen bonding. Interestingly, the relative weight of the dispersion contribution diminishes as the halogen atom's electronegativity increases, aligning with the observed trends in ΔE (Table S6.5).

Similarly, strong linear correlations between the decomposition terms of ΔE and ΔI for the $\nu_b^{\text{C-X}}$ band of **pyr**:C_6F_5Br and **pyr**:C_6F_5I are observed too (Table 5.1). In contrast, a weaker linear correlation for C_6F_5Cl can be found, potentially due to the significant deviation of the C–X $\cdots$ N angle from 180°, which decreases the coupling of the $\nu_b^{\text{C-X}}$ vibration with the halogen bond distance. It is interesting to notice that, although the partitioning of ΔI for the ν_a^{int} and $\nu_b^{\text{C-X}}$ bands correlates with the decomposition of ΔE for each system, they present interesting differences, as it can be seen in Figure 5.7b. Similar to ν_a^{int}, the ΔI partitioning for the C–X stretching vibration shows contributions from electrostatic and delocalization terms that increase the IR intensity, partially counterbalanced by an exchange-repulsion term that decreases it. However, unlike ν_a^{int}, the dominant contributor to ΔI is the electrostatic term rather than the exchange-repulsion term. In fact, the analysis suggests that the ΔI change for the C–X stretching vibration can be reliably predicted by the electrostatic term alone due to the cancellation of the opposing contributions from other terms (Table S6.5). Consequently, the results show that for this type of vibrational mode, the electron-correlation contributions do not play a pivotal role and the changes in the IR intensity can be explained at the HF level.

Finally, the analysis of the partition for the changes in the IR intensity for $\nu_c^{\text{C}_6\text{F}_5\text{X}}$ and ν_d^{pyr} vibrational modes leads to different results. While strong linear correlations are observed between the total changes in interaction energy and ΔI for these modes (see Table 5.1), their decompositions differ significantly from the other vibrational modes. This difference is attributed to the fact that $\nu_c^{\text{C}_6\text{F}_5\text{X}}$ and ν_d^{pyr} do not induce significant changes in the halogen bond interaction. In contrast, ν_a^{int} and $\nu_b^{\text{C-X}}$ are directly involved in the change of the halogen bond length. Consequently, the partitioning of their change in the IR intensity across the complexes varied considerably (Table 5.1). The different decomposition of the change in the IR intensity of each **pyr**:C_6F_5X complex for these two vibrational modes makes it difficult to give a general analysis. For instance, the predominant contribution for $\nu_c^{\text{C}_6\text{F}_5\text{Br}}$, $\nu_c^{\text{C}_6\text{F}_5\text{Cl}}$, and $\nu_c^{\text{C}_6\text{F}_5\text{I}}$ is $\Delta I_{el}^{(10)}$, $\Delta I_{ex}^{\text{HL}}$, and $\Delta I_{del}^{\text{HF}}$, respectively. The notable differences between different systems lead to a weak correlation between the decomposition terms of ΔE and ΔI_a. This finding suggests that the IR intensity changes observed in these modes upon complex formation do not share a common underlying physical origin with the interaction energy itself. The results obtained from this work highlight the power of the Infrared Spectra Decomposition Analysis method. It allows for the determination of strong correlations between ΔI partitioning and ΔE decomposition for modes that significantly impact the halogen bond distance (e.g., intermolecular vibration and C–X stretching). However, no such correlation is found for other vibrational modes analyzed in this study.

To assess the broader applicability of these findings, I conducted an IRS-DA analysis on two small halogen-bonded systems (HCN:BrF and HCN:IF) and three small hydrogen-bonded complexes (HCN:HCl, HCN:HNC, and HCN:HCN). The decomposition of ΔE and ΔI for three vibrational modes of each system was performed. Similar to the statistical analysis of **pyr**:C_6F_5X complexes, a strong linear correlation ($R^2 > 0.83$) exists between the decomposition terms of ΔI and ΔE for the intermolecular stretching modes across all five complexes. However, for the local vibrational modes, such a linear correlation is typically not found, as indicated by coefficients of determination (R^2) ranging between 0.20 and 0.80.

Overall, the results obtained from these diverse systems support the conclusions drawn for **pyr**:C_6F_5X and solidify the effectiveness of IRS-DA. This methodology offers a powerful tool for deciphering the connection between intermolecular interactions and the resulting changes in spectroscopic signatures. Notably, IRS-DA's ability to differentiate between the behavior of different vibrational modes further highlights its interpretative power.

CHAPTER 6

Conclusions

The research presented in this dissertation aimed to increase the understanding of intermolecular interactions and their effects on the spectroscopic properties of organic dyes. Specifically, the results of this thesis are split into two main blocks: (a) The computational analysis of the stability of halogen bonding in complexes formed by BF/BF_2 dyes and perfluorohaloarenes, and the assessment of the impact of the halogen bond on the photophysical properties of the dyes. And (b) the development and application of a new methodology to determine the physical origin of spectral changes in infrared spectra upon the formation of molecular complexes composed of the same heterocyclic moiety as in studied dyes.

In the first block, I performed theoretical studies of novel boron-containing probes interacting with perfluorohaloarenes through halogen bonding at a nitrogen atom and examined the photophysical properties of these complexes. Analysis of the electronic structures of two investigated series of dyes revealed significant patterns. In particular, the interaction between perfluorohaloarenes and boron-containing dyes at the pyridine ring, located outside the charge transfer (CT) pathway, led to modifications in the photophysical properties of the dye. Thermodynamic studies showed that, under the experimental conditions, the only halogen bond complexes formed involved any dye of series **A** and C_6F_5I. These complexes exhibited a slight redshift in absorption maximum wavelength and a substantial redshift in emission maximum wavelength, which were attributed to the pull effect of halogen bonding on the electron density of the dyes, thereby increasing CT along the conjugated systems. The second set of boron-containing dyes featured two halogen bond acceptor sites: one located within the CT pathway and another close to the boron-center electron acceptor group outside the CT pathway. NMR measurements and thermodynamic stud-

ies confirmed that only complexes involving the dyes of series **B** and C_6F_5I were formed. However, due to the proximity of the halogen bond acceptor sites to the boron-center electron acceptor group, the strength of the intermolecular interactions was lower than in the previous set of dyes **A**. Despite these weaker interactions, computational investigations into the impact of halogen bonding on different acceptor sites within dyes **B** revealed distinct trends in photophysical properties. Specifically, complexes where the halogen bond was situated near the boron group, outside of the charge transfer (CT) pathway, exhibited characteristic shifts in absorption and emission wavelengths. These shifts, namely a small redshift in absorption maximum wavelength and a significant redshift in emission maximum wavelength, aligned well with experimental data. This feature was assigned to the effect of the halogen bonding on the electron density distribution within the dyes, which facilitates the CT process, in agreement with the observed effects in dyes of series **A**.

In the second block, a novel methodology to decompose changes in IR spectrum intensity upon complex formation into terms of intermolecular interaction energy components (electrostatic, exchange, induction, dispersion) was developed and applied. The development of this method was based on the relation between the analytical expression of the nuclear relaxation polarizability and IR intensity, taking into account that both depend on the second derivative of the energy with respect to the normal coordinates. Consequently, a direct relationship was established between changes in both properties for a specific vibrational mode caused by an intermolecular interaction. This approach enabled the decomposition of changes in IR intensity due to intermolecular interactions into terms with different physical origin through energy decomposition analysis. Applying this method to real systems led to interesting conclusions, including establishing linear correlations between the interaction energy and the change in IR intensity of the studied normal mode bands. The variational-perturbational energy decomposition scheme (VP-EDS) was employed to decompose intermolecular interaction energies and changes in IR intensity upon complex formation into terms with different physical origin. A linear correlation between contributing physical terms to the interaction energy of the complexes and contributing physical terms to the total change in IR intensity of vibrational modes that involve significant changes in the intermolecular bond distance was found, suggesting that the physical origin of the interaction energy and the changes in the IR intensity for these vibrational modes have the same physical origin. This conclusion was confirmed by studying a different set of small hydrogen- and halogen-bonded complexes, which led to similar results.

In summary, the findings presented in this dissertation represent a significant step towards understanding the impact of halogen bonding on the electronic and vibrational spectroscopy of organic dyes, facilitating the development of new compounds and materials with diverse applications in various scientific fields.

Bibliography

[1] A. D. Buckingham, B. D. Utting. Intermolecular Forces. *Annu. Rev. Phys. Chem.* **1970**, 21, 287-316.

[2] G. Cavallo, P. Metrangolo, R. Milani, T. Pilati, A. Priimagi, G. Resnati, G. Terraneo. The Halogen Bond. *Chem. Rev.* **2016**, 116, 2478-2601.

[3] M. Erdélyi. Application of the Halogen Bond in Protein Systems. *Biochemistry* **2017**, 56, 2759-2761.

[4] J. Teyssandier, K. S. Mali, S. De Feyter. Halogen Bonding in Two-Dimensional Crystal Engineering. *ChemistryOpen* **2020**, 9, 225-241.

[5] R. Kampes, S. Zechel, M. D. Hager, U. S. Schubert. Halogen Bonding in Polymer Science: Towards New Smart Materials. *Chem. Sci.* **2021**, 12, 9275-9286.

[6] A. Caballero, F. Zapata, N. G. White, P. J. Costa, V. Félix, P. D. Beer. A Halogen-Bonding Catenane for Anion Recognition and Sensing. *Angew. Chem. Int. Ed.* **2012**, 51, 1876-1880.

[7] A. Amonov, S. Scheiner. Relation Between Halogen Bond Strength and IR and NMR Spectroscopic Markers. *Molecules* **2023**, 28, 7520.

[8] W. H. Perkin. On Mauve or Aniline-Purple. *R. Soc.* **1863**, 12, 713-715.

[9] J. P. Griess. On New Nitrogenous Derivatives of the Phenyl- and Benzoyl-Series. *P. R. Soc. London* **1859**, 9, 594-597.

[10] M. M. Lerch, M. Medved′, A. Lapini, A. D. Laurent, A. Iagatti, L. Bussotti, W. Szymański, W. J. Buma, P. Foggi, M. Di Donato, B. L. Feringa. Tailoring Pho-

toisomerization Pathways in Donor-Acceptor Stenhouse Adducts: The Role of the Hydroxy Group. *J. Phys. Chem. A* **2018**, 122, 955-964.

[11] M. Chapran, E. Angioni, N. J. Findlay, B. Breig, V. Cherpak, P. Stakhira, T. Tuttle, D. Volyniuk, J. V. Grazulevicius, Y. A. Nastishin, O. D. Lavrentovich, P. J. Skabara. An Ambipolar BODIPY Derivative for a White Exciplex OLED and Cholesteric Liquid Crystal Laser Toward Multifunctional Devices. *ACS Appl. Mater. Interfaces* **2017**, 9, 4750-4757.

[12] X. Wang, H. Liu, J. Wu, Z. Xie, Q. Zhang. Synthesis and Photovoltaic Properties of New Conjugated Polymers Based on Red Hair Pigment Skeleton. *Dyes Pigm.* **2019**, 160, 823-829.

[13] R. Zaleśny, N. Szczotka, A. Grabarz, B. Ośmiałowski. Design of Two-Photon-Excited Fluorescent Dyes Containing Fluoroborylene Groups. *ChemPhotoChem* **2019**, 3, 719-726.

[14] J. Fabian, H. Nakazumi, M. Matsuoka. Near-Infrared Absorbing Dyes. *Chem. Rev.* **1992**, 92, 1197-1226.

[15] T. Weil, T. Vosch, J. Hofkens, K. Peneva, K. Müllen. The Rylene Colorant Family-Tailored Nanoemitters for Photonics Research and Applications. *Angew. Chem. Int. Ed.* **2010**, 49, 9068-9093.

[16] K. Kawaoka, D. R. Kearns. Emission Properties of Tetracene-Pyrene and Pentacene-Pyrene Mixed Crystals. *J. Chem. Phys.* **1964**, 41, 2095-2097.

[17] M. R. Wasielewski. Photoinduced Electron Transfer in Supramolecular Systems for Artificial Photosynthesis. *Chem. Rev.* **1992**, 92, 435-461.

[18] N. Kitamura, T. Fukagawa, S. Kohtani, S. Kitoh, K.-K. Kunimoto, R. Nakagaki. Synthesis, Absorption and Fluorescence Properties and Crystal Structures of 7-Aminocoumarin Derivatives. *J. Photoch. Photobio. A* **2007**, 188, 378-386.

[19] M. Beija, C. A. M. Afonso, J. M. G. Martinho. Synthesis and Applications of Rhodamine Derivatives as Fluorescent Probes. *Chem. Soc. Rev.* **2009**, 38, 2410-2433.

[20] A. Mishra, R. K. Behera, P. K. Behera, B. K. Mishra, G. B. Behera. Cyanines During the 1990s: A Review. *Chem. Rev.* **2000**, 100, 1973-2012.

[21] L. Beverina, P. Salice. Squaraine Compounds: Tailored Design and Synthesis towards a Variety of Material Science Applications. *Eur. J. Org. Chem.* **2010**, 7, 1207-1225.

[22] A. Loudet, K. Burgess. BODIPY Dyes and Their Derivatives: Syntheses and Spectroscopic Properties. *Chem. Rev.* **2007**, 107, 4891-4932.

[23] G. Ulrich, R. Ziessel, A. Harriman. The Chemistry of Fluorescent BODIPY Dyes: Versatility Unsurpassed. *Angew. Chem. Int. Ed.* **2008**, 47, 1184-1201.

[24] A. Treibs, F. Kreuzer. Difluorboryl-Komplexe von Di- und Tripyrrylmethenen. *Liebigs Ann. Chem.* **1968**, 718, 208-223.

[25] G. Ulrich, C. Goze, M. Guardigli, A. Roda, R. Ziessel. Pyrromethene Dialkynyl Borane Complexes for "Cascatelle" Energy Transfer and Protein Labeling. *Angew. Chem. Int. Ed.* **2005**, 44, 3694-3698.

[26] C. Wan, A. Burghart, J. Chen, F. Bergström, L. B.- Johansson, M. F. Wolford, T. G. Kim, M. R. Topp, R. M. Hochstrasser, K. Burgess. Anthracene-BODIPY Cassettes: Syntheses and Energy Transfer. *Chem. Eur. J.* **2003**, 9, 4430-4441.

[27] R. Ziessel, C. Goze, G. Ulrich, M. Césario, P. Retailleau, A. Harriman, J. P. Rostron. Intramolecular Energy Transfer in Pyrene-BODIPY Molecular Dyads and Triads. *Chem. Eur. J.* **2005**, 11, 7366-7378.

[28] C. Goze, G. Ulrich, L. J. Mallon, B. D. Allen, A. Harriman, R. Ziessel. Synthesis and Photophysical Properties of Borondipyrromethene Dyes Bearing Aryl Substituents at the Boron Center. *J. Am. Chem. Soc.* **2006**, 128, 10231-10239.

[29] A. Harriman, G. Izzet, R. Ziessel. Rapid Energy Transfer in Cascade-Type BODIPY Dyes. *J. Am. Chem. Soc.* **2006**, 128, 10868-10875.

[30] L. Hung, C. Chen. Recent Progress of Molecular Organic Electroluminescent Naterials and Devices. *Mater. Sci. Eng. R Rep.* **2002**, 39, 143-222.

[31] A. Mishra, P. Bäuerle. Small Molecule Organic Semiconductors on the Move: Promises for Future Solar Energy Technology. *Angew. Chem. Int. Ed.* **2012**, 51, 2020-2067.

[32] R. Ziessel, A. Harriman. Artificial Light-Harvesting Antennae: Electronic Energy Transfer by Way of Molecular Funnels. *Chem. Commun.* **2011**, 47, 611-631.

[33] G. Ulrich, R. Ziessel. Convenient and Efficient Synthesis of Functionalized Oligopyridine Ligands Bearing Accessory Pyrromethene-BF_2 Fluorophores. *J. Org. Chem.* **2004**, 69, 2070-2083.

[34] T. Ueno, Y. Urano, H. Kojima, T. Nagano. Mechanism-Based Molecular Design of Highly Selective Fluorescence Probes for Nitrative Stress. *J. Am. Chem. Soc.* **2006**, 128, 10640-10641.

[35] G. Ulrich, S. Goeb, A. De Nicola, P. Retailleau, R. Ziessel. Chemistry at Boron: Synthesis and Properties of Red to Near-IR Fluorescent Dyes Based on Boron-Substituted Diisoindolomethene Frameworks. *J. Org. Chem.* **2011**, 76, 4489-4505.

[36] A. M. Grabarz, B. Jędrzejewska, A. Skotnicka, N. A. Murugan, F. Patalas, W. Bartkowiak, D. Jacquemin, B. Ośmiałowski. The Impact of the Heteroatom in a Five-Membered Ring on the Photophysical Properties of Difluoroborates. *Dyes Pigm.* **2019**, 170, 107481.

[37] B. Jędrzejewska, A. Skotnicka, A. D. Laurent, M. Pietrzak, D. Jacquemin, B. Ośmiałowski. Influence of the Nature of the Amino Group in Highly Fluorescent Difluoroborates Exhibiting Intramolecular Charge Transfer. *J. Org. Chem.* **2018**, 83, 7779-7788.

[38] B. Dziuk, B. Ośmiałowski, B. Zarychta, K. Ejsmont, L. Chęcińska. Symmetric Fluoroborate and its Boron Modification: Crystal and Electronic Structures. *Crystals* **2019**, 9, 662.

[39] M. Santra, H. Moon, M.-H. Park, T.-W. Lee, Y. K. Kim, K. H. Ahn. Dramatic Substituent Effects on the Photoluminescence of Boron Complexes of 2-(Benzothiazol-2-yl)phenols. *Chem. Eur. J.* **2012**, 18, 9886-9893.

[40] M. Głodek, E. F. Petrusevich, D. Plażuk, D. Jacquemin, B. Ośmiałowski. Polyaromatic hydrocarbon Antennas as Tools for Tuning Properties of Push-Pull Difluoroborates. *Dyes Pigm.* **2023**, 212, 111112.

[41] B. Ośmiałowski, B. Dziuk, K. Ejsmont, L. Chęcińska, L. Dobrzańska. Effect of Conjugated System Extension on Structural Features and Electron-Density Distribution in Charge-Transfer Difluoroborates. *Acta Crystallogr. C* **2021**, 77, 807-813.

[42] I. Knysh, A. Kozakiewicz-Piekarz, A. Wojtczak, D. Plażuk, G. Baryshnikov, R. Valiev, R. Nasibullin, H. Ågren, D. Jacquemin, B. Ośmiałowski, R. Zaleśny. Less is More: on the Effect of Benzannulation on the Solid-State Emission of Difluoroborates. *J. Mater. Chem. C* **2021**, 9, 15820-15830.

[43] A. M. Grabarz, B. Jędrzejewska, A. Zakrzewska, R. Zaleśny, A. D. Laurent, D. Jacquemin, B. Ośmiałowski. Photophysical Properties of Phenacylphenantridine Difluoroboranyls: Effect of Substituent and Double Benzannulation. *J. Org. Chem.* **2017**, 82, 1529-1537.

[44] A. M. Grabarz, A. D. Laurent, B. Jędrzejewska, A. Zakrzewska, D. Jacquemin, B. Ośmiałowski. The Influence of the π-Conjugated Spacer on Photophysical Properties of Difluoroboranyls Derived from Amides Carrying a Donor Group. *J. Org. Chem.* **2016**, 81, 2280-2292.

[45] G. Nawn, S. R. Oakley, M. B. Majewski, R. McDonald, B. O. Patrick, R. G. Hicks. Redox-Active, Near-Infrared Dyes Based on 'Nindigo' (Indigo-N,N′-Diarylimine) Boron Chelate Complexes. *Chem. Sci.* **2013**, 4, 612-621.

[46] D. Curiel, M. Más-Montoya, L. Usea, A. Espinosa, R. A. Orenes, P. Molina. Indolocarbazole-Based Ligands for Ladder-Type Four-Coordinate Boron Complexes. *Org. Lett.* **2012**, 14, 3360-3363.

[47] S. Hapuarachchige, G. Montaño, C. Ramesh, D. Rodriguez, L. H. Henson, C. C. Williams, S. Kadavakkollu, D. L. Johnson, C. B. Shuster, J. B. Arterburn. Design and Synthesis of a New Class of Membrane-Permeable Triazaborolopyridinium Fluorescent Probes. *J. Am. Chem. Soc.* **2011**, 133, 6780-6790.

[48] P. Rybczyński, M. H. E. Bousquet, A. Kaczmarek-Kędziera, B. Jędrzejewska, D. Jacquemin, B. Ośmiałowski. Controlling the fluorescence quantum yields of benzothiazole-difluoroborates by optimal substitution. *Chem. Sci.* **2022**, 13, 13347-13360.

[49] M. A. Kaczorowska, A. Kaczmarek-Kędziera, B. Ośmiałowski. Tautomeric equilibrium, proton affinity and mass spectrometry fragmentation of flexible hydrogen-bonded precursors and rigid N→BF_2 fluorescent dyes. *Sci. Rep.* **2021**, 11, 15995.

[50] T. N. Moshkina, E. V. Nosova, G. N. Lipunova, M. S. Valova, E. F. Petrusevich, R. Zaleśny, B. Ośmiałowski, V. N. Charushin. Substituted 2-(2-hydroxyphenyl)-3H-quinazolin-4-ones and their difluoroboron complexes: Synthesis and photophysical properties. *Spectrochim. Acta A* **2021**, 252, 119497.

[51] E. F. Petrusevich, M. Głodek, M. A. Antoniak, T. Muzioł, D. Plażuk, A. Siomra, M. Nyk, B. Ośmiałowski, R. Zaleśny. Difluoroborate-Based Bichromophores: Symmetry Relaxation and Two-Photon Absorption. *Spectrochim. Acta A* **2023**, 295, 122600.

[52] I. Knysh, M. B. Jassar, B. Ośmiałowski, R. Zaleśny, D. Jacquemin. In Silico Screening of Two-Photon Absorption Properties of a Large Set of Bis-Difluoroborate Dyes. *ChemPhotoChem* **2022**, 6, e202200137.

[53] E. F. Petrusevich, B. Ośmiałowski, R. Zaleśny, M. M. Alam. Two-Photon Absorption Activity of BOPHY Derivatives: Insights from Theory. *J. Phys. Chem. A* **2021**, 125, 2581-2587.

[54] B. Ośmiałowski, E. F. Petrusevich, K. C. Nawrot, B. K. Paszkiewicz, M. Nyk, J. Zielak, B. Jędrzejewska, J. M. Luis, D. Jacquemin, R. Zaleśny. Tailoring the Nonlinear Absorption of Fluorescent Dyes by Substitution at a Boron Center. *J. Mater. Chem. C* **2021**, 9, 6225-6233.

[55] B. Ośmiałowski, E. F. Petrusevich, M. A. Antoniak, I. Grela, M. A. Bin Jassar, M. Nyk, J. M. Luis, B. Jędrzejewska, R. Zaleśny, D. Jacquemin. Controlling Two-Photon Action Cross Section by Changing a Single Heteroatom Position in Fluorescent Dyes. *J. Phys. Chem. Lett.* **2020**, 11, 5920-5925.

[56] S. Draxler, M. E. Lippitsch, I. Klimant, H. Kraus, O. S. Wolfbeis. Effects of Polymer Matrixes on the Time-Resolved Luminescence of a Ruthenium Complex Quenched by Oxygen. *J. Phys. Chem.* **1995**, 99, 3162-3167.

[57] B. M. Bell, T. P. Clark, T. S. D. Vries, Y. Lai, D. S. Laitar, T. J. Gallagher, J. Jeon, K. L. Kearns, T. McIntire, S. Mukhopadhyay, H. Na, T. D. Paine, A. A. Rachford. Boron-based TADF Emitters with Improved OLED Device Efficiency Roll-off and Long Lifetime. *Dyes Pigm.* **2017**, 141, 83-92.

[58] B. Jędrzejewska, B. Ośmiałowski. Difluoroboranyl Derivatives as Efficient Panchromatic Photoinitiators in Radical Polymerization Reactions. *Polym. Bull.* **2018**, 75, 3267-3281.

[59] J. Shanmugapriya, K. Rajaguru, G. Sivaraman, S. Muthusubramanian, N. Bhuvanesh. Boranil Dye Based "Turn-on" Fluorescent Probes for Detection of Hydrogen Peroxide and Their Cell Imaging Application. *RSC Adv.* **2016**, 6, 85838-85843.

[60] L. A. Juárez, A. M. Costero, M. Parra, S. Gil, F. Sancenón, R. Martínez-Máñez. A New Chromo-Fluorogenic Probe Based on BODIPY for NO_2 Detection in Air. *Chem. Commun.* **2015**, 51, 1725-1727.

[61] A. J. Taylor, R. Hein, S. C. Patrick, J. J. Davis, P. D. Beer. Anion Sensing Through Redox-Modulated Fluorescent Halogen Bonding and Hydrogen Bonding Hosts. *Angew. Chem. Int. Ed.* **2023**, 63, e202315959.

[62] G. I. Kaplan, Intermolecular Interactions, John Wiley & Sons, Ltd, **2006**.

[63] A. Stone, The Theory of Intermolecular Forces, Oxford University Press, **2013**.

[64] A. Tkatchenko. Current Understanding of Van der Waals Effects in Realistic Materials. *Adv. Funct. Mater.* **2015**, 25, 2054-2061.

[65] R. S. Mulliken. Structures of Complexes Formed by Halogen Molecules with Aromatic and with Oxygenated Solvents. *J. Am. Chem. Soc.* **1950**, 72, 600-608.

[66] P. Metrangolo, F. Meyer, T. Pilati, G. Resnati, G. Terraneo. Halogen Bonding in Supramolecular Chemistry. *Angew. Chem. Int. Ed.* **2008**, 47, 6114-6127.

[67] P. Politzer, J. S. Murray, T. Clark. Halogen Bonding: an Electrostatically-Driven Highly Directional Noncovalent Interaction. *Phys. Chem. Chem. Phys.* **2010**, 12, 7748-7757.

[68] E. Parisini, P. Metrangolo, T. Pilati, G. Resnati, G. Terraneo. Halogen Bonding in Halocarbon-Protein Complexes: a Structural Survey. *Chem. Soc. Rev.* **2011**, 40, 2267-2278.

[69] P. Metrangolo, J. S. Murray, T. Pilati, P. Politzer, G. Resnati, G. Terraneo. Fluorine-Centered Halogen Bonding: A Factor in Recognition Phenomena and Reactivity. *Cryst. Growth Des.* **2011**, 11, 4238-4246.

[70] M. Cametti, B. Crousse, P. Metrangolo, R. Milani, G. Resnati. The Fluorous Effect in Biomolecular Applications. *Chem. Soc. Rev.* **2012**, 41, 31-42.

[71] H. A. Bent. Structural Chemistry of Donor-Acceptor Interactions. *Chem. Rev.* **1968**, 68, 587-648.

[72] T. Brinck, J. S. Murray, P. Politzer. Surface Electrostatic Potentials of Halogenated Methanes as Indicators of Ddirectional Intermolecular Interactions. *Int. J. Quantum Chem.* **1992**, 44, 57-64.

[73] T. Brinck, J. S. Murray, P. Politzer. Molecular Surface Electrostatic Potentials and Local Ionization Energies of Group V-VII Hydrides and Their Anions: Relationships for Aqueous and Gas-Phase Acidities. *Int. J. Quantum Chem.* **1993**, 48, 73-88.

[74] J. S. Murray, K. Paulsen, P. Politzer. Molecular Surface Electrostatic Potentials in the Analysis of Non-Hydrogen-Bonding Noncovalent Interactions. *Proc. Indian Acad. Sci. (Chem. Sci.)* **1994**, 106, 267-275.

[75] J. S. Murray, P. Lane, P. Politzer. Expansion of the σ-hole Concept. *J. Mol. Model.* **2009**, 15, 723-729.

[76] G. Desiraju, P. Ho, L. Kloo, A. Legon, R. Marquardt, P. Metrangolo, P. Politzer, G. Resnati, K. Rissanen. Definition of the Halogen Bond (IUPAC Recommendations 2013). *Pure Appl. Chem.* **2013**, 85, 1711-1713.

[77] M. Fourmigué. Halogen Bonding: Recent Advances. *Curr. Opin. Solid St. M.* **2009**, 13, 36-45.

[78] J. P. M. Lommerse, A. J. Stone, R. Taylor, F. H. Allen. The Nature and Geometry of Intermolecular Interactions between Halogens and Oxygen or Nitrogen. *J. Am. Chem. Soc.* **1996**, 118, 3108-3116.

[79] Z. P. Shields, J. S. Murray, P. Politzer. Directional Tendencies of Halogen and Hydrogen Bonds. *Int. J. Quantum Chem.* **2010**, 110, 2823-2832.

[80] S. M. Huber, J. D. Scanlon, E. Jimenez-Izal, J. M. Ugalde, I. Infante. On the Directionality of Halogen Bonding. *Phys. Chem. Chem. Phys.* **2013**, 15, 10350-10357.

[81] G. R. Desiraju, R. L. Harlow. Cyano-Halogen interactions and Their Role in the Crystal Structures of the 4-Halobenzonitriles. *J. Am. Chem. Soc.* **1989**, 111, 6757-6764.

[82] H. L. Nguyen, P. N. Horton, M. B. Hursthouse, A. C. Legon, D. W. Bruce. Halogen Bonding: A New Interaction for Liquid Crystal Formation. *J. Am. Chem. Soc.* **2004**, 126, 16-17.

[83] L. Kohlmeier, M. Kohlmeier. Adipose Tissue as a Medium for Epidemiologic Exposure Assessment. *Environ. Health Persp.* **1995**, 103, 99-106.

[84] O. S. Faleye, B. R. Boya, J.-H. Lee, I. Choi, J. Lee. Halogenated Antimicrobial Agents to Combat Drug-Resistant Pathogens. *Pharmacol. Rev.* **2024**, 76, 90–141.

[85] M. R. Scholfield, C. M. V. Zanden, M. Carter, P. S. Ho. Halogen Bonding (X-Bonding): A Biological Perspective. *Protein Sci.* **2013**, 22, 139-152.

[86] A. Mukherjee, S. Tothadi, G. R. Desiraju. Halogen Bonds in Crystal Engineering: Like Hydrogen Bonds yet Different. *Acc. Chem. Res.* **2014**, 47, 2514-2524.

[87] A. Priimagi, G. Cavallo, P. Metrangolo, G. Resnati. The Halogen Bond in the Design of Functional Supramolecular Materials: Recent Advances. *Acc. Chem. Res.* **2013**, 46, 2686-2695.

[88] J. Zhong, J. Sun, K. Ye, R. Lu. Halogen Effect in Photomechanical Molecular Crystals. *J. Mater. Chem. C* **2023**, 11, 16452-16472.

[89] M. Yamada, M. Kondo, J.-i. Mamiya, Y. Yu, M. Kinoshita, C. J. Barrett, T. Ikeda. Photomobile Polymer Materials: Towards Light-Driven Plastic Motors. *Angew. Chem. Int. Ed.* **2008**, 47, 4986-4988.

[90] H. Guo, C. Liang, T.-P. Ruoko, H. Meteling, B. Peng, H. Zeng, A. Priimagi. Programmable and Self-Healable Liquid Crystal Elastomer Actuators Based on Halogen Bonding. *Angew. Chem. Int. Ed.* **2023**, 62, e202309402.

[91] S. M. Huber, E. Jimenez-Izal, J. M. Ugalde, I. Infante. Unexpected Trends in Halogen-Bond Based Noncovalent Adducts. *Chem. Commun.* **2012**, 48, 7708-7710.

[92] C. W. Kellett, P. Kennepohl, C. P. Berlinguette. π Covalency in the Halogen Bond. *Nat. Commun.* **2020**, 11, 3310.

[93] B. W. D'Andrade, S. R. Forrest. White Organic Light-Emitting Devices for Solid-State Lighting. *Adv. Mater.* **2004**, 16, 1585-1595.

[94] S. Varghese, S. Das. Role of Molecular Packing in Determining Solid-State Optical Properties of π-Conjugated Materials. *J. Phys. Chem. Lett.* **2011**, 2, 863-873.

[95] D. Yan, A. Delori, G. O. Lloyd, T. Friščić, G. M. Day, W. Jones, J. Lu, M. Wei, D. G. Evans, X. Duan. A Cocrystal Strategy to Tune the Luminescent Properties of Stilbene-Type Organic Solid-State Materials. *Angew. Chem. Int. Ed.* **2011**, 50, 12483-12486.

[96] B. Ventura, A. Bertocco, D. Braga, L. Catalano, S. d'Agostino, F. Grepioni, P. Taddei. Luminescence Properties of 1,8-Naphthalimide Derivatives in Solution, in Their Crystals and in Co-crystals: Toward Room-Temperature Phosphorescence from Organic Materials. *J. Phys. Chem. C* **2014**, 118, 18646-18658.

[97] S. d'Agostino, F. Grepioni, D. Braga, B. Ventura. Tipping the Balance with the Aid of Stoichiometry: Room Temperature Phosphorescence versus Fluorescence in Organic Cocrystals. *Cryst. Growth Des.* **2015**, 15, 2039-2045.

[98] U. Mayerhöffer, F. Würthner. Halogen-Arene Interactions Assist in Self-Assembly of Dyes. *Angew. Chem. Int. Ed.* **2012**, 51, 5615-5619.

[99] F. Zapata, A. Caballero, N. G. White, T. D. W. Claridge, P. J. Costa, V. Félix, P. D. Beer. Fluorescent Charge-Assisted Halogen-Bonding Macrocyclic Halo-Imidazolium Receptors for Anion Recognition and Sensing in Aqueous Media. *J. Am. Chem. Soc.* **2012**, 134, 11533-11541.

[100] W. Zou, S. Lin, J. Li, H. Wei, X. Zhang, D. Shen, J. Qiao, H. Lian, D. Xie, X. Ge. Mechanism and Application of Halogen Bond Induced Fluorescence Enhancement and Iodine Molecule Cleavage in Solution. *New J. Chem.* **2015**, 39, 262-272.

[101] J. K. Salunke, N. A. Durandin, T. Ruoko, N. R. Candeias, P. Vivo, E. Vuorimaa-Laukkanen, T. Laaksonen, A. Priimagi. Halogen-Bond-Assisted Photoluminescence Modulation in Carbazole-Based Emitter. *Sci. Rep.* **2018**, 8, 14431.

[102] J. C. Christopherson, F. Topić, C. J. Barrett, T. Friščić. Halogen-Bonded Cocrystals as Optical Materials: Next-Generation Control over Light-Matter Interactions. *Cryst. Growth Des.* **2018**, 18, 1245-1259.

[103] M. Gorbe, A. M. Costero, F. Sancenón, R. Martínez-Máñez, R. Ballesteros-Cillero, L. E. Ochando, K. Chulvi, R. Gotor, S. Gil. Halogen-containing BODIPY derivatives for photodynamic therapy. *Dyes Pigm.* **2019**, 160, 198-207.

[104] E. Özcan, B. Dedeoglu, Y. Chumakov, A. G. Gürek, Y. Zorlu, B. Çoşut, M. Menaf Ayhan. Halogen-Bonded BODIPY Frameworks with Tunable Optical Features. *Chem. Eur. J.* **2021**, 27, 1603-1608.

[105] A. Buckingham, J. Del Bene, S. McDowell. The hydrogen bond. *Chem. Phys. Lett.* **2008**, 463, 1-10.

[106] T. Fornaro, D. Burini, M. Biczysko, V. Barone. Hydrogen-Bonding Effects on Infrared Spectra from Anharmonic Computations: Uracil-Water Complexes and Uracil Dimers. *J. Phys. Chem. A* **2015**, 119, 4224-4236.

[107] N. F. Cheetham, I. J. McNaughtm, A. D. E. Pullin. Donor-Acceptor Complexes Formed by Perfluoro-Organo Bromides and Iodides with Nitrogenous and Other Bases. III. Qualitative Examination of Condensed Phase Spectra of CF3I and CF3Br and of Their Complexes with Trimethylamine and Other Bases. *Aust J. Chem.* **1974**, 27, 973-985.

[108] W. B. Person, R. E. Humphrey, A. I. Popov. Infrared Spectra of Charge Transfer Complexes. II. Iodine Cyanide Complexes1. *J. Am. Chem. Soc.* **1959**, 81, 273-277.

[109] R. S. Mulliken. Molecular Compounds and their Spectra. II. *J. Am. Chem. Soc.* **1952**, 74, 811-824.

[110] A. I. Popov, J. C. Marshall, F. B. Stute, W. B. Person. Studies on the Chemistry of Halogens and of Polyhalides. XXI. Halogen Complexes of 4,4'-Bipyridine and the Infrared Spectra of Pyridine Complexes. *J. Am. Chem. Soc.* **1961**, 83, 3586-3590.

[111] C. D. Schmulbach, R. S. Drago. Molecular Addition Compounds of Iodine. III. An Infrared Investigation of the Interaction Between Dimethylacetamide and Iodine1. *J. Am. Chem. Soc.* **1960**, 82, 4484-4487.

[112] N. F. Cheetham, A. D. E. Pullin. A Gas-Phase Donor-Acceptor Complex. *Chem. Commun. (London)* **1967**, 233-234.

[113] I. J. McNaught, A. D. E. Pullin. Donor-Acceptor Complexes Formed by Perfluoro-Organo Bromides and Iodides with Nitrogenous and other Bases. V. Comparison of Liquid Phase Complexes of CFI_3, C_2F_5I or C_3F_7I with NMe_3, NEt_3 or NPr_3; infrared, Far-Infrared and N.M.R. Spectra. *Aust. J. Chem.* **1974**, 27, 1009-1015.

[114] P. Metrangolo, G. Resnati. Halogen Bonding: A Paradigm in Supramolecular Chemistry. *Chem. Eur. J.* **2001**, 7, 2511-2519.

[115] M. T. Messina, P. Metrangolo, W. Panzeri, E. Ragg, G. Resnati. Perfluorocarbon-Hydrocarbon Self-Assembly. Part 3. Liquid Phase Interactions Between Perfluoroalkylhalides and Heteroatom Containing Hydrocarbons. *Tetrahedron Lett.* **1998**, 39, 9069-9072.

[116] M. Messina, P. Metrangolo, N. W., S. Radice, G. Resnati, G. Zerbi. Infrared and Raman Analyses of the Halogen-Bonded Non-Covalent Adducts Formed by α,ω-diiodoperfluoroalkanes with DABCO and Other Electron Donors. *J. .Mol. Struct.* **2000**, 524, 87-94.

[117] D. Pal, S. K. Agrawal, A. Chakraborty, S. Chakraborty. Competition Between the Hydrogen Bond and the Halogen Bond in a [CH_3OH-CCl_4] Complex: a Matrix Isolation IR Spectroscopy and Computational Study. *Phys. Chem. Chem. Phys.* **2020**, 22, 22465-22476.

[118] N. Nagels, Y. Geboes, B. Pinter, F. De Proft, W. A. Herrebout. Tuning the Halogen/Hydrogen Bond Competition: A Spectroscopic and Conceptual DFT Study of Some Model Complexes Involving CHF_2I. *Chem. Eur. J.* **2014**, 20, 8433-8443.

[119] N. Nagels, D. Hauchecorne, W. A. Herrebout. Exploring the C-X$\cdots\pi$ Halogen Bonding Motif: An Infrared and Raman Study of the Complexes of CF_3X (X = Cl, Br and I) with the Aromatic Model Compounds Benzene and Toluene. *Molecules* **2013**, 18, 6829–6851.

[120] S. Boys, F. Bernardi. The Calculation of Small Molecular Interactions by the Differences of Separate Total Energies. Some Procedures with Reduced Errors. *Mol. Phys.* **1970**, 19, 553–566.

[121] F. B. Duijneveldt, J. G. C. M. Rijdt, J. H. Lenthe. State of the Art in Counterpoise Theory. *Chem. Rev.* **1994**, 94, 1873-1885.

[122] B. Jeziorski, R. Moszyński, K. Szalewicz. Perturbation Theory Approach to Intermolecular Potential Energy Surfaces of van der Waals Complexes. *Chem. Rev.* **1994**, 94, 1887-1930.

[123] A. Heßelmann, G. Jansen. Intermolecular Dispersion Energies from Time-Dependent Density Functional Theory. *Chem. Phys. Lett.* **2003**, 367, 778-784.

[124] P. Fowler, A. Sadlej. Long-Range and Overlap Effects on Collision-Induced Properties. *Mol. Phys.* **1992**, 77, 709-725.

[125] D. M. Bishop, M. Dupuis. The Interaction Polarizability and Interaction Second-Hyperpolarizability for He···He. *Mol. Phys.* **1996**, 88, 887-898.

[126] B. Skwara, A. Kaczmarek, R. W. Góra, W. Bartkowiak. On Decomposition of Interaction-Induced Electric Properties of HF Dimer. *Chem. Phys. Lett.* **2008**, 461, 203-206.

[127] K. Müller-Dethlefs, P. Hobza. Noncovalent Interactions: A Challenge for Experiment and Theory. *Chem. Rev.* **2000**, 100, 143-168.

[128] J. P. Wagner, P. R. Schreiner. London Dispersion in Molecular Chemistry-Reconsidering Steric Effects. *Angew. Chem. Int. Ed.* **2015**, 54, 12274-12296.

[129] R. Zaleśny, M. Garcia-Borràs, R. W. Góra, M. Medved', J. M. Luis. On the Physical Origins of Interaction-Induced Vibrational (Hyper)Polarizabilities. *Phys. Chem. Chem. Phys.* **2016**, 18, 22467-22477.

[130] R. Zaleśny, M. Medved', R. W. Góra, H. Reis, J. M. Luis. Partitioning of Interaction-Induced Nonlinear Optical Properties of Molecular Complexes. I. Hydrogen-Bonded Systems. *Phys. Chem. Chem. Phys.* **2018**, 20, 19841-19849.

[131] M. Medved', A. Iglesias-Reguant, H. Reis, R. W. Góra, J. M. Luis, R. Zaleśny. Partitioning of Interaction-Induced Nonlinear Optical Properties of Molecular Complexes. II. Halogen-Bonded Systems. *Phys. Chem. Chem. Phys.* **2020**, 22, 4225-4234.

[132] W. Sokalski, S. Roszak, K. Pecul. An Efficient Procedure for Decomposition of the SCF Interaction Energy into Components with Reduced Basis Set Dependence. *Chem. Phys. Lett.* **1988**, 153, 153-159.

[133] A. J. Misquitta, R. Podeszwa, B. Jeziorski, K. Szalewicz. Intermolecular Potentials Based on Symmetry-Adapted Perturbation Theory with Dispersion Energies from Time-Dependent Density-Functional Calculations. *J. Chem. Phys.* **2005**, 123, 214103.

[134] S. M. Cybulski, G. Chałasiński, R. Moszyński. On Decomposition of Second-Order Møller-Plesset Supermolecular Interaction Energy and Basis Set Effects. *J. Chem. Phys.* **1990**, 92, 4357-4363.

[135] G. Chałasiński, M. Szcześniak. On the Connection Between the Supermolecular Møller-Plesset Treatment of the Interaction Energy and the Perturbation Theory of Intermolecular Forces. *Mol. Phys.* **1988**, 63, 205-224.

[136] S. Kozuch, J. M. L. Martin. Halogen Bonds: Benchmarks and Theoretical Analysis. *J. Chem. Theory Comput.* **2013**, 9, 1918-1931.

[137] L. P. Wolters, P. Schyman, M. J. Pavan, W. L. Jorgensen, F. M. Bickelhaupt, S. Kozuch. The Many Faces of Halogen Bonding: a Review of Theoretical Models and Methods. *WIREs Comput. Mol. Sci.* **2014**, 4, 523-540.

[138] S. Grimme, L. Goerigk, R. F. Fink. Spin-Component-Scaled Electron Correlation Methods. *WIREs Comput. Mol. Sci.* **2012**, 2, 886-906.

[139] S. Grimme. Improved Second-Order Møller-Plesset Perturbation Theory by Separate Scaling of Parallel- and Antiparallel-Spin Pair Correlation Energies. *J. Chem. Phys.* **2003**, 118, 9095-9102.

[140] W. Romberg. Vereinfachte Numerische Integration. *DKNVS Forhandlinger Bd.* **1955**, 28, 30-36.

[141] H. S. Yu, X. He, S. L. Li, D. G. Truhlar. MN15: A Kohn-Sham Global-Hybrid Exchange-Correlation Density Functional with Broad Accuracy for Multi-Reference and Single-Reference Systems and Noncovalent Interactions. *Chem. Sci.* **2016**, 7, 5032-5051.

[142] R. A. Kendall, J. Dunning, R. J. Harrison. Electron Affinities of the First-Row Atoms Revisited. Systematic Basis Sets and Wave Functions. *J. Chem. Phys.* **1992**, 96, 6796-6806.

[143] D. E. Woon, J. Dunning. Gaussian Basis Sets for Use in Correlated Molecular Calculations. III. The Atoms Aluminum Through Argon. *J. Chem. Phys.* **1993**, 98, 1358-1371.

[144] K. A. Peterson. Systematically Convergent Basis Sets with Relativistic Pseudopotentials. I. Correlation Consistent Basis Sets for the Post-d Group 13-15 Elements. *J. Chem. Phys.* **2003**, 119, 11099-11112.

[145] M. J. Frisch, G. W. Trucks, H. B. Schlegel, G. E. Scuseria, M. A. Robb, J. R. Cheeseman, G. Scalmani, V. Barone, G. A. Petersson, H. Nakatsuji, X. Li, M. Caricato, A. V. Marenich, J. Bloino, B. G. Janesko, R. Gomperts, B. Mennucci, H. P. Hratchian, J. V. Ortiz, A. F. Izmaylov, J. L. Sonnenberg, D. Williams-Young, F. Ding, F. Lipparini, F. Egidi, J. Goings, B. Peng, A. Petrone, T. Henderson, D. Ranasinghe, V. G. Zakrzewski, J. Gao, N. Rega, G. Zheng, W. Liang, M. Hada, M. Ehara, K. Toyota, R. Fukuda, J. Hasegawa, M. Ishida, T. Nakajima, Y. Honda, O. Kitao, H. Nakai, T. Vreven, K. Throssell, J. A. Montgomery, J. E. Peralta, F. Ogliaro, M. J. Bearpark, J. J. Heyd, E. N. Brothers, K. N. Kudin, V. N. Staroverov, T. A. Keith, R.

Kobayashi, J. Normand, K. Raghavachari, A. P. Rendell, J. C. Burant, S. S. Iyengar, J. Tomasi, M. Cossi, J. M. Millam, M. Klene, C. Adamo, R. Cammi, J. W. Ochterski, R. L. Martin, K. Morokuma, O. Farkas, J. B. Foresman, D. J. Fox. Gaussian-16 Revision C.01, **2016**. Gaussian Inc. Wallingford CT.

[146] H.-J. Werner, P. J. Knowles, G. Knizia, F. R. Manby, M. Schütz. Molpro: a General-Purpose Quantum Chemistry Program Package. *WIREs Comput. Mol. Sci.* **2012**, 2, 242-253.

[147] M. W. Schmidt, K. K. Baldridge, J. A. Boatz, S. T. Elbert, M. S. Gordon, J. H. Jensen, S. Koseki, N. Matsunaga, K. A. Nguyen, S. Su, T. L. Windus, M. Dupuis, J. A. Montgomery Jr. General Atomic and Molecular Electronic Structure System. *J. Comput. Chem.* **1993**, 14, 1347-1363.

[148] R. Puttreddy, J. M. Rautiainen, S. Yu, K. Rissanen. NXON Halogen Bonds in Complexes of N-Haloimides and Pyridine-N-oxides: A Large Data Set Study. *Angew. Chem. Int. Ed.* **2023**, 62, e202307372.

[149] M. Medved', A. Iglesias-Reguant, H. Reis, R. W. Góra, J. M. Luis, R. Zaleśny. Partitioning of Interaction-Induced Nonlinear Optical Properties of Molecular Complexes. II. Halogen-Bonded Systems. *Phys. Chem. Chem. Phys.* **2020**, 22, 4225-4234.

[150] B. Dereka, I. Fureraj, A. Rosspeintner, E. Vauthey. Halogen-Bond Assisted Photoinduced Electron Transfer. *Molecules* **2019**, 24, 4361.

[151] M. G. Sarwar, B. Dragisic, L. J. Salsberg, C. Gouliaras, M. S. Taylor. Thermodynamics of Halogen Bonding in Solution: Substituent, Structural, and Solvent Effects. *J. Am. Chem. Soc.* **2010**, 132, 1646-1653.

[152] T. M. Beale, M. G. Chudzinski, M. G. Sarwar, M. S. Taylor. Halogen Bonding in Solution: Thermodynamics and Applications. *Chem. Soc. Rev.* **2013**, 42, 1667-1680.

[153] S. B. Hakkert, J. Gräfenstein, M. Erdelyi. The 15N NMR Chemical Shift in the Characterization of Weak Halogen Bonding in Solution. *Faraday Discuss.* **2017**, 203, 333-346.

[154] T. G. A. Heijmen, R. Moszyński, P. E. S. Wormer, A. van der Avoird. Symmetry-Adapted Pperturbation Theory Applied to Interaction-Induced Properties of Collisional Complexes. *Mol. Phys.* **1996**, 89, 81–110.

[155] R. W. Góra, R. Zaleśny, A. Zawada, W. Bartkowiak, B. Skwara, M. G. Papadopoulos, D. L. Silva. Large Changes of Static Electric Properties Induced by Hydrogen

Bonding: An ab Initio Study of Linear HCN Oligomers. *J. Phys. Chem. A* **2011**, 115, 4691-4700.

[156] R. W. Góra, B. Błasiak. On the Origins of Large Interaction-Induced First Hyperpolarizabilities in Hydrogen-Bonded π-Electronic Complexes. *J. Phys. Chem. A* **2013**, 117, 6859-6866.

[157] M. Torrent-Sucarrat, B. Kirtmand, J. M. Luis. Accurate Evaluation of Vibrational Nonlinear Optical Properties. *AIP Conf. Proc.* **2009**, 1148, 717-720.

[158] J. M. Luis, M. Duran, J. L. Andrés. A Systematic and Feasible Method for Computing Nuclear Contributions to Electrical Properties of Polyatomic Molecules. *J. Chem. Phys.* **1997**, 107, 1501-1512.

[159] D. M. Bishop, Molecular Vibration and Nonlinear Optics, pages 1–40. John Wiley & Sons, Ltd, **1998**.

[160] C. Eckart. Operator Calculus and the Solution of the Equations of Quantum Dynamics. *Phys. Rev.* **1926**, 28, 711-726.

[161] J. M. Luis, M. Duran, J. L. Andrés, B. Champagne, B. Kirtman. Finite Field Treatment of Vibrational Polarizabilities and Hyperpolarizabilities: On the Role of the Eckart Conditions, Their Implementation, and Their Use in Characterizing Key Vibrations. *J. Chem. Phys.* **1999**, 111, 875-884.

[162] P. Besalú-Sala, M. Solà, J. M. Luis, M. Torrent-Sucarrat. Fast and Simple Evaluation of the Catalysis and Selectivity Induced by External Electric Fields. *ACS Catal.* **2021**, 11, 14467-14479.

[163] B. Kirtman, J. M. Luis, D. M. Bishop. Simple Finite Field Method for Calculation of Static and Dynamic Vibrational Hyperpolarizabilities: Curvature Contributions. *J. Chem. Phys.* **1998**, 108, 10008-10012.

[164] J. M. Luis, M. Duran, J. L. Andrés, B. Champagne, B. Kirtman. Finite Field Treatment of Vibrational Polarizabilities and Hyperpolarizabilities: On the Role of the Eckart Conditions, Their Implementation, and Their Use in Characterizing Key Vibrations. *J. Chem. Phys.* **1999**, 111, 875-884.

[165] C. G. Broyden. The Convergence of a Class of Double-rank Minimization Algorithms 1. General Considerations. *IMA J. Appl. Math.* **1970**, 6, 76-90.

[166] R. Fletcher. A New Approach to Variable Metric Algorithms. *Comput. J.* **1970**, 13, 317-322.

[167] D. Goldfarb. A Family of Variable-Metric Methods Derived by Variational Means. *Math. Comp.* **1970**, 24, 23-26.

[168] D. F. Shanno. Conditioning of Quasi-Newton Methods for Function Minimization. *Math. Comp.* **1970**, 24, 647-656.

[169] C. Møller, M. S. Plesset. Note on an Approximation Treatment for Many-Electron Systems. *Phys. Rev.* **1934**, 46, 618–622.

List of Figures

List of Tables

Full List of Publications

Published and submitted articles included in the Thesis:

- A. Iglesias-Reguant, J. Zielak-Milewska, T. Misiaszek, R. Zaleśny, J. M. Luis, B. Ośmiałowski. Unveiling Halogen-Bonding Interactions between a Pyridine-Funcitionalized Fluoroborate Dye and Perfluorohaloarenes with Fluorescence Spectroscopy. *J. Org. Chem.* **2022**, 87, 15159–15165. (IF_{2022}: 3.6; Q1 in Organic Chemistry).

- A. Iglesias-Reguant, H. Reis, M. Medved', J. M. Luis, R. Zaleśny. A New Computational Tool for Interpreting the Infrared Spectra of Molecular Complexes. *Phys. Chem. Chem. Phys.*, **2023**, 25, 11658. (IF_{2023}: 3.3; Q1 in Physics, Atomic, Molecular & Chemical).

- A. Iglesias-Reguant, H. Reis, M. Medved', B. Ośmiałowski, J. M. Luis, R. Zaleśny. Decoding the Infrared Spectra Changes Upon Formation of Molecular Complexes: the Case of Halogen Bonding in Pyridine$\cdots$Perfluorohaloarene Complexes. *Phys. Chem. Chem. Phys.*, **2023**, 25, 20173. (IF_{2023}: 3.3; Q1 in Physics, Atomic, Molecular & Chemical).

Other published and submitted articles not included in the PhD thesis:

- T. N. Moshkina, E. V. Nosova, A. E. Kopotilova, B. Ośmiałowski, A. Iglesias-Reguant, P. A. Slepukhin, G. N. Lipunova, O. S. Taniya, A. A. Kalinichev, V. N. Charushin. (A)symmetric Chromophores Based on Cyano and Fluorine-Substituted 2,3-bis(5-arylthiophen-2-yl)quinoxalines: Synthesis, Photophysical Properties and Application Prospects. *Dyes Pigm.*. **2022**, 204, 110434. (IF_{2022}: 4.5; Q1 in Chemical Engineering (miscellaneous)).

- K. Kamińska, D. Iwan, A. Iglesias-Reguant, W. Spałek, M. Daszkiewicz, A. Sobolewska, R. Zaleśny, E. Wojaczyńska, E. Bartkiewicz. Synthesis, Spectroscopic and Computa-

tional Studies of Photochromic Azobenzene Derivatives with 2-azabicycloalkane Scaffold. *J. Mol. Liq.*, **2022**, 363, 119869. (IF_{2022}: 6.0; Q1 in Spectroscopy).

- P. Rybczyński, A. Kaczmarek-Kędziera, A. Iglesias-Reguant, D. Plażuk, B. Ośmiałowski. Tautomeric Equilibrium in 1-Benzamidoisoquinoline Derivatives. *Molecules*, **2023**, 28, 1101. (IF_{2023}: 4.6; Q2 in Multidisciplinary Chemistry).

Supplemental Data

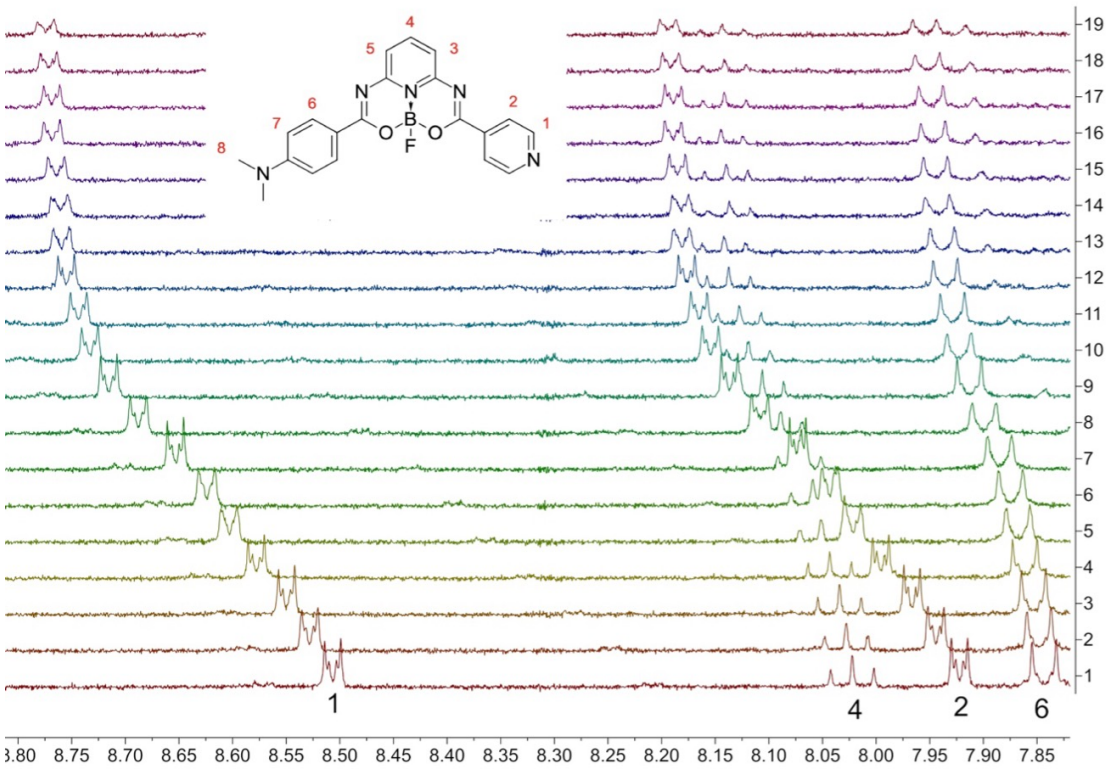

Figure 6.1: The stacked ^{1}H-NMR titration spectra of **A-3** in C_6F_6 by addition of C_6F_5I.

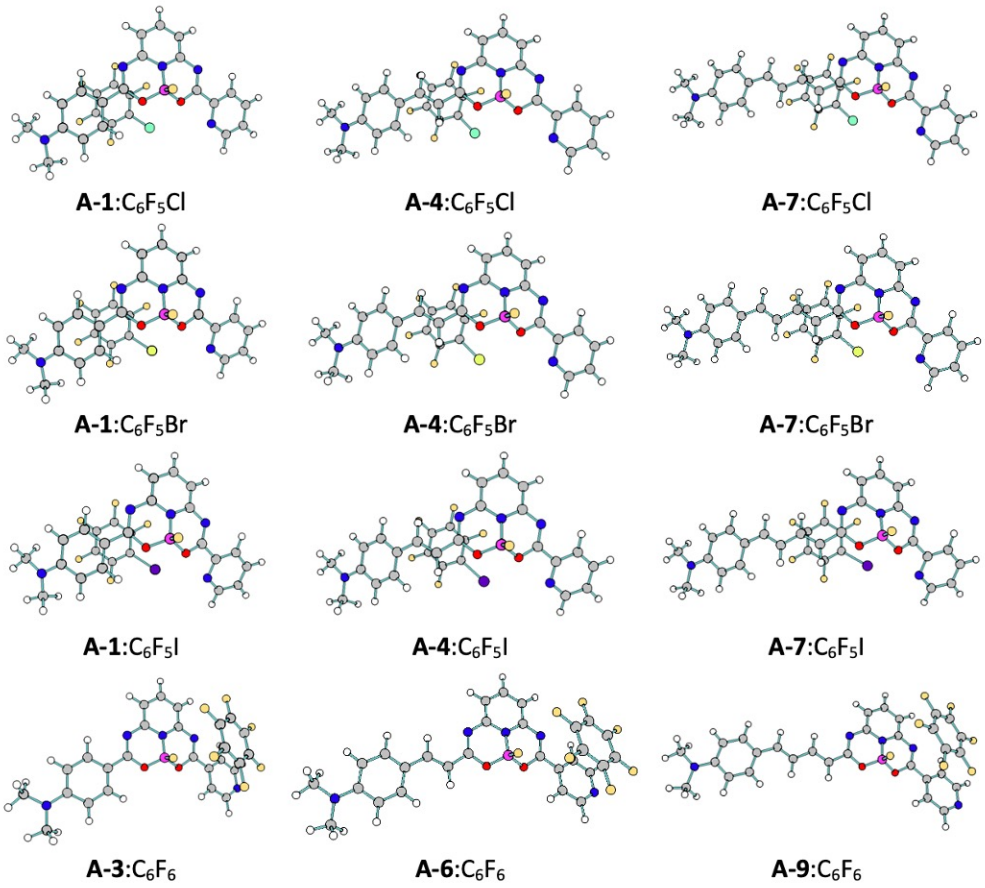

Figure 6.2: Equilibrium geometries of the **A**-series complexes of group 2 obtained at the MN15/aug- cc-pVDZ(PP) level of theory.

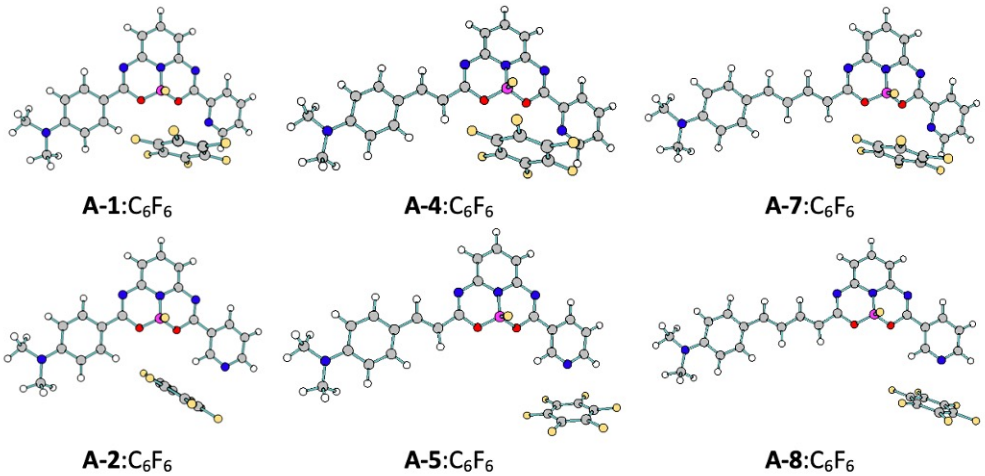

Figure 6.3: Equilibrium geometries of the **A**-series complexes of group 3 obtained at the MN15/aug- cc-pVDZ(PP) level of theory.

Table 6.1: Intermolecular interaction energy (ΔE, in kcal/mol) of **A**-series dyes computed using DF-SCS-MP2 method and the aug-cc-pVDZ(PP) basis set.

	C_6F_6	C_6F_5Cl	C_6F_5Br	C_6F_5I
A-1	-7.32	-10.7	-11.39	-12.56
A-2	-4.34	-3.28	-3.97	-6.32
A-3	-7.08	-2.33	-4.03	-6.41
A-4	-7.76	-8.95	-9.34	-9.92
A-5	-3.99	-2.38	-3.96	-6.28
A-6	-7.05	-2.41	-4.05	-6.43
A-7	-7.62	-8.25	-8.88	-10.32
A-8	-4.04	-2.32	-3.96	-6.21
A-9	-7.02	-2.38	-4.02	-6.42

Table 6.2: Partitioning of the interaction energy (ΔE) of **A-2**:C_6F_5X, **A-3**:C_6F_5X, **A-4**:C_6F_5X, and **A-6**:C_6F_5X complexes at the equilibrium geometries at the MP2/aug-cc-pVDZ(PP) level of theory.

	$\Delta E_{el}^{(10)}$	$\Delta E_{del}^{\mathrm{HF}}$	$\Delta E_{ex}^{\mathrm{HL}}$	$\Delta E_{int}^{\mathrm{HF}}$	$\Delta E_{int}^{\mathrm{SCS-MP2}}$
A-2:C_6F_5Cl	-3.46	-0.91	5.11	0.74	-3.28
A-2:C_6F_5Br	-9.17	-3.33	11.92	-0.59	-3.97
A-2:C_6F_5I	-15.91	-6.94	20.63	-2.23	-6.32
A-3:C_6F_5Cl	-3.42	-0.93	4.28	-0.07	-2.33
A-3:C_6F_5Br	-9.29	-3.39	12.14	-0.55	-4.03
A-3:C_6F_5I	-16.14	-7.08	21.09	-2.13	-6.41
A-4:C_6F_5Cl	-7.93	-2.27	18.02	7.81	-8.25
A-4:C_6F_5Br	-8.45	-2.51	19.40	8.44	-9.34
A-4:C_6F_5I	-8.45	-2.77	20.32	8.47	-9.92
A-6:C_6F_5Cl	-3.54	-0.99	4.35	-0.18	-2.41
A-6:C_6F_5Br	-9.45	-3.48	12.34	-0.59	-4.05
A-6:C_6F_5I	-16.14	-7.08	21.09	-2.18	-6.43

Table 6.3: The computed ^{1}H-NMR chemical shift in gas phase, C_6F_6 solvent, and C_6F_5I solvent.

	gas phase	C_6F_6 (pcm)	C_6F_5I (pcm)
H4	-0.14	-0.12	-0.10
H5	-0.03	-0.03	-0.04
H6	-0.01	-0.01	-0.02
H7	0.95	0.95	0.96
H8	0.41	0.36	0.31

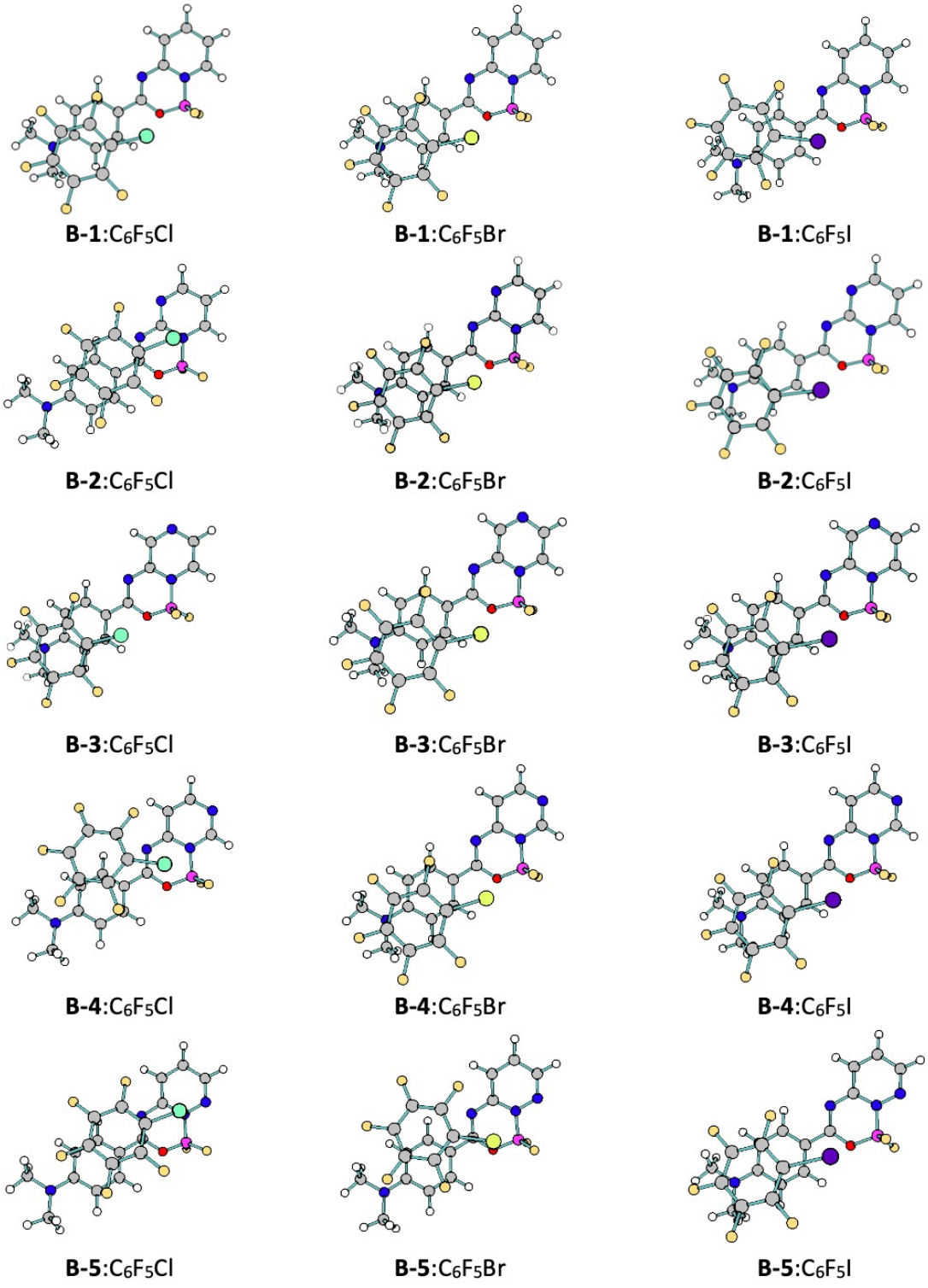

Figure 6.4: Equilibrium geometries of the π-stacking **B**:C_6F_5X complexes of group 2 obtained at the MN15/aug- cc-pVDZ(PP) level of theory.

Table 6.4: Partitioning of the interaction energy (ΔE) of $\mathbf{B}^h$:C_6F_5I and $\mathbf{B}^i$:C_6F_5I complexes at the equilibrium geometries at the MP2/aug-cc-pVDZ(PP) level of theory.

	$\Delta E_{el}^{(10)}$	$\Delta E_{del}^{\mathrm{HF}}$	$\Delta E_{ex}^{\mathrm{HL}}$	$\Delta E_{int}^{\mathrm{HF}}$	$\Delta E_{int}^{\mathrm{SCS-MP2}}$
$\mathbf{B}^h$**-2**:C_6F_5I	-11.63	15.18	-4.85	-1.31	-6.40
$\mathbf{B}^h$**-3**:C_6F_5I	-11.40	15.14	-4.52	-0.77	-4.64
$\mathbf{B}^h$**-4**:C_6F_5I	-11.63	14.85	-4.55	-1.33	-4.43
$\mathbf{B}^h$**-5**:C_6F_5I	-8.29	11.42	-3.80	-0.67	-4.72
$\mathbf{B}^i$**-1**:C_6F_5I	-11.03	16.15	-4.56	0.56	-5.73
$\mathbf{B}^i$**-2**:C_6F_5I	-10.08	14.28	-4.22	-0.02	-5.72
$\mathbf{B}^i$**-3**:C_6F_5I	-9.79	14.69	-3.91	0.99	-5.09
$\mathbf{B}^i$**-4**:C_6F_5I	-9.99	14.89	-3.98	0.92	-5.17
$\mathbf{B}^i$**-5**:C_6F_5I	-10.56	15.63	-4.26	0.82	-5.40

Table 6.5: Partitioning of the interaction energy (ΔE) of **pyr**:C_6F_5Cl, **pyr**:C_6F_5Br, and **pyr**:C_6F_5I complexes at the equilibrium geometries at the MP2/aug-cc-pVDZ(PP) level of theory.

	pyr:C_6F_5Cl	**pyr**:C_6F_5Br	**pyr**:C_6F_5I
$\Delta E_{el}^{(10)}$	-5.18	-11.00	-19.31
$\Delta E_{del}^{\mathrm{HF}}$	-1.58	-4.17	-8.80
$\Delta E_{ex}^{\mathrm{HL}}$	7.16	14.81	26.08
$\Delta E_{int}^{\mathrm{HF}}$	0.40	-0.36	-2.03
$\Delta E_{el,r}^{(12)}$	-0.55	-1.14	-1.80
$\Delta E_{dis}^{(20)}$	-4.79	-6.80	-9.30
$\Delta E_{ex}^{(2)}$	1.86	3.24	5.38
$\Delta E_{int}^{\mathrm{MP2}}$	-3.08	-5.06	-7.75

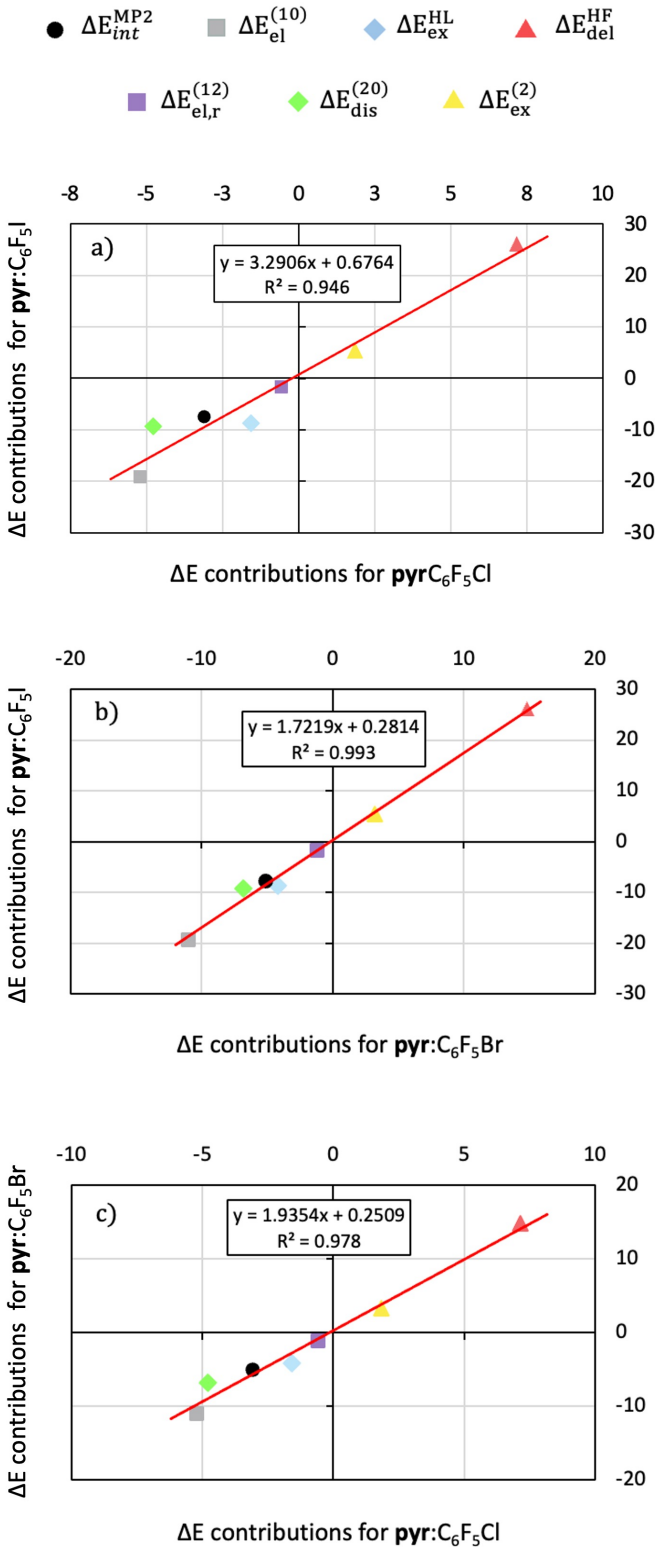

Figure 6.5: Linear regressions between interaction-type contributions for the interaction energy of **pyr**:C_6F_5Cl vs. **pyr**:C_6F_5I, **pyr**:C_6F_5Br vs. **pyr**:C_6F_5I, and **pyr**:C_6F_5Cl vs. **pyr**:C_6F_5Br. Energies are given in kcal/mol.